

UNIVERSITÉ PARIS-SUD XI
École Doctorale 517 PNC : Particules, Noyaux, Cosmos

Discipline : Physique

THÈSE DE DOCTORAT

présentée par

Clémentine SANTAMARIA

effectuée au CEA, Centre de Saclay,
IRFU/Service de Physique Nucléaire

pour obtenir le grade de
Docteur en Sciences de l'Université Paris-Sud XI

Quest for new nuclear magic numbers with MINOS

Soutenue le 7 septembre 2015

Directeur de thèse : Dr. Alexandre OBERTELLI

Composition du jury :

Pr. Elias KHAN	: président du jury
Dr. Alexandre OBERTELLI	: directeur de thèse
Pr. Peter REITER	: rapporteur
Dr. Olivier SORLIN	: rapporteur
Dr. Kathrin WIMMER	: examinatrice

REMERCIEMENTS

Après trois années de thèse, me voici à la fin sans même m'en être aperçue... Ces années au CEA et au Japon ont été remplies d'apprentissage, de travail, mais aussi de belles rencontres et d'amitiés qui m'ont aidée et soutenue et sans lesquelles je ne pourrais pas aujourd'hui écrire ces remerciements. Je vais essayer de rester brève tout en tentant de n'oublier personne, ce qui n'est pas chose facile.

Je voudrais premièrement remercier mon directeur de thèse Alexandre Obertelli sans qui la thèse n'existerait pas. Il m'a fait confiance pour participer à la naissance du détecteur MINOS avec les ingénieurs et être responsable de son exploitation avec les premiers tests sous faisceau, la création d'un algorithme de tracking, puis les expériences de physique et leur analyse. Alexandre est pour moi un vrai passionné de la physique nucléaire qui fourmille d'idées innovantes à mettre en pratique pour faire avancer le domaine significativement. J'ai beaucoup appris grâce à lui, surtout à essayer d'avoir une vision moins restrictive et plus générale de la physique nucléaire et vais m'efforcer de mettre cela en pratique durant ma carrière. Cette année au Japon avec lui a été une expérience formidable, avec des journées de travail entrecoupées de pauses touristiques ou culinaires. C'est peut-être un peu cliché mais je n'aurais vraiment pas pu avoir meilleur directeur de thèse, collègue et ami durant ces trois ans.

J'aimerais aussi dire un grand merci à l'incommensurable patience et gentillesse d'Anna Corsi qui a toujours été là pour répondre à mes questions, pour faire des simulations au pied levé et même pour m'héberger pendant une semaine ! J'aimerais finalement remercier plus généralement mon groupe de recherche au SPhN, Valérie Lapoux, Alain Gillibert et Lolly Pollacco, qui par leur organisation, leur force tranquille et leur expérience m'ont toujours épaulée et encouragée. Je n'ai pas vu le temps passer et c'est avec regret que je vois la fin toute proche, alors je ne dirai pas au revoir à tout le groupe mais à bientôt au Japon ou ailleurs, car je compte bien continuer à travailler avec vous !

Je ne peux pas continuer sans remercier au grand complet la "dream team" MINOS du CEA. Ces personnes sans qui le projet serait resté à l'état d'idée et qui ont toujours été là pendant le développement et/ou en expérience: Alain Delbart, Alan Peyaud, Arnaud Giganon, Gilles Prono, Caroline Lahonde-Hamdoun, Denis Calvet, Frédéric Château, Jean-Marc Gheller, Gilles Authelet, Jean-Yves Roussé, Cédric Péron... Merci aussi pour leur capacité de détente en toute circonstance, je sais que je n'ai pas forcément été de tout repos en expérience, et je les remercie de m'avoir aidée dans ces moments de stress.

Je voudrais remercier Michel Garçon et Héloïse Goutte de m'avoir accueillie au sein du SPhN durant trois ans, et le service en général pour leur gentillesse et mes échanges avec Antoine Drouart, Thomas Duguet, Vittorio Soma, Barbara Sulignano et d'autres que je m'excuse d'avoir oubliés.

Je finis ma tournée française avec une attention spéciale aux thésards et post-docs que j'ai cotoyés durant ces deux ans effectifs au SPhN, et sans qui les moments de procrastination auraient été bien plus ternes ! Merci à Simon Boissinot et Matthieu Sénoville qui ont partagé mon bureau et accepté d'écouter mes soucis de code (le canard !) ou autres. Merci aussi à Jean-François Lemaitre, Raphaël Briselet et Loïc Thulliez pour votre bonne humeur et nos échanges toujours loufoques ! Ne vous inquiétez pas, je garderai le contact ! Enfin, petite dédicace à Benjamin qui se reconnaîtra : merci aux Terriens...

Il est temps pour moi de me tourner vers le soleil levant et mon année au Japon. Je voudrais remercier Pieter Doornenbal (j'écris en français pour le faire pratiquer un peu !) pour son soutien durant ces mois d'expérience et d'analyse intenses. Merci de sa gentillesse et de son humour, mais aussi de son expérience en spectroscopie qui m'a beaucoup aidée. Je continuerai à passer au Japon pour t'ennuyer encore un peu !

I would like to thank all of my RIKEN colleagues for this year in Japan: Tomohiro Uesaka for hosting me in the Spin-Isospin laboratory, and a special mention to the PhD and post-docs I have met there with whom I have spent memorable evenings of izakaya and karaoke (Hongna Liu, P-A Söderström, He Wang, Jin Wu, Zhengyu Xu...) ! During this year, we have accomplished so much with the SEASTAR collaboration and I would like to thank all the people I have met there and hope to see them in the future !

Je voudrais également remercier les personnes qui ont contribué à l'amélioration de ce manuscrit, Alexandre Obertelli, Anna Corsi, Nancy Paul et Vittorio Soma. J'en profite au passage pour dire merci à mon jury de thèse, Elias Khan, Peter Reiter, Olivier Sorlin et Kathrin Wimmer, pour avoir pris le temps de lire le manuscrit, de venir pour ma soutenance et pour leurs questions et commentaires qui ont apporté à cette version finale du manuscrit de thèse.

Je ne pourrais pas terminer ces remerciements sans mentionner mes parents qui m'ont toujours encouragée dans tout ce que j'ai entrepris, et grâce à qui j'ai acquis cette envie d'apprentissage et de recherche. Merci !

A tous ces gens qui m'ont permis d'écrire cette thèse, maintenant vous devez la lire (si ce n'est pas déjà fait) !

CONTENTS

Remerciements	3
1 Motivations	1
1.1 Nuclear structure and exotic nuclei	1
1.2 Theoretical models of nuclear physics	3
1.2.1 Nuclear structure	3
1.2.2 Direct reactions	6
1.3 Very exotic nuclei and MINOS	8
1.3.1 First spectroscopy of very exotic nuclei	8
1.3.2 Island of Inversion	9
2 MINOS : conception and validation	13
2.1 General description	13
2.1.1 Liquid hydrogen target	13
2.1.2 Vertex tracker	16
2.1.3 Ancillary detectors	21
2.1.4 Electronics and data acquisition	21
2.2 Alpha source and cosmic bench tests	24
2.2.1 α source tests	24
2.2.2 Cosmic bench tests	27
2.3 Physics cases simulations	31
3 In-beam performances at the HIMAC facility and tracking algorithm	33
3.1 Experimental setup	33
3.2 Tracking algorithm	34
3.2.1 Software description	35
3.2.2 Selection of events	36
3.2.3 Track filtering	38
3.2.4 Track fitting and vertex finding	39
3.3 TPC performances	41
3.3.1 Drift velocity	42
3.3.2 Resolutions	43
3.3.3 Pad multiplicity	44

4	Setup of the first SEASTAR experimental campaign	47
4.1	Radioactive Isotope Beam Factory	47
4.1.1	Primary beam production	47
4.1.2	BigRIPS and ZeroDegree spectrometers	48
4.2	DALI2	52
4.3	MINOS configuration	54
4.4	Trigger and data acquisition	55
5	Data analysis	59
5.1	Particle Identification	59
5.1.1	$B\rho$ - ΔE -TOF identification method	60
5.1.2	Identification in BigRIPS	60
5.1.3	Corrections for the ZeroDegree identification	62
5.1.4	Efficiency and beam line transmission	63
5.2	DALI2 Calibration	65
5.2.1	Energy calibration	65
5.2.2	Efficiency	69
5.3	MINOS Calibration	70
5.3.1	Drift velocity	70
5.3.2	Inclusion of beam tracking: PPAC and DSSSD	71
5.3.3	Doppler correction with MINOS	72
5.4	Reference measurement: ^{68}Fe	74
5.4.1	Dependence over angle and vertex	74
5.4.2	Energy spectrum of ^{68}Fe	76
5.5	Momentum distribution of the knocked-out proton	77
6	Results and Interpretation	81
6.1	Energy spectrum	81
6.2	Cross section	86
6.2.1	Inclusive cross sections	86
6.2.2	Exclusive cross sections	88
6.3	^{66}Cr and collectivity beyond $N=40$ below ^{78}Ni	91
	Conclusion	97
A	MINOS tracking algorithm characteristics	103
B	Beam line characteristics	104
C	Electronics scheme	106
D	Accepted article	107
	Bibliography	118

CHAPTER 1

Motivations

1.1 Nuclear structure and exotic nuclei

In 1934, W. Elsasser [1] noticed an evolution of the binding energies of light nuclei along the nuclear chart. With an analogy to atomic electrons, he correlated the more bound nuclei with closed shells of protons and neutrons. He established for the first time a harmonic oscillator model of non-interacting nucleons to describe nuclei with a potential well generating different energy levels. Due to the lack of experimental evidence for a single-particle description of nuclei, the theory was not pursued until 1949 when M. Goeppert-Mayer [2, 3] and O. Haxel, J. Jensen and H. Suess [4] independently showed that the inclusion of a spin-orbit potential could give rise to the observed experimental gaps between the shells or orbitals, called "magic numbers" at 2, 8, 20, 28, 50, and 82 nucleons. It gave rise to a great advance in understanding the nuclear structure as it was able to reproduce properties of nuclei such as spins, magnetic moments, isomeric states, and γ -decay systematics.

Not only masses are important to determine the shell structure of a nucleus, but also the spectroscopy of the nucleus with its excited states. The excited states of a nucleus correspond to the transition of one or several nucleons to higher energy available orbitals and reflect its structure. For the first study of a nucleus, the measurement of the first excited states is therefore important, as well as the probabilities of the transitions. For even-even nuclei over the nuclear chart, we can measure their first excited state energy, shown in Fig. 1.1, with their transition probability to the ground state $B(E2)$. This is related to the ratio of second to first excited state energies, shown in Fig. 1.2. The highest values of first excited state energies coincide with magic numbers, i.e. more stable nuclei.

For several decades, these magic numbers remained a constant with observed nuclei. In 1975, the measured β -decays of Na isotopes showed a lowest excitation energy for ^{32}Mg , with $Z=12$ and $N=20$ [5, 6]. These measurements showed the non immutability of the $N=20$ magic number and put in question the understanding of nuclear structure for exotic nuclei.

With the advent of radioactive ion beam accelerators such as GANIL in France, ISOLDE at CERN, NSCL in USA, Radioactive Ion Beam facility of RIKEN in Japan, GSI in Germany, heavy ion beams were accelerated and radioactive nuclei with rather large neutron to proton number ratios, i.e. on the sides of the nuclear chart, were produced. These "exotic" nuclei, not present in natural conditions on Earth, were then measured and characterized for the first time. Since then, experimental measurements have never stopped to further dwell in more exotic nuclei with an upgrade of the heavy ion beam facilities to reach more neutron-rich regions.

Other regions of the nuclear chart have exhibited a change of shell structure with the disappearance of standard magic numbers and the appearance of new shell closures for exotic nuclei

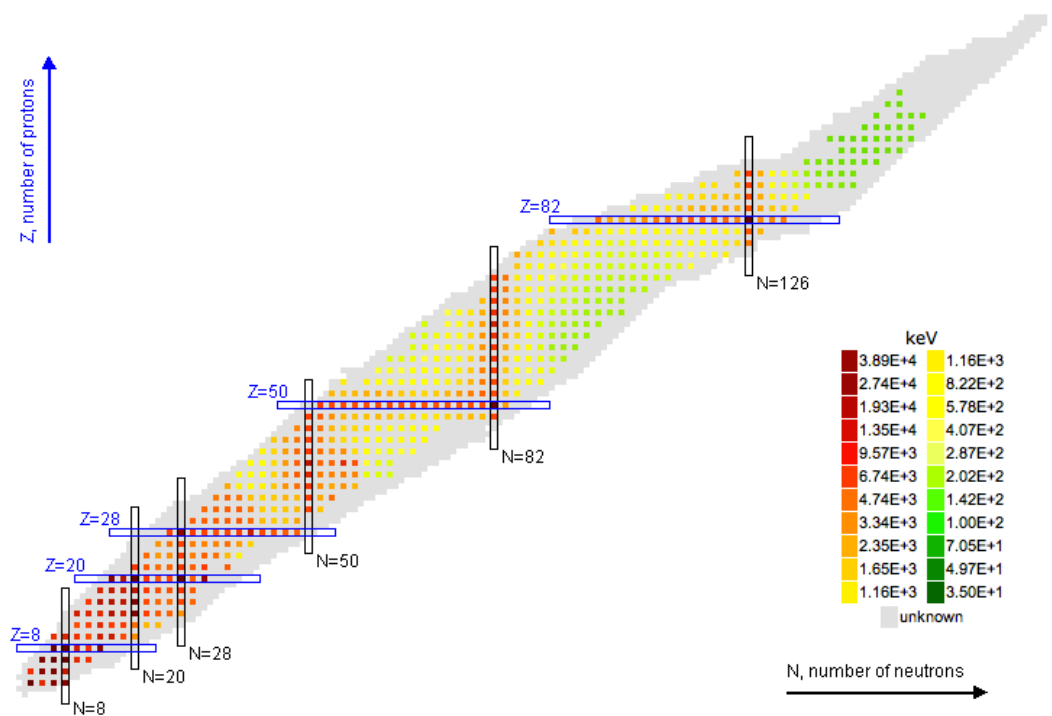


Fig. 1.1 – Nuclear chart with number of neutrons on the abscissa and number of protons on the ordinate. The known first excited state energies for even-even nuclei are given in color. The highest values of first excited state energies coincide with magic numbers, indicated on the graph. Source: <http://www.nndc.bnl.gov/nudat2/>.

[8, 9]. The region of $N=20$ and $N=28$ neutron-rich nuclei has been more thoroughly examined and regions of deformation have been found for both. For example a low first excited state has been discovered in ^{42}Si at $N=28$ [10, 11]. A merging of these two phenomena into one large region of deformation is suggested for several isotopes in this region [7], confirmed for example in Mg isotopes as shown with the systematics of the two first excitation energies in Fig.1.3. The existence of sub-shell gaps at $N = 32$ in Ca, Ti and Ar isotopes has been confirmed with the spectroscopy of ^{52}Ca [8], ^{54}Ti [12, 13] and ^{50}Ar [14], and at $N=34$ with ^{54}Ca [9].

Theory in nuclear physics aims at reproducing the experimental exotic nuclei and at predicting the evolution towards even more exotic nuclei still unexplored. Nuclear physics experiments in unexplored regions of the nuclear chart are required with the measurement of relevant observables along isotopic (same number of protons) and isotonic (same number of neutrons) chains to understand the evolution of nuclear structure along the nuclear chart [15]. However, the nuclear many-body problem involves two types of nucleons (fermions), with an internal structure of quarks and gluons. Because of this, the in-medium nucleon-nucleon interaction in a nucleus cannot be known exactly. Hadronic physics aims at the better understanding of the nucleon structure, to be interpreted within Quantum ChromoDynamics (QCD). Lattice [16] calculations still have many limitations to reproduce observables such as the proton radius.

The structure of an unstable nucleus is described by "static" observables such as its mass

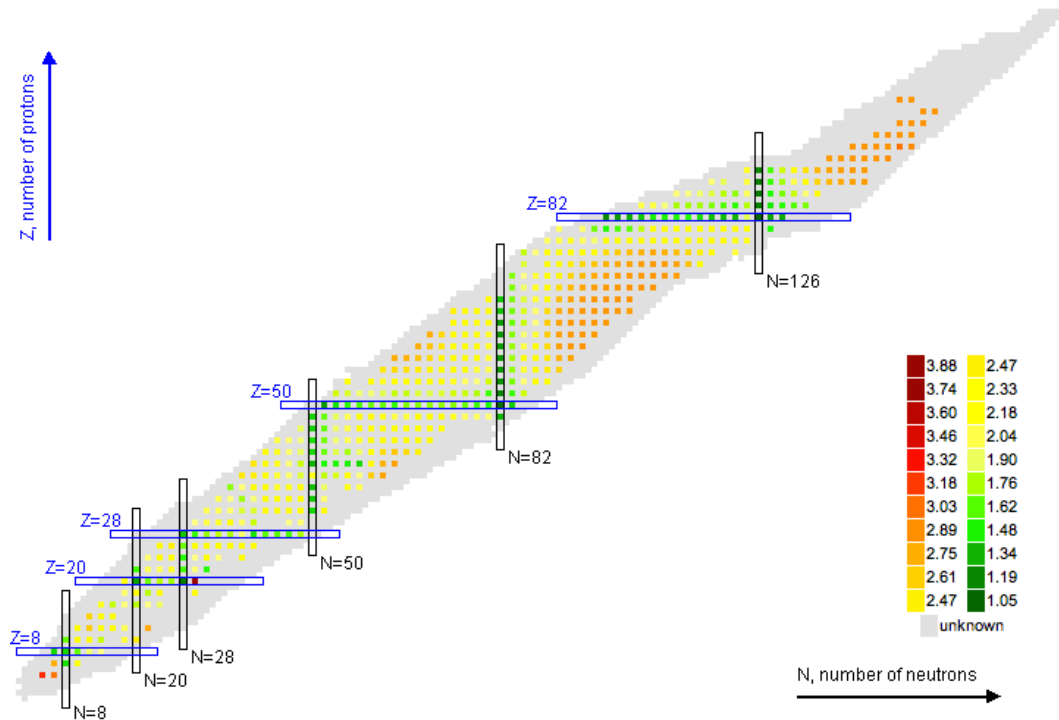


Fig. 1.2 – Nuclear chart with number of neutrons on the abscissa and number of protons on the ordinate. The known ratio of second to first excited state energies for even-even nuclei are shown in color. The highest ratios are an indication of deformation. Source: <http://www.nndc.bnl.gov/nudat2/>.

and spectroscopy. It can also be conveyed by direct reaction cross sections when analyzed with a proper model. Nuclear direct reactions are also sensitive to the single-particle states in the structure of the nucleus.

1.2 Theoretical models of nuclear physics

Theoretical models in nuclear physics may be built upon different approximations depending on the observable of interest in the nucleus. We give in the following a brief description of the two most encountered nuclear structure models: the shell model and the Hartree-Fock-Bogoliubov based calculations, as well as an overview of models for direct reactions. The reaction and nuclear structure parts are usually described with two distinct theories as most of the theories. Indeed, the reaction part is often derived without considering the many internal degrees of freedom of the colliding nuclei, while the nuclear structure part has to take into account many-body correlations arising from the interactions between nucleons.

1.2.1 Nuclear structure

Shell Model. Historically, the nuclear structure has been interpreted with shells in analogy with the atom. This theory based on particle-independent nucleons in a potential well is called

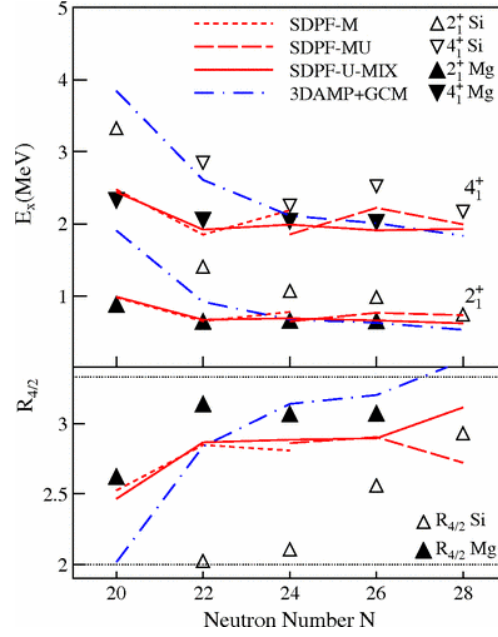


Fig. 1.3 – First 2_1^+ and second 4_1^+ excitation energies for even-even isotopes of Si and Mg and the ratio of second to first excited state $R_{4/2}$. The energies are constant from $N=20$ to $N=26$ for Mg isotopes whereas Si isotopes exhibit a higher excitation energy at $N=20$, confirming a shell gap for Si, with a sudden decrease of energies towards $N=28$ which shows an onset of collectivity for Si. The figure is taken from Ref. [7].

Shell Model. Nucleons fill the eigenstates, i.e. orbitals, of the mean potential generated by all of the nucleons. The characteristics of the potential fix the orbital energies and therefore the energy spacing of orbitals. The use of a harmonic oscillator potential coupled with spin-orbit term enables the reproduction of the standard magic numbers of stable nuclei. The orbitals are then spaced according to these magic nuclei, as shown in Fig. 1.5, denoted with the quantum numbers nl_j where n is the number of nodes in the oscillator, l is the orbital angular momentum of the nucleon, and j its total angular momentum. In the ground state of the nucleus, nucleons are successively filled from the lower to higher energy orbitals in agreement with the Pauli exclusion principle. Excited states can be seen as the transition of one or several nucleons to higher energy available orbitals. The shell model can calculate the filling of orbitals for excited states of the nucleus from a residual nucleon-nucleon (NN) interaction. The Shell Model hamiltonian H in the second quantization formalism is written as

$$H = \sum_i \epsilon_i n_i + \sum_{i,j,k,l} v_{i,j,k,l} a_i^\dagger a_j^\dagger a_l a_k \quad (1.1)$$

where ϵ_i are the orbital energies defined by the mean field interaction, $v_{i,j,k,l}$ are the Two-Body Matrix Elements (TBME) of the residual NN interaction between orbitals i, j, k, l , and a_i^\dagger/a_k the operator of a nucleon for the orbital i/k . The TBME determine the configuration of each excited state, i.e. the contribution from the different possible filling of the orbitals. The total

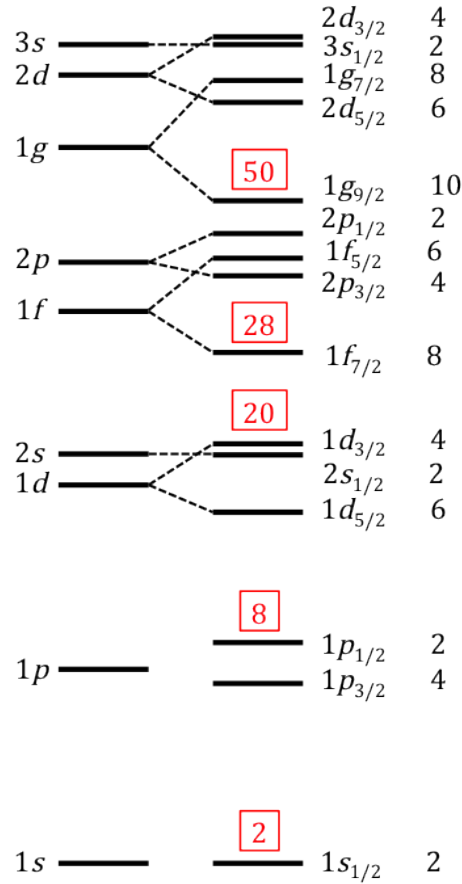


Fig. 1.4 – Shell structure of stable nuclei up to N or $Z = 50$, obtained by Goeppert-Mayer and Haxel *et al.* [3, 4].

hamiltonian can be split in a monopole (m) and multipole(M) terms:

$$\mathcal{H} = \mathcal{H}_m + \mathcal{H}_M. \quad (1.2)$$

The monopole term corresponds to a spherical Hartree-Fock description and is responsible for the global saturation properties and for the evolution of single-particle states in a spherical field. The multipole component takes into account particle-particle and particle-hole correlations with isoscalar and isovector pairing correlations, spin-isospin correlations, quadrupolar, octupolar and hexadecapolar terms.

One may infer that calculations of all the possible nucleon configurations will take a lot of time for even relatively light nuclei. The No-Core Shell Model takes into account all the orbitals and nucleons in lower-mass nuclei [17, 18]. In the standard Shell Model approach, an inert core is taken for some of the filled orbitals in the nucleus investigated, thus reducing the number of nucleons and orbitals entering in the calculation of excited states configurations. The orbitals taken into account for the calculation form the so-called valence space. As the NN interaction is not analytically known, the TBME are fixed from a model and modified afterwards empirically

to reproduce known experimental data in a localized region of the nuclear chart. Shell Model calculations are very sensitive to the valence space used, especially in the case of deformed nuclei away from shell closures or nuclei far from the valley of stability where strong reorderings of shell orbitals occur that require larger valence spaces.

Hartree-Fock mean-field theory. Effective interactions have been developed to be integrated in a Hartree-Fock mean field model, fitted to reproduce the properties of the infinite nuclear matter and the characteristics of some stable doubly-magic nuclei. The mean-field approach is based on the assumption of the independent nucleons in a constant one-body potential generated by all the nucleons. This approximation can be made thanks to the short range of the NN interaction. In this model [19], a single-particle Hamiltonian can be derived as

$$H^{HF} = \sum_{k,k'} \left(t_{kk'} + \sum_j^A \bar{v}_{kj k'j} \right) a_k^\dagger a_{k'} = \sum_k \epsilon_k a_k^\dagger a_k \quad (1.3)$$

where $t_{kk'}$ represent the single-particle configuration, and $\bar{v}_{kj k'j}$ the NN interaction between the nucleons. The A-body problem is then reduced to A analytically solvable 1-body problems. The Skyrme [20, 21] and Gogny [22] effective interactions are most often used for their capabilities to reproduce experimental data.

Collective states in spherical nuclei can be reproduced by the Random Phase Approximation (RPA) with the Hartree-Fock mean field or the Quasi-Particle Random Phase Approximation taking into account the pairing correlations [23] with the Hartree-Fock-Bogoliubov (HFB) field. In the case of deformed nuclei, associated collective states (rotations and vibrations) can be obtained by solving the Hill-Wheeler equations [24] or through a collective Hamiltonian [24, 25, 26, 27].

Modern implementations focus on optimizing directly the corresponding Energy Density Functional, therefore the connection with an underlying effective Hamiltonian is lost.

1.2.2 Direct reactions

In nuclear reactions, there are two possibilities for the nucleus: it can either form a compound nucleus, or go directly from initial to final states without the formation of an intermediate compound system. In the latter case, the reaction is a surface process, called a direct reaction [28]. In direct kinematics, the direct reaction will probe the target nucleus. However, the study of radioactive exotic nuclei prevents the creation of targets with their short lifetime. Instead, exotic nuclei are now probed in inverse kinematics, i.e. the radioactive nucleus is produced in the nuclear physics accelerator and transported up to the reaction point with a target containing the probe of interest, such as protons or α for example. The nucleus ejected after the reaction is identified at this stage to distinguish the reaction of interest.

Direct nuclear reactions are used to probe the low-energy structure of the nucleus such as radius, density, and first excited states spectroscopy. They regroup: (i) the elastic scattering (protons (p, p), neutrons (n, n), or α particles (α, α) for example) where no nucleon nor energy are exchanged in the reaction, to probe the radii of nuclei. (ii) The inelastic scattering of nuclei ((p, p') , (α, α') or ($^{208}\text{Pb}, ^{208}\text{Pb}'$) for example) where only excitation energy is transferred during the reaction, putting the nuclei in an excited state, probe the collective structure of the excited

state and its excitation energy. The inelastic scattering of protons or neutrons can probe the neutron and proton transition densities and therefore the nature of excitation when compared to Coulomb excitation experiments. (iii) The transfer of one or two nucleons for a low energy of around 5 to 50 MeV/nucleon can provide a lot of information on the populated excited states: absolute excitation energies of the excited states, wave functions of both the initial nucleus and the measured excited states. Finally (iv) the knockout of one or two nucleons at higher energies from about 50 to 1000 MeV/nucleon are very useful for the first spectroscopic studies in inverse kinematics at NSCL(USA), GSI(Germany), or RIBF(Japan) of very exotic nuclei. Because of the intermediate energy, thick targets can be used to balance with the low beam intensities.

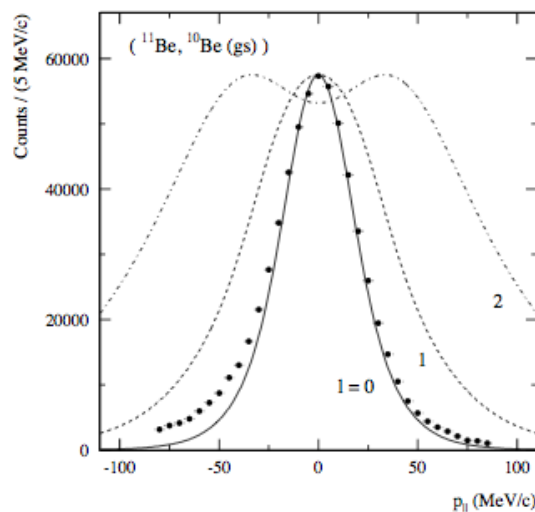


Fig. 1.5 – p_{\parallel} distribution of the ^{10}Be fragments in the rest frame of the projectile from a ^9Be ($^{11}\text{Be}, ^{10}\text{Be} + \gamma$) X neutron removal reaction at 60 MeV/nucleon. Only the contribution leading to the ground state of ^{10}Be is shown. The curves are calculations assuming a knockout reaction from s, p, and d states. Figure taken from Aumann *et al.* [29].

Knockout reactions of one or two nucleons is treated in the literature as a direct process with the eikonal and sudden approximation. Under this assumption, the momentum distribution width of the ejectile, core nucleus ejected after the reaction is then the image of the intrinsic momentum of the knocked-out nucleon [30]. As an illustration, However, the precise mechanism of heavy-ion induced knockout is still an open question in case of low incident energies and a deeply-bound knocked-out nucleon [31, 32]. The use of a hydrogen target is thought to lead to a cleaner proton-induced reaction process for both transfer and knockout reactions [33]. We will focus on the knockout of protons from a very neutron-rich nucleus.

An approach that has been successfully used in the past for proton-induced knockout is the Plane Wave Impulse Approximation (PWIA). It is a one-step removal process describing the nuclei involved in the reaction as plane waves in a non-relativistic frame as $\exp(-i\vec{p}\cdot\vec{r})$ with the momentum \vec{p} and direction \vec{r} of each nucleus. The THREEDEE code [34] developed in the 1980s has often been used to describe knockout reactions in this framework.

To reproduce $(p, 2p)$ and (p, pn) knockout reactions measurements, three new codes have been developed recently: (i) the new Distorted Wave Impulse Approximation (DWIA) code developed by K. Ogata (RCNP, Japan) for $(p, 2p)$ reactions [35], (ii) the Faddeev-Alt-Grassberger-Sandhas reaction framework of R. Crespo (IST, Portugal) [36], and (iii) the eikonal/DWIA formalism for $(p, 2p)$ reactions from C. Bertulani (Texas A&M, USA) [37].

1.3 Very exotic nuclei and MINOS

1.3.1 First spectroscopy of very exotic nuclei

The study of very exotic nuclei at the limit of the accelerator capabilities is an experimental challenge but also a real gain in very scarcely known regions of the nuclear chart. The Radioactive Isotope Beam Factory (RIBF) of RIKEN in Japan [38] is the first constructed new-generation nuclear physics accelerator in the world with the highest radioactive beam intensities achieved so far. It is operational since 2007.

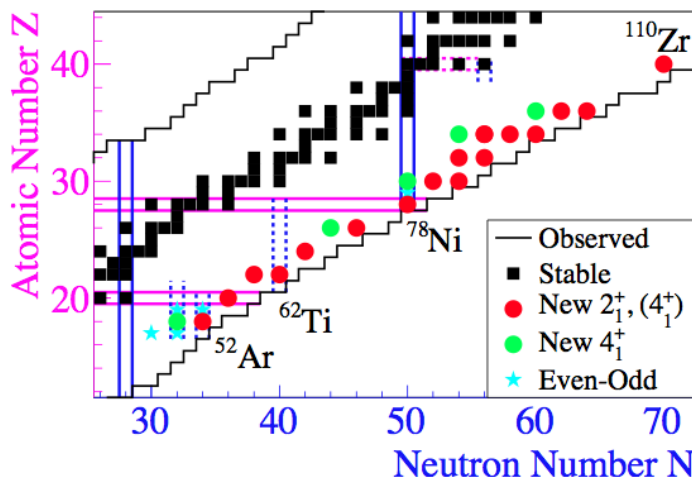


Fig. 1.6 – Overview of the 16 new $E(2_1^+)$ and at least 5 new $E(4_1^+)$ measurements foreseen within the SEASTAR project.

The Shell Evolution And Search for Two-plus states At the RIBF (SEASTAR) [39, 40] is a physics program to systematically measure all 2_1^+ states up to $Z = 40$ accessible with the presently available ^{70}Zn and ^{238}U primary beam intensities at the RIBF, as shown in Fig. 1.6, with the measurement of sixteen new $E(2_1^+)$ and at least five new $E(4_1^+)$ states. It includes the study of (i) the neutron sub-shell closure below ^{54}Ca (^{52}Ar), (ii) correlations in Ca isotopes beyond ^{54}Ca (^{56}Ca), (iii) the $N = 40$ "Island of Inversion" for lower proton number ($^{60,62}\text{Ti}$), (iv) the collectivity evolution beyond $N=40$ (^{66}Cr , ^{72}Fe) (v) the persistence of the $N=50$ shell closure (^{78}Ni), (vi) the orbital migration beyond $N = 50$ ($^{82,84}\text{Zn}$, $^{86,88}\text{Ge}$, $^{90,92}\text{Se}$), (vii) the rise in collectivity at $N=60$ and beyond (^{94}Se , $^{98,100}\text{Kr}$), and (viii) the $N = 70$ sub-shell closure (^{110}Zr).

For the spectroscopy of such nuclei produced at a few or tens of particles per second, the

use of a standard thin Be or CH₂ target would not give enough statistics in a few days time for each beam setting. To increase the luminosity, i.e. reactions, i.e. γ -rays produced, A. Obertelli (CEA) thought of using a thicker target of liquid hydrogen with proton knockout reactions. Using a target of 100 to 200 mm thickness to optimize the luminosity with respect to re-interaction in the target, the energy loss in the target becomes considerable at the RIBF energies. For example, a ^{66}Cr beam of around 250 MeV/nucleon at the beginning of the target will have only 200 MeV/nucleon or so after the target. At these energies, the Doppler effect is important with the detection of γ -rays. Therefore, the vertex position inside the target needs to be known. For this, a vertex tracker is developed to be put around the hydrogen target for $(p, 2p)$ knockout reactions. The combination of the target and detector is called MINOS (MagIc Numbers Off Stability), funded by an ERC Starting Grant from November 2010 [41, 42].

The design and simulations for the detector have been conducted until mid-2012. First tests on a detector prototype were conducted from mid-2012 until the construction and validation of the first real detector from April-May 2013. The detector and target were then shipped to Japan in October 2013 when first in-beam tests were taken at the HIMAC medical facility [43] to validate the performances of the vertex tracker.

In May 2014, the first physics experiments were performed successfully as the first SEASTAR campaign with a ^{238}U primary beam obtaining the first measurement of ^{66}Cr , $^{70,72}\text{Fe}$, and ^{78}Ni . A second SEASTAR campaign took place in May 2015 with a ^{238}U primary beam on the higher-mass nuclei up to the ^{110}Zr first spectroscopy. Other experiments aiming at the di-neutron correlations in halo nuclei [44] and the invariant mass measurement of ^{28}O [45] have been accepted by the Physics Advisory Committee of RIKEN, with the experiment on halo nuclei proposed by Y. Kubota (CNS, University of Tokyo) and A. Corsi (CEA) [44] took place in November 2014. A last SEASTAR campaign is also planned with the measurement of the remaining lower-mass nuclei with a ^{70}Zn beam.

My thesis focuses on the development, tests and first physics experiments at the RIBF with the spectroscopy of ^{66}Cr .

1.3.2 Island of Inversion

N=20 Island of Inversion. In 1975, the first excited state of ^{32}Mg was measured by β -decays of Na isotopes [5, 6]. This N=20 nucleus was indicated to be deformed from its low excitation energy. A lot of experimental studies have since then been performed to characterize the region with binding energies [46, 47], neutron separation energies [48], mass measurements [49], excitation energies [5, 7, 50, 51, 52, 53, 54, 55], and Coulomb excitation experiments [56, 57, 58, 59]. In this region, two-particle two-hole ($2p2h$) configurations are favored over normally-filled orbitals: this was defined as an *Island of Inversion*. This N=20 region was investigated with shell model calculations to understand the mechanism for such an onset of collectivity: a collapse of the shell ordering was found [60], confirmed with the comparison of excited states [61] and binding energies [62] to shell-model calculations. This N=20 region has been studied to define the contours of this Island of Inversion and an extension up to N=26 was found for the Mg isotopes [63], leading to believe that both $^{32}_{20}\text{Mg}$ and $^{40}_{28}\text{Mg}$ [64] are in the Island of Inversion. Inversely, for the Si chain this Island is not continuous for N=20 to N=28 as $^{34}_{20}\text{Si}$ is magic [65] while $^{42}_{28}\text{Si}$ is deformed [11]. The experimental data is shown in Fig. 1.3 with

the 2^+ and 4^+ energies of Si and Mg isotopes. Beyond mean-field calculations have also been performed in this region of deformation to understand the mechanisms behind it [66].

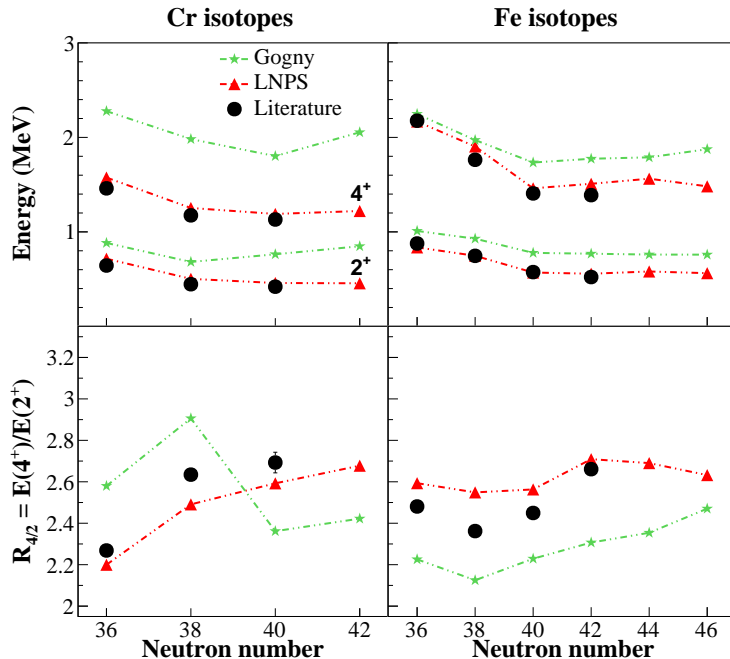


Fig. 1.7 – Systematics of Cr and Fe isotopes compared to the shell model calculations using the LNPS interaction [67], and also to the Hartree-Fock-Bogoliubov + 5-dimension Collective Hamiltonian calculations using the Gogny D1S force [68, 69].

N=40 Island of Inversion. In the Fe and Cr isotopes below Ni, an onset of collectivity towards N=40 has been found, summed up in Fig. 1.7 with the experimental known data. The first measurement in this region has been performed on ^{66}Fe from β -decay at CERN [70] and showed for the first time an onset of collectivity with the drop of the 2_1^+ state at N=40 instead of the increase seen in ^{68}Ni . At GANIL, the 2_1^+ state energy of ^{62}Cr was also measured from β -decay with the lowest energy in this mass region. In analogy to the N=20 region, an inversion mechanism at N=40 was explained in terms of nuclear forces. For more neutron-rich Cr and Fe isotopes, β -decay measurements are then limited by the evaporation of a neutron which enforces the production of even more neutron-rich nuclei to obtain the nuclei of interest after β -n reaction and proton knockout experiments become more competitive in this region [71].

This sudden onset of deformation along the Fe chains has also been inferred from recent lifetime and $B(E2; 0_1^+ \rightarrow 2_1^+)$ measurements on $^{64,66,68}\text{Fe}$ [72, 73, 74]. These two different observables, supported by mass measurements [75], demonstrate an increase of collectivity for both Cr and Fe isotopes beyond N=38. The even-even Cr isotopes have known first 2_1^+ and second 4_1^+ excited state energies up to ^{64}Cr at N=40 with the Cr 2_1^+ energies decreasing beyond N=32 [76, 77] and the lowest 2_1^+ energy measured at 420(7) keV for the N=40 ^{64}Cr [78]. The $B(E2; 0_1^+ \rightarrow 2_1^+)$ reduced transition probabilities have been measured up to N=40 also with $^{58,60,62}\text{Cr}$ in Ref. [79, 80] and ^{64}Cr in Ref. [74]. The scarce experimental data available on neutron-rich Cr and

Fe isotopes around N=40 do not show a maximum in collectivity. This N=40 region has a behavior similar to the Mg isotopes at N=20 and N=28 and has therefore been claimed as an Island of Inversion for the Cr and Fe isotopes [72, 76].

Shell model calculations in the N=40 region below Ni with a $pf g_{9/2} d_{5/2}$ valence space for neutrons and pf valence space for protons outside a ^{48}Ca core [67] showed significant neutron excitations above the $1g_{9/2}$ orbital to its quadrupole partner $2d_{5/2}$ and claimed an Island of Inversion for Fe and Cr isotopes at N=40. Beyond-mean field calculations based on a collective hamiltonian deduced from the Gogny D1S interaction [81, 82] lead to similar predictions.

From measurements, this N=40 pf neutron shell closure is marked in ^{68}Ni with a high excitation energy of the 2_1^+ state [83] and a small $B(E2; 0_1^+ \rightarrow 2_1^+)$ value [84]. However, mass measurements show that the N=40 gap is weak for ^{68}Ni [85, 86] and the low $B(E2; 0_1^+ \rightarrow 2_1^+)$ value in ^{68}Ni can be due to a N=40 shell closure but might also come from a neutron-dominated excitation [87].

Therefore, the question remains: do the heavier Cr and Fe isotopes mimic the merging found in the Mg isotopes between N=20 and N=28, or does the N=50 shell closure persevere below ^{78}Ni [88] ?

CHAPTER 2

MINOS : conception and validation

The MINOS device is composed of a liquid hydrogen target and a Time Projection Chamber (TPC). It is dedicated to proton-induced nucleon knockout experiments. A sketch of MINOS is shown in Fig. 2.1. In this chapter, the target, the TPC, the electronics, and the data acquisition system are presented. The first tests with an alpha source and cosmic rays as well as physics cases simulations to characterize the detector are detailed.

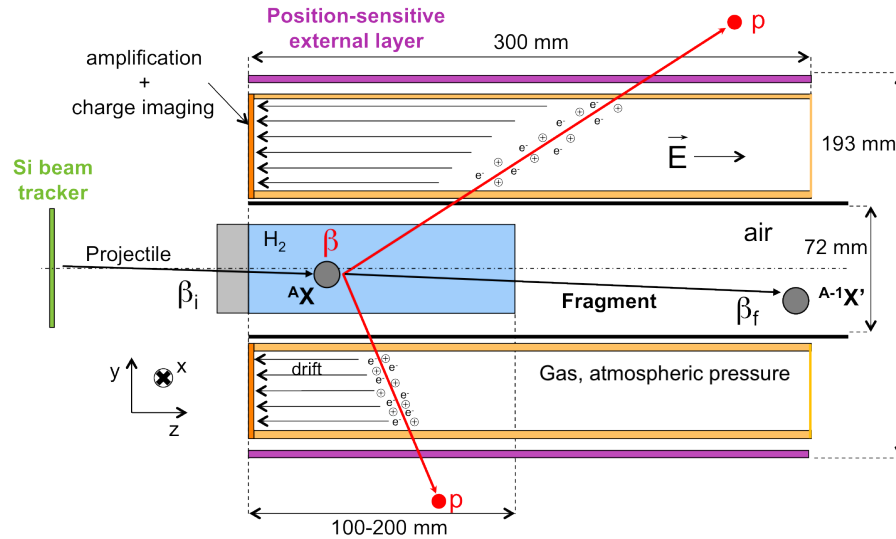


Fig. 2.1 – Principle scheme of the MINOS device.

2.1 General description

2.1.1 Liquid hydrogen target

The Magnetism and Cryogenics laboratory (SACM) of CEA-IRFU developed several liquid targets in the past for different experiments such as Polder at Jefferson Lab in 1996 or the PRESPEC Collaboration at GSI in 2011 [89, 90]. The MINOS target design is greatly inspired from the PRESPEC target [89], aiming at minimizing the amount of hydrogen in the system for safety reasons. It is composed of: (i) a cold part with the cryostat and the liquid target inside a beam pipe in vacuum located in the experimental area in Fig. 2.2, (ii) a control-command

and warm hydrogen gas section with storage tank for safety. The control-command is in charge of the target control (cooling and warming up), as well as of the target monitoring and safety commands. The cryo-rack allows a safe hydrogen transfer to the target.

2.1.1.1 Target cell



Fig. 2.2 – (Left) Front view (from downstream) of the target during the filling phase. The liquid-gas interface of hydrogen is clearly visible. (Right) Front view of the target cell mounted on its aluminum support with the supply and exhaust tubes for hydrogen.

The target cell, shown in Fig.2.2, is made of polyethylene terephthalate (PET) films (denoted hence as the trademark Mylar) sealed on a stainless steel target holder with an elastic glue withstanding low temperatures. Two pipes through the target holder are dedicated to the hydrogen supply and exhaust. The Mylar films are made of an entrance window of $110\ \mu\text{m}$ thickness with an effective target diameter of 39 mm, and an exit window of $150\ \mu\text{m}$ thickness, 52 mm in diameter and variable length from 100 to 200 mm. The caps are thermoformed at $160\ \text{°C}$ by mechanical stamping using dedicated tools to obtain the desired geometry.

By contraction at low temperature, internal pressure efforts could reach a maximum of 1500 mbar absolute pressure (abs) in the target. Therefore the burst pressure was checked at both room temperature and liquid-nitrogen temperature. Crash tests have been performed at low temperature with liquid nitrogen five times, and the burst pressures reached values from 5.5 bar to 6.3 bar, well above the safety rules. The pressure inside the target also causes the entrance window to curve, with a radius of curvature dictated by the internal pressure. For example, during the first SEASTAR campaign (May 2014), a pressure of 1 bar was measured during the experiment, with a H_2 density of $70.973\ \text{kg}\cdot\text{m}^{-3}$ and a 2.7 mm maximum curvature of the entrance window. During the second SEASTAR campaign (May 2015), a pressure of 500 mbar was measured during the experiment, with a H_2 density of $73.22(8)\ \text{kg}\cdot\text{m}^{-3}$ and a 1.35 mm maximum curvature of the entrance window.

The cryogenic hydrogen target is in vacuum and surrounded by a Aluminum beam pipe of 72 mm inner diameter and 2 mm thickness. During physics experiments, Mylar windows of $150\ \mu\text{m}$ thickness are put at each end of the beam pipe to pump the reaction chamber to a secondary vacuum of $\sim 10^{-6}$ mbar.

2.1.1.2 Cooling and control-command

The hydrogen is liquefied in a cryostat so that a helium supply is not needed in the experimental area. It is equipped with a cryo-cooler, i.e. a cold head on top of the cryostat and compressor in the vicinity of the cryostat. The hydrogen is liquefied in the cold head in the condenser, and falls by gravity into the target. A copper screen inside the cryostat is mounted on the cold head to protect all cold parts such as the condenser and the aluminum target support from the surrounding 300 K radiations. A good vacuum in the cryostat is achieved with a turbo molecular pump combined with a hermetic primary pump.

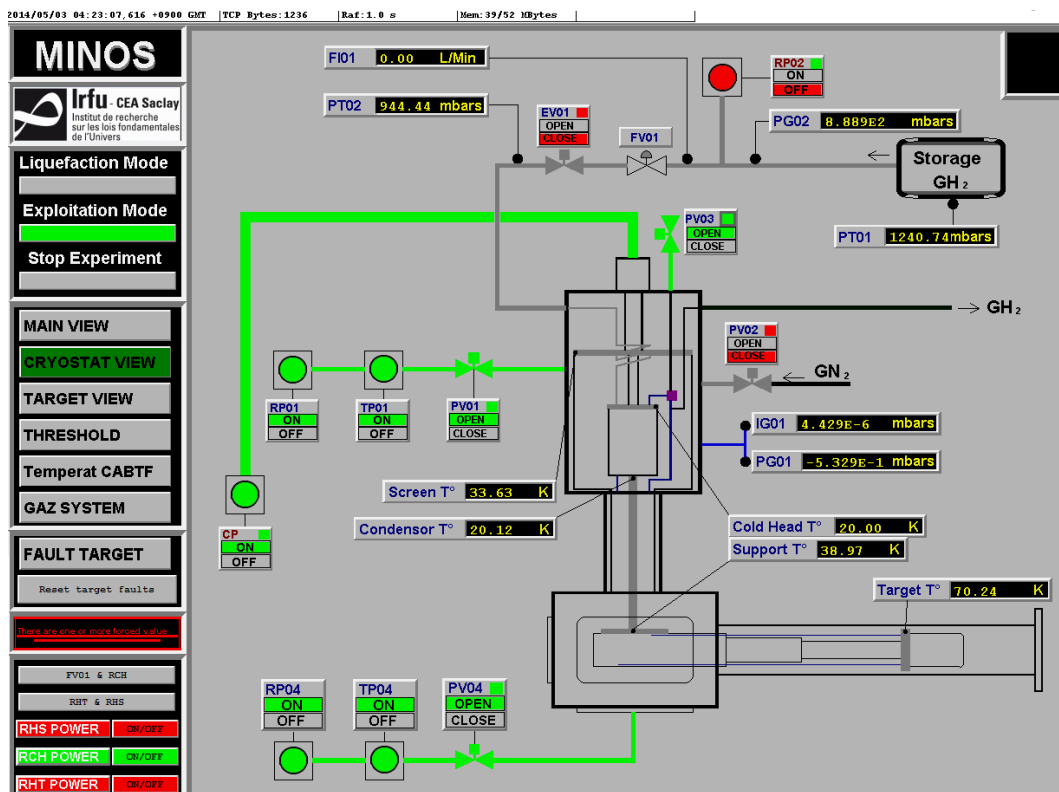


Fig. 2.3 – View of the MUSCADE control command during operation with the vacuum in the reaction chamber, target temperature and storage pressure values for control.

The MINOS control-command system is in charge of the safe operation of the target and detectors. It manages the vacuum and cryogenic system for the target and the gas system for detectors. It is composed of a logic controller which can be managed remotely via a Supervisory Control and Data Acquisition (SCADA) named MUSCADE developed by the Systems Engineering Division (SIS) of IRFU. This MUSCADE system, shown in Fig. 2.3, allows to follow in details all operations of the system and also to bring a remote assistance to users during physics experiments.

2.1.2 Vertex tracker

The MINOS tracker is a cylindrical gaseous detector composed of an annular Time Projection Chamber (TPC) surrounded by an external Micromegas tracker. The TPC is used to reconstruct the proton tracks in three dimensions and localize the vertex position in the liquid-hydrogen target. The TPC with Micromegas detectors, external tracker and electronics have all been developed at the Detectors and Computer department of CEA, the SEDI. The vertex tracker is surrounding the beam pipe as a hollowed out cylinder of 300 mm length, 80 mm inner diameter, and 193 mm outer diameter.

2.1.2.1 Time Projection Chamber

A Time Projection Chamber (TPC) is a volume of gas in which the atoms are ionized with the crossing of charged particles. Due to a strong electric field applied in the TPC (180 V/cm), ionization electrons do not recombine and drift towards the detection plane (anode). At this end plane, the electron signal is amplified in a bulk-Micromegas detector [91, 92] segmented in pads. The electrons induce a signal on a pixelated detection plane. In the MINOS TPC, the electric field is parallel to the beam direction and the cathode and Micromegas readout plane are mounted on both sides of the cylinder containing an internal and external field cage to direct the field lines in the TPC (cf. Fig. 2.1).

The γ -rays emitted from the inside of the target need to cross the TPC to be detected with a gamma detector array outside. The protons also need to cross the TPC in case of missing mass spectroscopy experiments when ancillary detectors are placed to detect the proton tracks and energies. Therefore, the TPC has to fit inside the DALI2 γ detector array [93] used during the physics experiments at RIKEN and be made of light materials. Its design has been inspired by the PANDA TPC prototype [94].

Field cage. The TPC is composed, for electric isolation and rigidity of the TPC, of internal and external concentric cylinders made of 2 mm thick Rohacell® (polymethacrylimide low density rigid structural foam) material, of 80 mm and 178.8 mm internal diameters respectively. The outer surface of the internal cylinder and the inner surface of the external cylinder are both covered by gas tight copper-stripped Kapton (polyamide) foils which define the internal and external electric field cages (manufactured by CERN).

The MINOS TPC electric field cage defines the path the electrons ionized along the proton tracks will follow towards the Micromegas readout plane. The uniformity and stability of the electric field inside the TPC is needed for a correct path analysis afterwards. The bulk-Micromegas technology described below is the best suited to maximize the uniformity in the amplification area as there is only 3.2 mm between the TPC walls and the first active readout pad. The TPC field cage is designed to reach a uniform electric field ($E_x/E_z \leq 10^{-4}$) at the first pad location. This is insured with an electric field cage made of 1 mm large strips printed with a 1.5 mm pitch on both sides of a 50 μ m thick Kapton foil for an equivalent 0.75 mm pitch between top and bottom strips. Two 3.9 M Ω surface mount resistors are soldered in parallel between one top and its adjacent bottom strip for a total of 196+195 strips and 788 resistors. The homogeneity of the field is reached at around twice the pitch of the field cage, here 3 mm from the TPC wall. A picture of the opened TPC and of the electric field cage is shown in Fig.

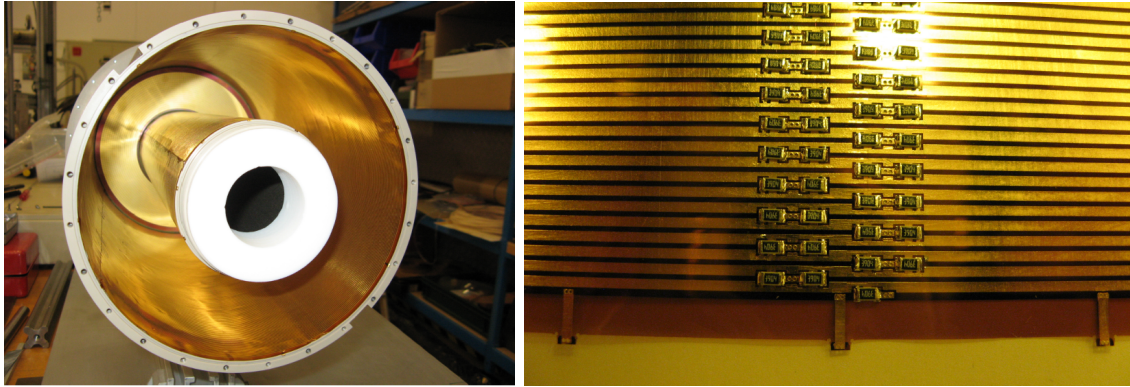


Fig. 2.4 – (Left) MINOS TPC with one side opened. The internal and external field cages are visible. (Right) Kapton foil field cage with the Copper strips and resistors in between.

2.4. The two field cages are voltage supplied in parallel through the cathode high-voltage. To improve the electric field and ensure the drift of electrons in the Micromegas region, a separate high voltage is fixed on the last strip. A CAEN SY5527 multi-channel crate is used for the high voltage supply of the Micromegas mesh, the last strip of the field cages, and the cathode.

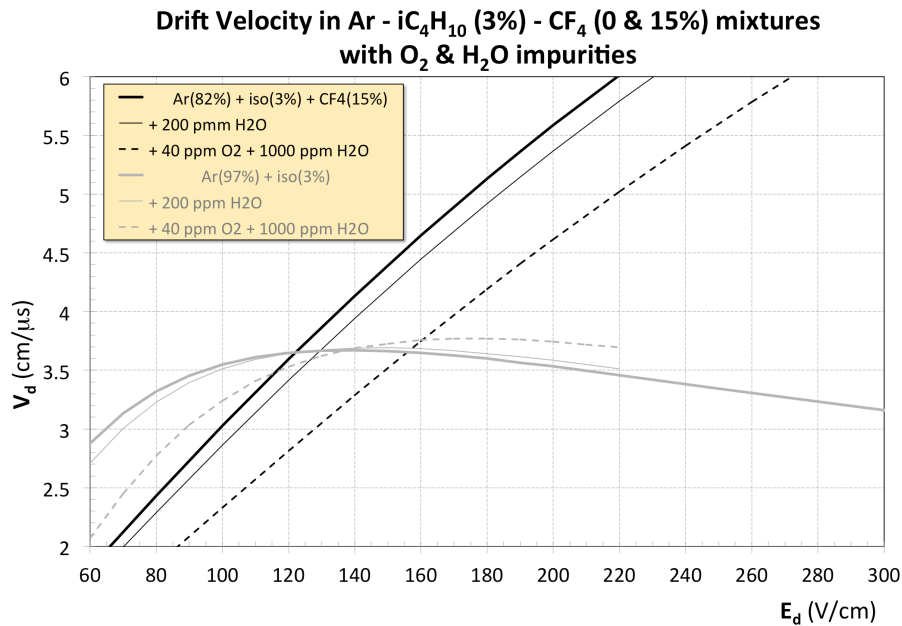


Fig. 2.5 – Magboltz simulations of the electron drift velocity as a function of the drift electric field for the two gas admixtures (in black the Ar(82%)-iso(3%)-CF4(15%) gas admixture, and in grey the Ar(97%)-iso(3%) admixture) and for different oxygen and water impurity levels. Despite the small E_d dependence of the Ar(97%)-iso(3%) gas admixture, the Ar(82%)-iso(3%)-CF4(15%) gas was favored due to its high drift velocity at $E_d \sim 200$ V/cm.

Gas. The gas for the TPC is a compromise between electron transverse and longitudinal diffusions, electron drift speed and gain in the Micromegas amplification gap while retaining a non-flammable gas. A gas mixture composed of Argon (82%), CF_4 (15%) and isobutane (3%) has been chosen for the TPC for its higher drift velocity compared to the standard Ar(97%)-iso(3%) admixture, as shown in Fig. 2.5. (i) Argon is chosen for its low average energy required to produce one ion/electron pair of 26 eV. (ii) CF_4 raises the electron drift velocity and lowers the diffusions in the 200-300 V/cm electric field range of interest. (iii) Isobutane ($\text{i-C}_4\text{H}_{10}$) is a known quencher in the amplification avalanche process required at the anode side of the TPC with the detection plane. The proportions of isobutane and CF_4 are defined from Magboltz [95] simulations and gain measurements performed with a 128 μm gap bulk-Micromegas prototype. This keeps electron transverse and longitudinal diffusions below $200 \mu\text{m}/\sqrt{(\text{cm})}$ while the Micromegas gain can reach a few thousands. The cathode plane printed circuit board (PCB) is a sandwich of two 1.6 mm thick glass epoxy layers on both sides of a 50 μm thick Kapton foil used to increase the dielectric strength of the assembly and sustain up to 9 kV cathode voltage with a sufficient safety margin as we use a typical 6 kV voltage during experiments. The water and oxygen impurities are greatly changing the drift velocity in the TPC, as shown in Fig. 2.5. It is therefore important to monitor the drift velocity and impurities during experiments.

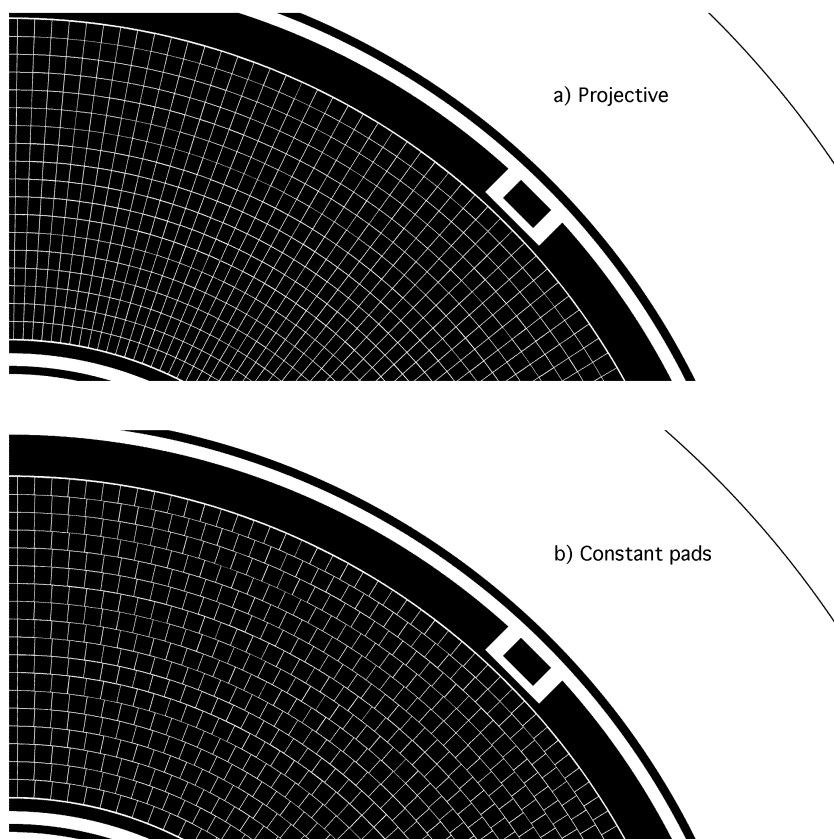


Fig. 2.6 – Micromegas pad planes with (a) projective pad geometry and (b) constant pad geometry. The Micromegas mesh rectangular connection pad is also visible.

Micromegas detector. The MINOS TPC uses the standard bulk-Micromegas with a $128 \mu\text{m}$ amplification gap [91, 92]. The Micromegas detector is a gaseous detector, sketched in Fig. 2.7. It detects the ionization electrons produced in the TPC by amplifying those charges. The detector is divided in two separate volumes by a metallic micro-mesh placed at $128 \mu\text{m}$ of the readout detection pads. This distance is called the amplification gap. The other volume is called the conversion gap, of 300 mm in our case, the length of the TPC. A voltage is applied at the mesh for the drift towards the readout plane and amplification of the electrons. Due to the small amplification gap, high electric fields are applied in this region. For the MINOS TPC, typical mesh voltages of 460 V are applied, which corresponds to a 36 kV/cm electric field. This high electric field induces a lot of amplification of the signal, called gain of the Micromegas, shown in Fig. 2.8 for the MINOS TPC.

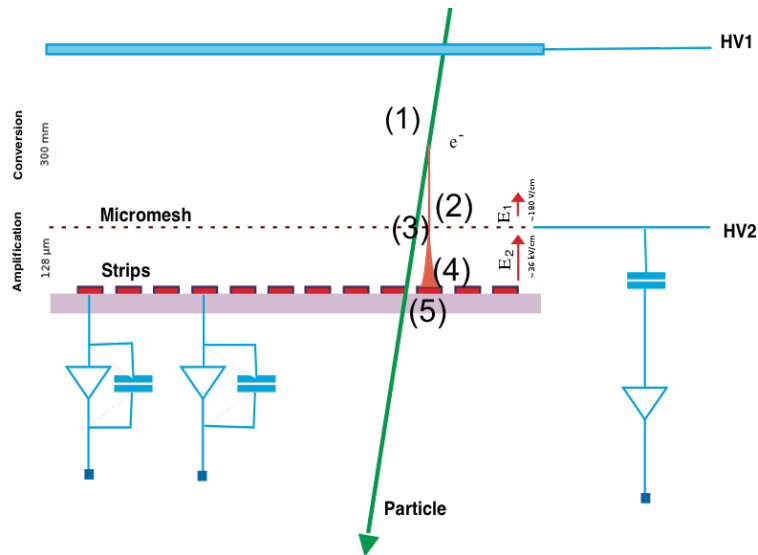


Fig. 2.7 – Sketch of the Micromegas principle.

The need for a very compact design and uniformity of performances designated the Micromegas technology for its well known robustness, simplicity and performances. The size of the pads and their geometry on the Micromegas disk is given by simulations. It is a compromise between the number of pads, i.e. electronic channels, and vertex position resolution. Full-scale GEANT4 simulations [96] were carried out by L. Audirac (post-doc at CEA-SPhN) and summarized in the MINOS review article [41]. From these simulations, two different geometries were retained. The first design is composed of 4608 pads with 18 rings of 2 mm radius containing each 256 segments in a "projective" geometry and thus has larger pads on the outer radii of the TPC than on the inner radii. The second "constant" pad geometry of 3604 pads also contains 18 rings of equal radius but the pads are constructed and placed such that all the pads have the same area of about 4 mm^2 . The two designs are presented in Fig. 2.6.

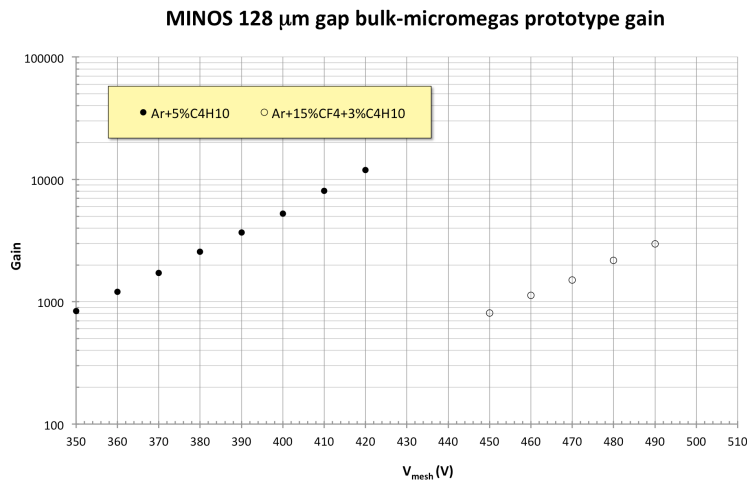


Fig. 2.8 – Measured amplification gain of the bulk Micromegas detectors as a function of the mesh potential for two different gas admixtures.

2.1.2.2 Time drift information

In a TPC, a three-dimensional (3D) recording of charged particle tracks is performed. With the Micromegas pads, a position of the track points is possible in two dimensions (x, y). The third dimension z is recovered by the drift time information. The farther away the ionization electron is from the Micromegas, the longer time it will take to drift onto the detection plane.

To recover this drift time information, we consider the TPC signals of the induced charge as a function of time for each hit pad (cf. Fig. 2.19 (b) for the pad signal). For each pad, the signal is driven by several parameters in the electronics: the shaping time, the digitization frequency and the gain. An analytical formula fitted from data for the electronic signal $q(t)$ as a function of the trigger time t_{pad} , the shaping time τ and the amplitude A can be written as:

$$q(t) = A \times e^{\left(-3\frac{t-t_{pad}}{\tau}\right)} \sin\left(\frac{t-t_{pad}}{\tau}\right) \left(\frac{t-t_{pad}}{\tau}\right)^3 + q_b \quad (2.1)$$

with the signal baseline q_b , a constant fixed by the electronics.

Therefore, by fitting the signals with this analytical function, we can extract the trigger time t_{pad} (in nanoseconds) at which the signal is produced in the TPC and the maximum of the function which is the charge q_{pad} (in femtocoulombs) deposited on the pad. The extracted time is only relative to the acquisition trigger time and is delayed by t_0 . It is proportional to the position z_{pad} along the beam direction with:

$$z_{pad} = (t_{pad} - t_0) \times v_{drift} \quad (2.2)$$

Knowing the drift velocity v_{drift} of the gas (cf. Sections 3.3.1 and 5.3 for its determination), we can deduce a three dimensional picture of charge deposition along the track in the gas volume of the TPC.

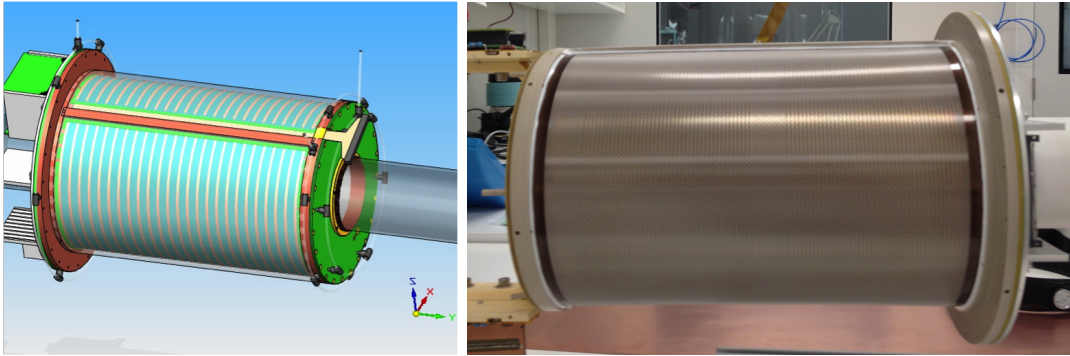


Fig. 2.9 – Design schematic (left) and picture (right) of the external Micromegas tracker without its copper shell.

2.1.3 Ancillary detectors

External Micromegas tracker. An external curved Micromegas tracker has been designed to fit on the outer side of the TPC with two half-cylinders and act as a supplementary insulator with its outer copper cathode, as shown in Fig. 2.9. This curved Micromegas is based on the CLAS12 project [97]. It is composed of a 3 mm conversion space and a 128 μm amplification gap with the anode strips orthogonal to the length of the TPC. It is supplied with the same gas admixture as the TPC in a common gas circuit. This detector aims at detecting the protons crossing the TPC to determine precisely the drift velocity at each instant and therefore monitor more accurately the possible changes in the TPC with a few 100 μm position resolution on the proton tracks. The external Micromegas tracker has not yet been used for experiments and is still under development.

Double Sided Silicon Strip Detector. The Double Sided Silicon Strip Detector (DSSSD) is a semiconductor detector from Micron of $10 \times 10 \text{ cm}^2$ size composed of 128 strips in each face, orthogonal to each other for a 560 μm pitch and detector resolution, as shown in Fig. 2.10. The detectors are used for beam tracking and can be placed at the beginning and end of the MINOS structure for a more precise beam trajectory. During the first physics campaign, one of the detectors was placed upstream of the target and TPC.

2.1.4 Electronics and data acquisition

2.1.4.1 Electronics

MINOS is a medium-size system totalizing 5376 channels: 4608 channels for the TPC in the projective geometry, 256 channels for the cylindrical trigger detector, and 512 channels for the upstream and downstream beam monitor double-sided silicon strip detectors (DSSSD).

For the readout electronics [98], the front-end cards (FECs) from the T2K experiment [99] are used. Each equipped originally with 4 AFTER chips, they are replaced for the physics experiments by the upgraded AGET chips from the GET project [100]. GET (acronym for “General

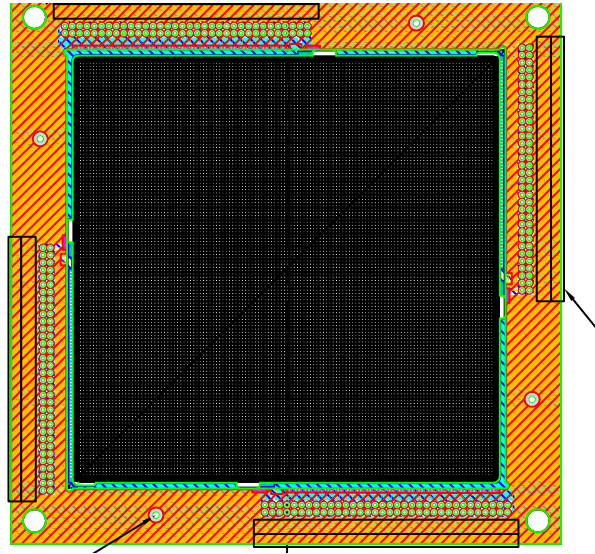


Fig. 2.10 – Design schematic of the DSSSD.

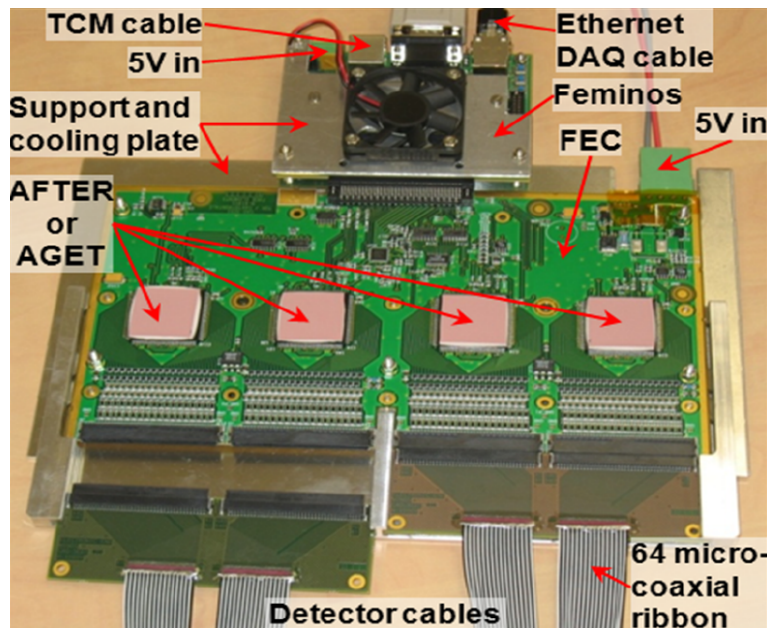


Fig. 2.11 – Picture of a FEC card equipped with AGET chips and read out by a Feminos card.

Electronics for TPCs”) is a joint project between CEA-IRFU, CENBG, GANIL (France) and NSCL (US) laboratories. The project has been funded by the French funding agency ANR and the DOE (US), with E.C. Pollacco from CEA as spokesperson. One of the differences between the AFTER and AGET chips is that all channels have to be digitized in AFTER while AGET has a discriminator on each channel that allows only hit channels to be readout, reducing the dead time accordingly. Each chip is composed of 64 channels of charge sensitive pre-amplifier

and shaper (120 fC to 10 pC range and 16 selectable values of shaping time). The data is writeable at up to 100 MHz on a 512-time bin array and readable at 25 MHz with an external ADC. Assuming an occupancy of 6 channels hit per chip, the event data acquisition rate can reach a kHz with little dead time, which is adequate to our needs. In total, a maximum of 23 FECs is used in the MINOS system. The digital part of the T2K readout system was inadequate for MINOS in terms of data rate. Therefore, a custom-made board was designed by D. Calvet (CEA-Sedi) to readout both AFTER and AGET chip based FECs, called Feminos. The Feminos cards are all synchronized to a common 100 MHz reference clock and trigger by a single card called the Trigger Clock Module (TCM) through Ethernet connections. This TCM module can receive the trigger from an auxiliary acquisition and transmits the end of acquisition, end of busy, signal. System configuration, monitoring and data merging from multiple Feminos cards to a common DAQ PC uses a Gigabit Ethernet switch and relies on the standard UDP/IP networking protocol.

The TPC pad plane is connected to the readout electronics by a set of almost five thousand 80 cm long cables. To reach the desired compactness and to maximize the signal-to-noise ratio, we followed the experience gained by internal R&D for the CLAS12 project [97] in using specially designed ribbons of micro-coaxial cables made by Hitachi Cable Ltd. The product is a flexible (less than 2.5 cm bending radius), 24 mm wide and 0.4 mm thick ribbon composed of sixty-four micro-coaxial cables. Each micro-coaxial cable is only 0.35 mm in diameter and has a very low capacitance of 50 pF/m. Two ribbons are soldered side-by-side on a PCB with connectors at each end to make a 128-channel cable assembly. In total, thirty-six 128-channel cables are needed to readout the TPC. Six additional cables are needed to readout the trigger detector and the DSSSDs. These cables are similar to those used by the TPC except for their length and connectors.

2.1.4.2 Data acquisition

The MINOS DAQ software that runs on a DAQ PC is based on a new C++ generic DAQ framework named Mordicus and written by F. Château (CEA-SEDI). Mordicus is a generic implementation of the concepts previously used to develop the DAQ software of the KM3NeT [101] and GET [100] projects. It supports standalone and coupled acquisition operation modes and provides an interface to the configuration, run control and data storage. The DAQ is composed of several processes shown in Fig. 2.12 and described below.

The Data Generator is responsible for the configuration and data acquisition of its associated Feminos board. It receives the frames containing event fragments, handles potential data loss, and sends a reliable stream of well-formed events to the Data Processor. The Data Processor receives the event streams from all Data Generators. Then it merges the events having the same event number and timestamp, coming from different sources, to create complete events containing the data of every enabled Feminos. Finally it can store these assembled events to disk. The Data Controller does not perform any data acquisition or processing, but is required to configure the TCM board. The Run Control Server is responsible for the orchestration of run operations and acts as a communication between the processes of the acquisition system and the outside world. It is also in charge of checking and synchronizing the state-machine of all the processes.

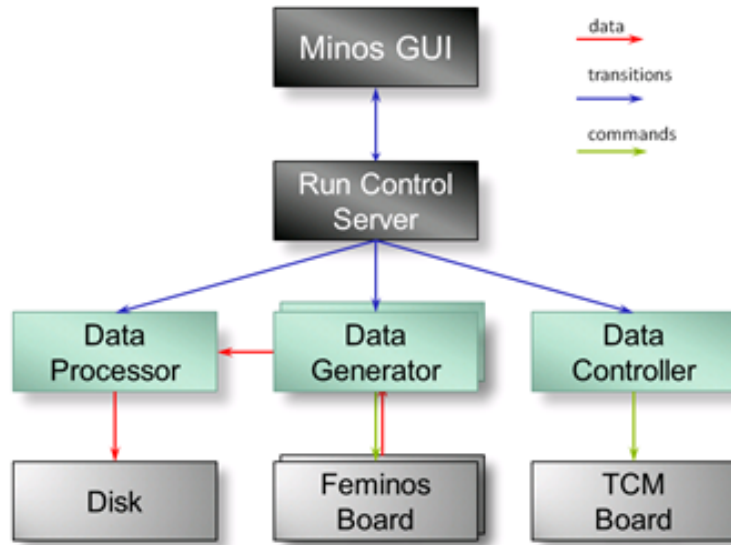


Fig. 2.12 – Scheme of the MINOS DAQ processes in a standalone operation.

The coupling to a master DAQ is described in Section 4.4 when the setup of the experiments is given.

2.2 Alpha source and cosmic bench tests

2.2.1 α source tests

In Autumn and Winter of 2012, a test chamber called MIMAC chamber has been constructed to test different Micromegas solutions for the TPC in several gas conditions, and to choose the geometry of the pads. The MIMAC chamber is composed of a steel cylinder enclosure of 50 cm length with the cathode on one side and on the other side the anode equipped with a Micromegas detector shown in Fig. 2.13 to compose a TPC. The Micromegas detector is composed of four areas with different geometries of pads, on each side of the detector disk. An ^{241}Am source of α particles of around 5.4 MeV (one with 5442.80(13) keV and another with 5485.56 keV) is inserted in the MIMAC chamber for tests.

As a first step, we have put the source inside and just triggered the acquisition with signal on the mesh in order to reconstruct the position of the source. One issue with this type of acquisition is the lack of timing for the track. The ^{241}Am source also isotropically diffuses α particles, therefore inducing another unknown variable, the incident angle of the α particles. Furthermore, α particles of 5 MeV have a range of about 5 cm in an Argon gas at atmospheric pressure, which limits the track length in the TPC. As not the total length of the TPC is hit, the drift velocity cannot be deduced from the signals to constrain the position of the tracks in length. With these two unknowns, the vertex point of the α source cannot be reconstructed without any parameters.

Assuming the source position along the length of the TPC is known, we take the spherical coordinates shown in Fig. 2.14 with z the TPC length and (x, y) the plane where the source

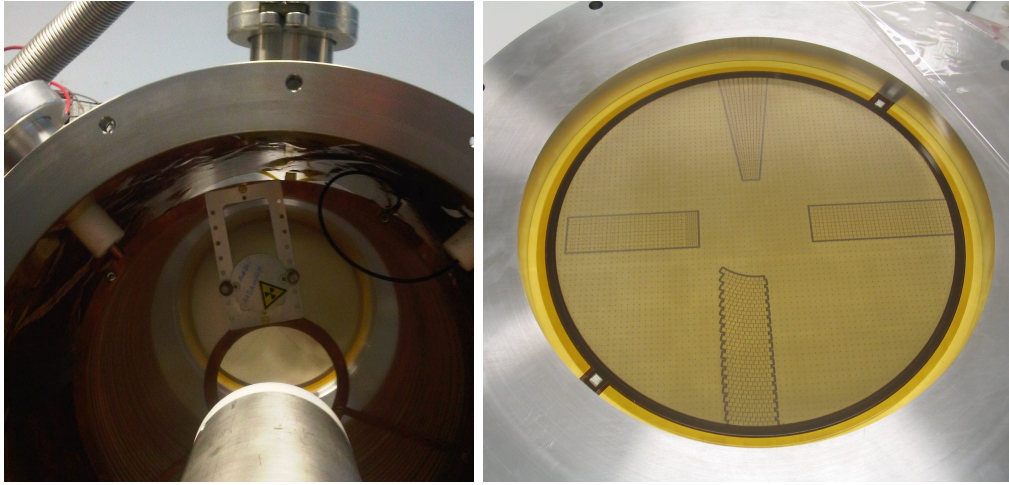


Fig. 2.13 – (Left) MIMAC test chamber when opened with an ^{241}Am source fixed with the copper rings as the outer field cage. (Right) Prototype of Micromegas detector at the end of the TPC (seen at the rear of the MIMAC chamber on the left figure) with four different geometries of pads.

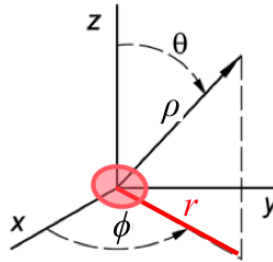


Fig. 2.14 – Reference axes for the α source test presented in Fig. 2.15 with z in the length of the TPC, and (x, y) a plane parallel to the detection and cathode planes in which the source is located (red disk). The references are transferred in spherical coordinates with (r, ϕ) the position of the source in the (x, y) plane and θ the incident angle of the α particles emitted from the source.

is located. We can apply a minimization scheme by taking different (r, ϕ) offset positions of the tracks (i.e position of the source in the (x, y) plane) in the 2D plane orthogonal to the detection plane and plotting the resulting source positions. In Fig. 2.15 are shown the results of this minimization for the best r and ϕ resolutions in source position. A cut on the higher angles of incidence θ is made (see right part of Fig. 2.15) to improve the resolution of the source reconstruction. Indeed, a zero incidence angle corresponds to a track parallel to the TPC length which doesn't produce a correct track on the Micromegas pads. Higher incidence angles therefore coincide with longer tracks produced in the TPC. We finally obtain a Full Width Half Maximum resolution on the source position of 1 mm in r and 2.7 mm in ϕ .

We have also worked for the α tests at lower pressures down to 150 mbar to obtain a larger

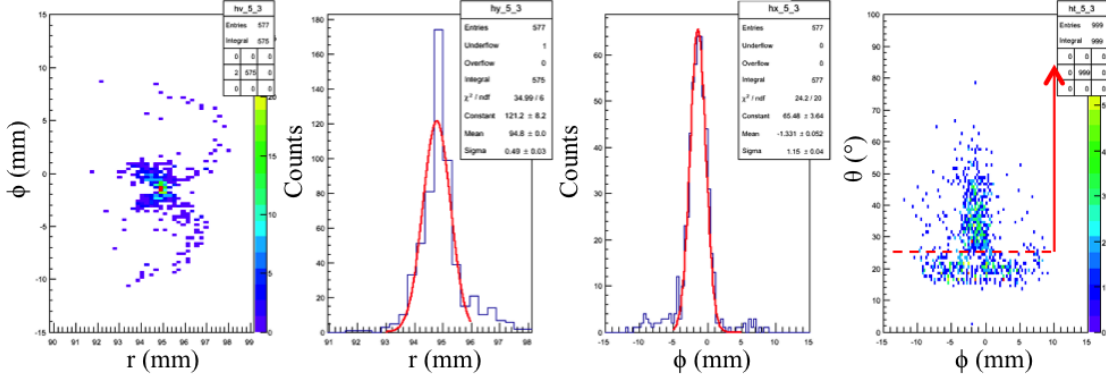


Fig. 2.15 – (Right) Incidence angle θ of the α source with respect to the angular position on the detection plane. (Left and Middle) Two dimensional and one dimensional reconstructions of the source position for incidence angles θ of the tracks larger than 25° .

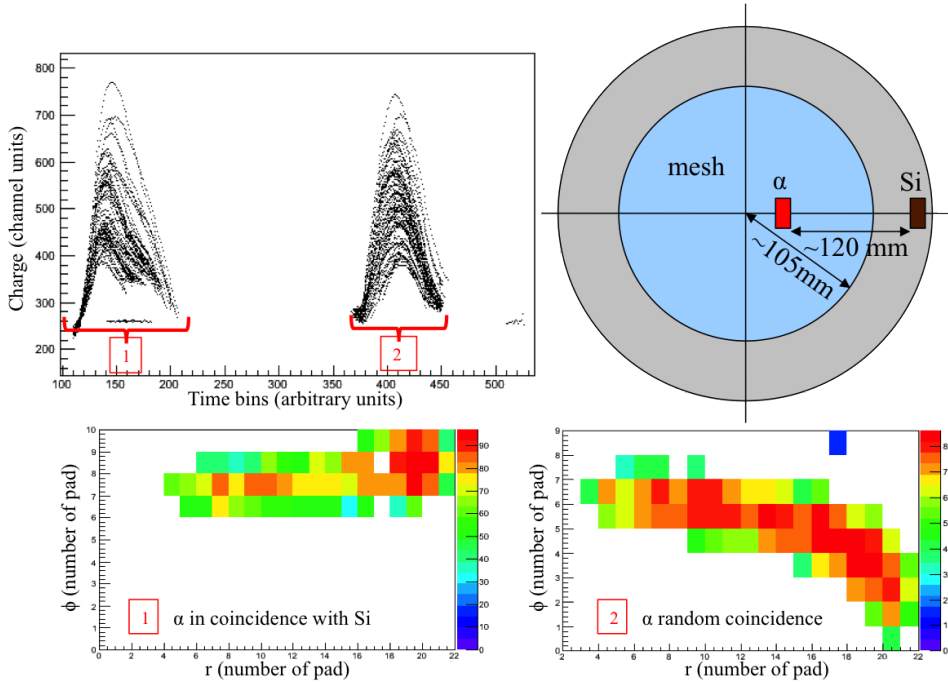


Fig. 2.16 – (Top Right) Sketch of the setup using a Si detector and an α source. (Top Left) Charge signals for an event. We distinguish two different tracks at two different times in the acquisition time, due to the large acquisition window of $10 \mu\text{s}$. The first signal (Bottom Left) corresponds to the α track in coincidence with the Si detector trigger, while the second signal (Bottom Right) is a random coincidence event.

range of the α , i.e. larger track in the TPC. A Si detector is added in the TPC as presented in the top right part of Fig. 2.16 to trigger on specific trajectories between the source and the Si

detector. We finally find tracks in the TPC, with an example shown in Fig. 2.16.

2.2.2 Cosmic bench tests

In physics experiments at the RIBF, the MINOS TPC will track protons with a maximum energy of 300 MeV, leading to an energy loss of about few keV/mm. Cosmic rays are a first validation as they have the same range of energy loss as protons with about 1 keV/mm. First tests on cosmic rays were performed with two plastic scintillators above and below the MIMAC chamber to test the validity of the setup with cosmic rays. They were successfully identified on the detection plane, as shown in Fig. 2.17.

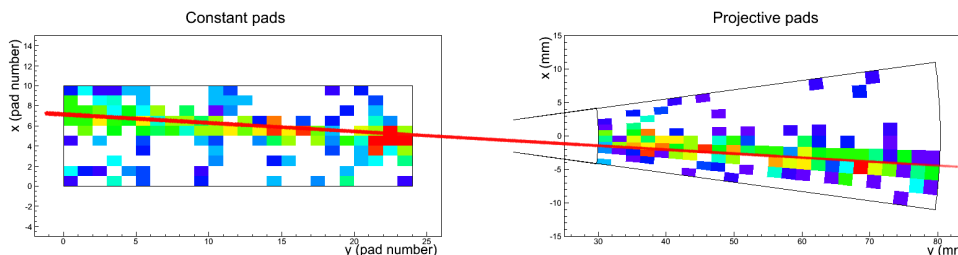


Fig. 2.17 – Figure of a cosmic ray on the detection plane crossing two different Micromegas pad planes.

The real TPC prototype has been constructed in early 2013 and validated at CEA Saclay on the CLAS12 (a hadronic physics experiment using curved Micromegas detectors) cosmic-ray bench [97] in Summer 2013. The experimental setup is illustrated in Fig. 2.18. The cosmic bench is composed of (i) two XY detection planes placed at the top and the bottom of the TPC and (ii) two plastic scintillators that are placed on the top and bottom of the whole structure. Each of these XY detection planes is composed of two $500 \times 500 \text{ mm}^2$ Micromegas detection planes, called CosMulti, composed of orthogonal strips to attain a spatial resolution $< 300 \mu\text{m}$. They are used as reference points along the cosmic ray track. The time signals of the scintillators are transmitted to a coincidence module to create the trigger of our acquisition system: the acquisition is triggered by a particle coming through both the top and bottom scintillators, thus reducing the background noise and ensuring a cosmic-ray track passing inside the bench.

The TPC is equipped with the projective Micromegas plane geometry during tests performed in Spring 2013, before sending the TPC to Japan and performing the first in-beam experiments. The signals from the TPC and from the XY detection planes were all read with the MINOS electronics composed of FEC cards equipped with AFTER chips and Feminos cards for each quarter of the detection plane.

Data taking was performed with the following settings for the electronics: 100 MHz sampling frequency, 120 fC range and 420 ns shaping time. The cathode was set to 6 kV voltage and the Micromegas stage was set to an amplification gain close to a thousand. During the data taking, O_2 impurities were maintained and checked below 60 ppm and H_2O impurities below 1000 ppm.

In a first step, raw data were extracted from the acquisition files and stored in a ROOT tree, containing simply the charge deposited in every pad of our Micromegas projective plane in our

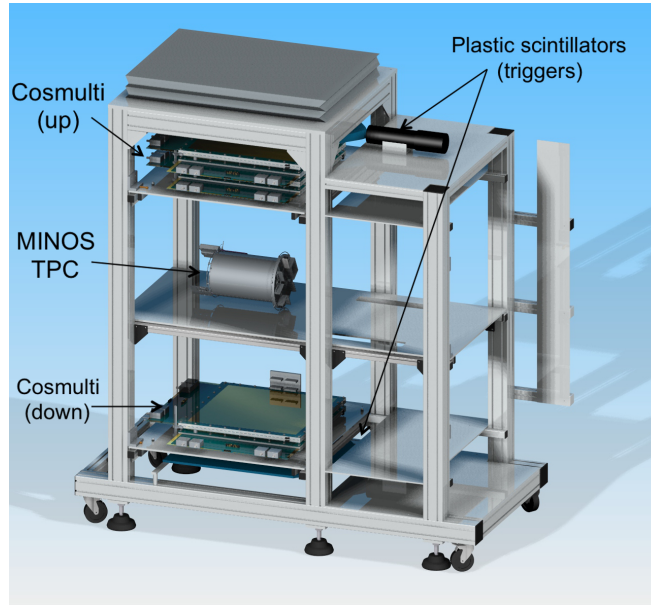


Fig. 2.18 – Artistic view of the CLAS12 cosmic bench composed of two plastic scintillators for trigger, large position sensitive Micromegas detectors interspersing the MINOS TPC. Cables and electronics are not drawn for clarity purposes.

acquisition window of $5.1 \mu\text{s}$. A fit of each pad energy signal collected over time was performed with the analytical function of Eq. 2.1.

The baseline $E_{baseline}$ was fixed in the electronics to 250 bins and subtracted from the data, which leaves two parameters to be determined by the fit: the maximum and the timing of the channel relative to the trigger received by the electronics. An example of the quality of the fit can be seen on the event shown in Fig. 2.19.

The drift velocity during these tests agrees with Magboltz simulations [95]. Fig. 2.19 (a) shows the distribution of deposited charge as a function of the z axis of the TPC. The distributions ends at 30 cm, corresponding to the length of the TPC. It shows that (i) the expected drift velocity of $4.74 \text{ cm}/\mu\text{s}$ allows to obtain the correct value of z , and that (ii) the charge collection is efficient through the whole TPC length. A typical signal collected on a pad is shown in Fig. 2.19 (b) together with its fit (Eq. 2.1). The projection of a cosmic ray track on the Micromegas plane is shown in Fig. 2.19 (c), while the 3D reconstruction of the track is plotted in Fig. 2.19 (d).

As the position of the TPC was not clearly determined during the test, aligning the MINOS TPC with the CosMulti detectors requires a five parameter minimization. In January 2014, other tests to determine the efficiency of MINOS with cosmic rays were performed by A. Corsi (CEA, France) and the engineering team of SEDI with the two scintillators above and below the TPC and a third smaller scintillator of around 25 cm length inserted partly inside the TPC in the beam pipe where the target would be placed. With a triple coincidence trigger, the cosmic ray passing through the three scintillators is then geometrically crossing the TPC. Reconstructing the tracks in the TPC with a simple three dimensional minimization, we can

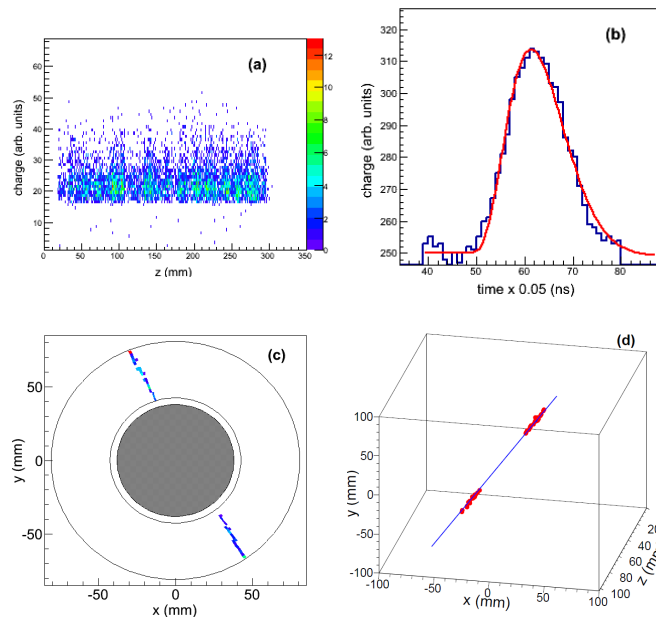


Fig. 2.19 – On the cosmic ray test bench: (a) Distribution of deposited charge as a function of the z axis of the TPC for about 2000 events. (b) Typical signal collected on a pad. (c) Projection of a track on the (x, y) Micromegas detection plane. Background events above threshold have been left on purpose and can be seen at random positions on the pad plane. (d) 3D view of the event shown in 2D in panel (c).

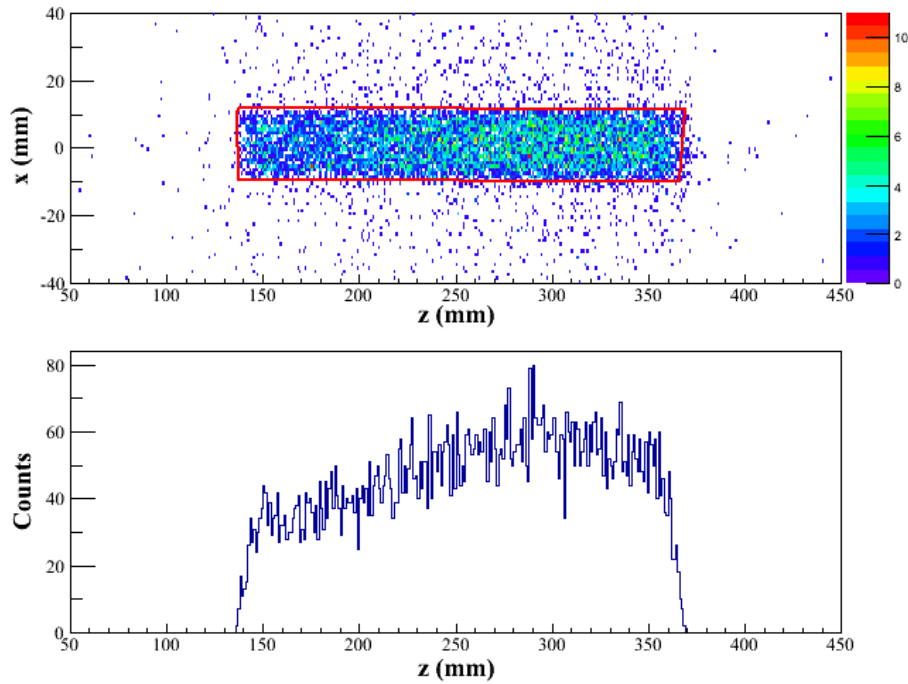


Fig. 2.20 – On the cosmic ray test bench with a thin scintillator in the beam pipe: (Top) Position on the thin scintillator plane of the reconstructed cosmic tracks in the TPC, the position of the scintillator of 25 cm length is clearly visible inside the red rectangle. (Bottom) Position of the tracks along the TPC length for tracks passing in the thin scintillator (in the red rectangle). Courtesy of A. Corsi (CEA, France).

	$^{53}\text{K}(p, 2p)^{52}\text{Ar}$	$^{79}\text{Cu}(p, 2p)^{78}\text{Ni}$
Beam energy	250 MeV/nucleon	250 MeV/nucleon
Target length	150 mm	100 mm
$(p, 2p)$ events simulated	2568 (100%)	2349 (100%)
$(p, 2p)$ events in the TPC	2473 (96%)	2295 (98%)
$(p, 2p)$ events analyzed	2361 (92%)	2195 (93%)
2 protons analyzed	1982 (77%)	1787 (76%)
1 proton analyzed	379 (15%)	408 (17%)
FWHM vertex position resolution	4.2(1) mm	4.3(1) mm

Tab. 2.1 – Simulation results for the $^{53}\text{K}(p, 2p)^{52}\text{Ar}$ and $^{79}\text{Cu}(p, 2p)^{78}\text{Ni}$ physics cases. The entrance window of the target is located at the beginning of the TPC, at the Micromegas detection plane in both physics cases. Detected events correspond to the portion of $(p, 2p)$ events that leave energy in the TPC. Analyzed events correspond to events that are fully treated by the tracking algorithm and lead to a vertex position.

plot the position of the track in the thin scintillator plane as seen in Fig. 2.20. We finally obtain an overall 73.3(7)% efficiency of the MINOS TPC for cosmic muons. A change of statistics is seen between the beginning and the end of the scintillator in the bottom part of Fig. 2.20, at [150,250] and [250,350] mm intervals, corresponding to the non inserted and inserted part of the detector in the TPC respectively. Therefore, in the beginning of the scintillator not inserted in the TPC, vertical cosmic rays with low incident angles cannot be seen in the TPC and the overall efficiency obtained is a minimum efficiency of MINOS for cosmic rays taking into account the geometrical efficiency of the setup. Considering the lower energy deposition of cosmic rays with respect to high energy protons (about 3 keV/mm) and the geometrical efficiency included in the measurement, this test with cosmic rays validates the operation of the TPC during experiments and is consistent with a 100% efficiency for protons at energies ranging from 50 to 150 MeV.

2.3 Physics cases simulations

Simulations are performed to validate the vertex positions measured during in-beam tests at HIMAC [43] and expected during physics experiments performed at the RIBF (RIKEN, Japan), as well as the detection efficiency. In the following, we present cases that are part of the RIKEN Proposal for Scientific Program (PSP) related to the search for first 2^+ states in neutron-rich nuclei [39]: $^{79}\text{Cu}(p,2p)^{78}\text{Ni}$ and $^{53}\text{K}(p,2p)^{52}\text{Ar}$ at an incident energy of 250 MeV/nucleon.

The full-scale simulations are made in three consecutive steps: (i) a GEANT4 (v10.00) [96] simulation including a reaction process (INCL v09.06.47) [102, 103] to generate events and produce the particles in the device, (ii) a Monte Carlo simulation to reproduce the drift and the amplification of the ionized electrons towards the Micromegas detection plane, (iii) the reconstruction of the vertex position via the tracking software used also for experiments, detailed in Section 3.2. Details on the simulations are given in Ref. [41].

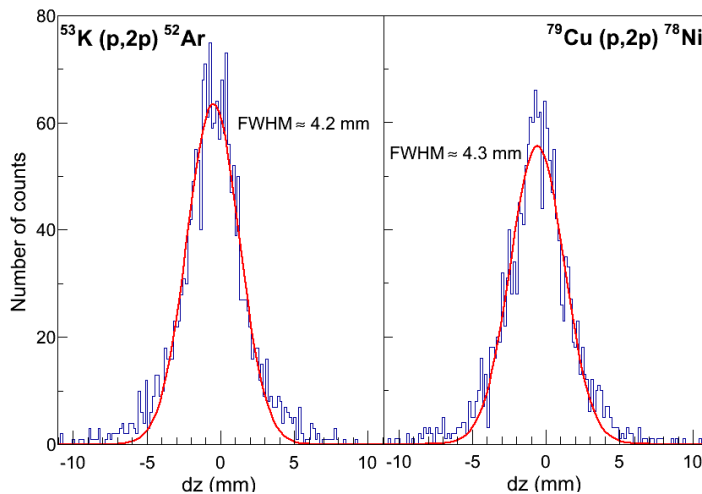


Fig. 2.21 – Difference in millimeters between the reconstructed vertex and the real vertex of the $(p,2p)$ reaction along the beam direction for the simulation of (left) $^{53}\text{K} (p,2p) ^{52}\text{Ar}$ and (right) $^{79}\text{Cu} (p,2p) ^{78}\text{Ni}$.

In the case of the spectroscopy of ^{52}Ar via $(p,2p)$ knockout, a beam of ^{53}K at 250 MeV/nucleon on a 150 mm thick LH_2 target is considered and 400 000 events are generated by GEANT4 simulations. We consider that $(p,2p)$ reactions can be identified with the identification of the beam residue as it is usually the case in experiments by use of a spectrometer downstream the target, either SAMURAI or the Zero Degree spectrometer at the RIBF. In the TPC, the gas ionization produced by proton tracks is simulated as well as the electron drift towards the detection plane. The algorithm described in Section 3.2 is used to extract the two proton events and to measure the total efficiency of the detector and the vertex resolution in the beam direction. In $(p,2p)$ physics experiments, the vertex of interaction can still be reconstructed with the detection of one proton in the TPC and the beam direction reconstructed by the beam detectors positioned before and after the setup. Out of all $(p,2p)$ simulated reactions, 92% were reconstructed with the detection of one (15%) or two (77%) protons in the TPC, demonstrating the large efficiency of the MINOS design. The rare unidentified $(p,2p)$ events correspond to a proton scattered at low energy with a second proton scattered at small angle which does not reach the TPC. Results for efficiency are summarized in Table 2.1. The reconstruction of the vertex in the case of two protons analyzed in the TPC are compared to the real position as shown in Fig. 2.21. A vertex position resolution along the beam axis of 4.2(1) mm at full-width-half-maximum is obtained. This resolution is consistent with the goal researched for in-beam γ -ray spectroscopy and will be sufficient for a correct Doppler correction in physics experiments.

From the simulations performed in Ref. [41], an important contribution to the vertex resolution comes from the angular straggling of the protons in the target. For a ^{53}K beam at 250 MeV/u kinetic energy for example, the proton tracks have an angular straggling of 1.2 mrad FWHM for a 150 mm target.

CHAPTER 3

In-beam performances at the HIMAC facility and tracking algorithm

In quasifree scattering experiments performed at energies up to 300 MeV/nucleon, protons are scattered off the nucleus with a typical energy of 150 MeV (maximum of 300 MeV), leading to an energy loss of a few keV per mm in the TPC gas at atmospheric pressure. To test the performances of the TPC, an in-beam validation experiment at several hundreds of MeV/nucleon has been performed at the HIMAC facility for heavy charged particle therapy in Chiba, Japan [43]. We first briefly introduce the experimental setup in section 3.1. The tracking algorithm developed to analyze the MINOS data is detailed in section 3.2. Experimental results and comparison with simulations are presented in section 3.3.

3.1 Experimental setup

We test the MINOS TPC at the HIMAC facility in Chiba, Japan with beams of ^{20}Ne at 350 and 180 MeV/nucleon, as well as a parasitic beam of ^4He at 200 MeV/nucleon from the CAT-TPC experiment with which we share the preparation and beam time. Instead of the thick liquid hydrogen target used in the physics experiments, two CH_2 or C targets spaced by 124 mm of 0.5 mm thickness (5.73×10^{21} atoms/cm² and 5.65×10^{21} atoms/cm² respectively) and 30 mm diameter are mounted on Plexiglass frames for an overall 40 mm diameter and placed inside an Aluminum beam pipe of 2 mm thickness and 72 mm internal diameter. The beam pipe is in air, with 1.47×10^{21} atoms/cm² in the beam pipe along the TPC length. Aluminum plates have also been used after each of the CH_2 targets to monitor the effect of the proton straggling in the plates. The overall experimental setup is presented in Fig. 3.1, with on the left a picture of the TPC, and on the right the experimental scheme.

The detector has been made and brought in two copies due to its fragility and the two corresponding Micromegas detectors have a different pad geometry (cf. section 2.1.2). The first is composed of 4608 pads in the "projective" pad geometry, and the second is composed of 3604 pads in the "constant" pad geometry. The MINOS electronics system is comprised of Front-End Cards (FEC) equipped with AFTER chips and readout with the FEMINOS dedicated cards, described in section 2.1.4, as in the tests with the alpha source and cosmic rays (section 2.2). The overall system is then synchronized via a Trigger Clock Module (TCM) which receives the external trigger. It is the first time the full electronics system has been tested, with in total 20

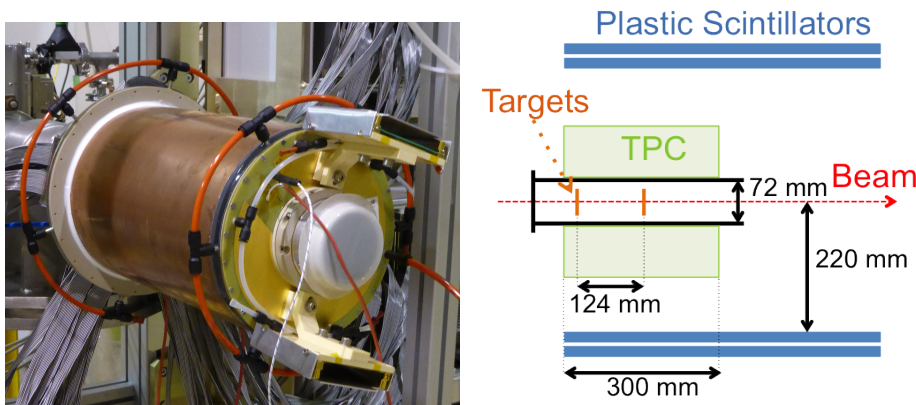


Fig. 3.1 – (Left) MINOS TPC at the HIMAC facility. (Right) MINOS experimental scheme seen from above of the in-beam test at HIMAC, with the distances in mm.

FEC and FEMINOS cards for the TPC. The electronics system is controlled with the MINOS dedicated Data Acquisition System, also tested for the first time.

Beam detectors are placed upstream the detector in the beam line: two low-pressure Multi-Wire Drift Chambers (MWDC) [104] are put for the determination of the beam position in 2D, containing three different wire planes: one with horizontal wires, the second with vertical wires, and the third with wires at an angle of 30 degrees to the vertical, in order to provide an overall position resolution of $300 \mu\text{m}$ for radioactive isotope beams with intensities of 1 MHz. Plastic scintillators are added near the MWDC detectors for beam triggering. Since the nearest MWDC is at least one meter from the detector, the vertex resolution should be less precise than with using two particle trajectories in the TPC, as found with full-scale GEANT4 simulations and presented in the following paper [41]. The MWDC detectors are not analyzed in the following and we will focus on the performances of the TPC alone.

To trigger on events where recoiling charged particles are ejected in the TPC region, two layers composed each of two plastic scintillators of 220 mm width, 630 mm length and 20 mm thickness are placed on the left and on the right of the detector. The trigger information is constructed with a signal from either one or two of the plastic scintillator layers and from either one or both of the sides corresponding to one- or two-particle events in the TPC.

The beam tracking detectors and triggers are managed with the RIBF Data Acquisition system in which we integrate the MINOS DAQ (see section 2.1.4 for a description of the system and section 4.4 for a description of the coupling between the RIBF and MINOS DAQ). $(p, 2p)$ events are not unambiguously identified due to the lack of particle identification after our setup. The vertex position resolution and the detector efficiency detailed in the following sections are consequently extracted with unidentified charged particles.

3.2 Tracking algorithm

For the tracking algorithm of the MINOS TPC the physics experiments impose several requirements. Firstly, statistics is the most important need as MINOS is used for experiments with a

very low beam intensity and therefore the software has to be as efficient as possible. Secondly, the application of a correct Doppler reconstruction implies a resolution in the beam direction for the vertex position of less than 5mm for in-beam spectroscopy experiments to compensate for target thickness effects.

3.2.1 Software description

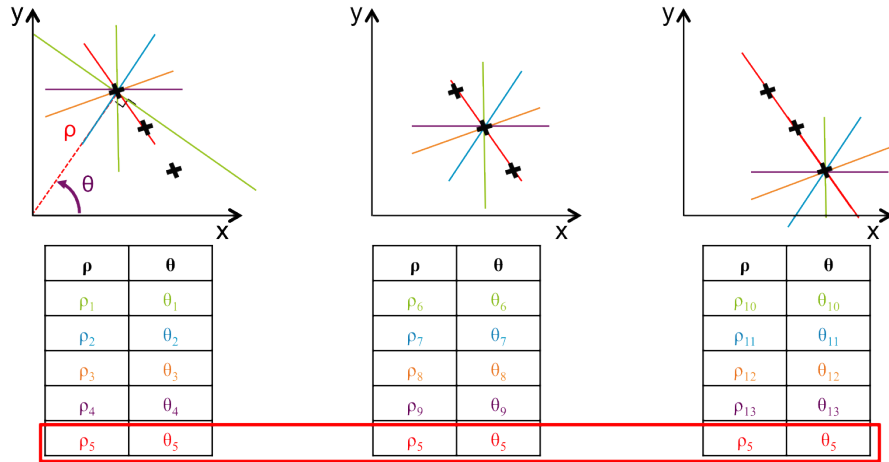


Fig. 3.2 – Principle of the Hough transform. For three points in the track (from left to right) the Hough transform scans all the possible tracks passing through this point (several shown in different colors). These tracks are defined by the minimum distance ρ to the origin and the angle θ of this minimum distance to the origin axis, presented here on the left for the red track. On the bottom part is presented schematically the parametrization of the colored tracks with the Hough transform. In the end, we look at all the different couples in the Hough space and find a common couple (ρ_5, θ_5) which corresponds to the track crossing all the points (in red). We therefore find the physical track from which the points belong to.

A first objective of the tracking algorithm is to find tracks in the data set for every event. Several methods have been applied for tracking such as a Kalman filter for the PANDA prototype TPC [94, 105] or a back-tracking of the photons with simulation-based pulse-shape analysis of the signals for the AGATA spectrometer [106]. In the MINOS TPC a longitudinal electric field but no magnetic field being applied, the tracks are linear. Moreover, there is most of the time only one reaction per event correlated to the trigger, and the tracks signal is well above the electronics noise. One needs only to find tracks (i.e. lines) in the event (i.e. image). Proposed by P.V.C. Hough in 1962 [107], the Hough transform, presented in Fig. 3.2, has been a constant source of ideas for pattern recognitions, first for the detections of straight lines [108] and then applied to the detection of arbitrary patterns [109] in images. For the recognition of straight lines in two dimensions, the Hough transform changes each point in the coordinate space into a straight line in the parameter space. Each line is specified in the real space by two parameters (ρ, θ) . ρ is the algebraic minimum distance between the line and the origin and θ the angle from this orthogonal vector and a given reference axis (cf. Fig. 3.2). The parametrization becomes unique once the angle θ is restricted to $[0, \pi]$, ρ being either negative or positive in this standard

representation.

In three dimensions, a line is parametrized uniquely by 4 parameters, which exponentially decreases the speed of the Hough transform in this space. All the signals are collected on this plane in two dimensions, consequently the number of tracks can be determined in this (xy) detection plane using the Hough transform. However, the kinematics of proton-knockout reactions in the laboratory frame is maximized at 45° coplanar protons with respect to the beam direction. The reactions taking place in the beam pipe, the knocked-out protons are then most of the time nearly collinear in the detection plane. In the application of the standard Hough transform, the two tracks being near the same line in two dimensions, they cannot be distinguished. To address this problem, I have devised a new parametrization of the Hough transform which is explained in the next section 3.2.2.

Delta electrons can be produced by materials and seen in the TPC gas. These delta electrons, along with electronics noise, can trigger some pads that will obscure the tracks with noisy signals. This resulting noisy signal can be hidden in two dimensions and one needs the time drift information, i.e. the third dimension, to disentangle the actual track from the noise. If we only use the Micromegas detection plane and consider a track with a delta electron, the fit of this track is compromised and induces a wrong vertex reconstruction. The tracking algorithm must then filter off any possible noise contributions, as explained in section 3.2.3.

Once the tracks are unambiguously selected, they can be fitted and the reaction vertex reconstructed. The general algorithm scheme and the conditions applied for the application of the tracking method (cf. Tab. A.1) is presented in Fig. 3.3 and is explained in detail in the following paragraphs.

3.2.2 Selection of events

In a first step, the charge and time information collected by each pad of the detection plane are discarded and only the position of the pads that are hit on the detector for each event are taken into account. We therefore obtain a set of (x, y) points for each event, placed in the annular disk forming the detection plane. The reactions with the target are taking place in the inner disk, either with the thick liquid hydrogen target for physics experiments or with 0.5 mm thick CH_2 targets for the HIMAC test. The wanted tracks should exclusively come from there and this restricts the Hough parametrization plane considerably, hence reducing the computing time.

As mentioned above, $(p, 2p)$ induced knockout reactions are mostly coplanar and collinear in the detection plane. If we use the standard Hough transform parametrization, two collinear tracks have the same (ρ, θ) parameters and therefore mistaking the two tracks as resulting from the same particle. This forces a change in the parametrization of the Hough transform. Each track line in the TPC resulting from a reaction in the target is instead parametrized with the angles θ_{int} and θ_{ext} of crossings to the inner and outer radii of the detection plane respectively.

To detect the straight lines in every event with this parametrization, an iteration over all possible θ_{int} is made with a chosen binning for every hit point (x, y) in the TPC. For each considered pad, there is one and only one line, parametrized as in Eq. 3.1, crossing at the same time the hit point and the point situated at the inner radius R_{int} at an angle θ_{int} , with

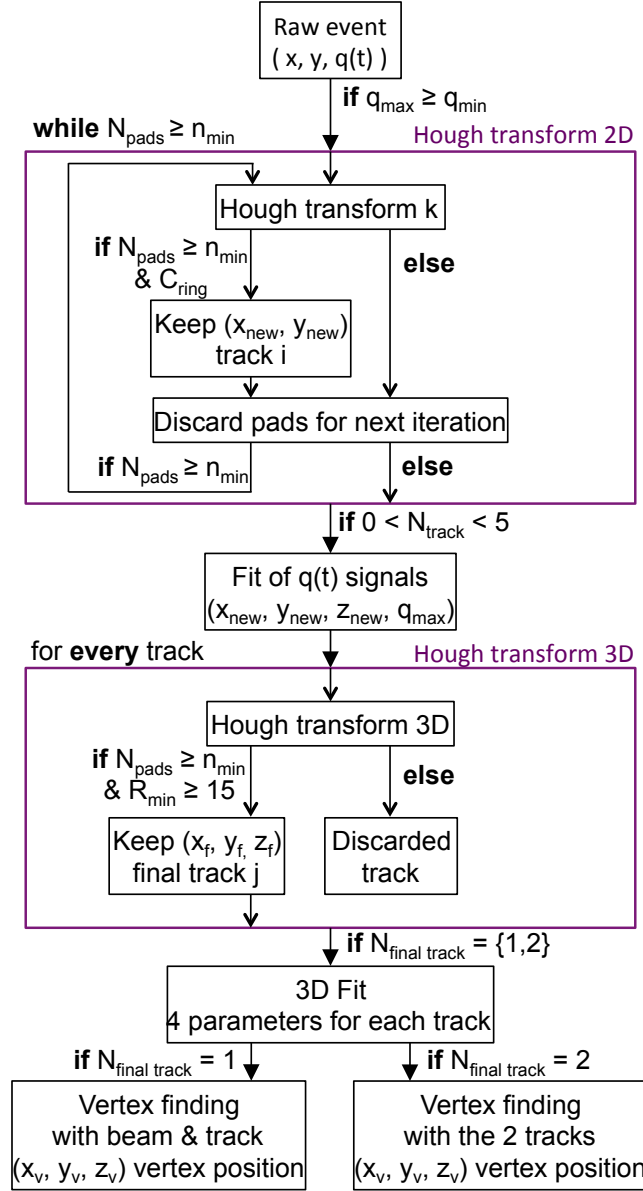


Fig. 3.3 – Scheme of the overall tracking algorithm with details on the applied conditions in Tab. A.1.

coordinates $(x_{int} = R_{int} \cos \theta_{int}, y_{int} = R_{int} \sin \theta_{int})$.

$$\begin{aligned}
 y &= p_0 + p_1 x & ; & \quad y_{int} = p_0 + p_1 x_{int} \\
 p_1 &= \frac{y_{int} - y}{x_{int} - x} & ; & \quad p_0 = y_{int} - p_1 x_{int}
 \end{aligned} \tag{3.1}$$

We can therefore calculate the point (x_{ext}, y_{ext}) at which this line will be crossing the outer radii, which will determine our θ_{ext} , by solving the following system 3.2:

$$\begin{cases}
 y_{ext} = p_0 + p_1 x_{ext} \\
 x_{ext}^2 + y_{ext}^2 = R_{ext}^2
 \end{cases} \tag{3.2}$$

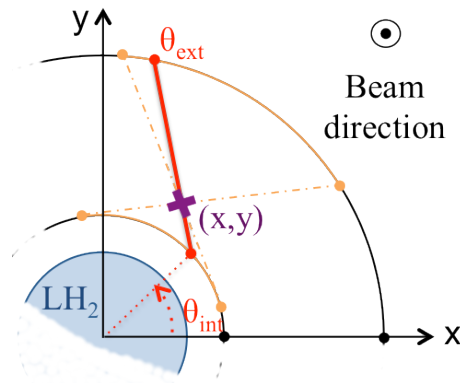


Fig. 3.4 – View of the Hough transform parameterization used with our geometrical specifications. The parameterization relies on the crossing points of the tracks with the inner and outer disks defined by the angles θ_{int} and θ_{ext} from the x axis. One possible track (in red) crossing the point (x, y) (in purple) is shown. The range of possible angles θ_{int} and θ_{ext} for this specific hit pad (x, y) are shown in orange.

θ_{ext} is deduced from Eq. 3.2 by ensuring that the two points forming the segment (i.e. track in the detection plane) are contained in the same half-disk.

We apply this iteratively and calculate all the possible $(\theta_{int}, \theta_{ext})$ combinations for all the pads hit in one event. Those values are stored in a 2-dimensional histogram where tracks are identified by maxima, as shown in Fig. 3.5. The track is considered only if it contains more than $n_{min} = 10$ pads as the physical tracks should all go through the detector. An additional condition C_{ring} is applied to make sure that at least 2 pads are hit in the four most inner rings of the TPC to cut out possible beam particles crossing the Micromegas detector, hence not coming from the target(s). Once the pads belonging to the maximum in the Hough space are identified, they are stored as a track and removed from the detection plane to apply again the Hough transform to find the next maximum in the Hough space. This procedure is applied several times until the number of remaining pads with signal is smaller than $n_{min} = 5$, while a maximum of 20 iterations is put in order to limit the computing time in case of noisy events due to sparks for example.

3.2.3 Track filtering

Once tracks are identified on the (xy) detection plane in the previous step, we can treat them in their full three dimensions by deducing the time information included in the signal of each pad as mentioned in Section 2.1.2.2 (the charge information is retrieved also at this step but is only useful in the last stage of the algorithm for the final fit of the tracks). Knowing the drift velocity v_{drift} of the gas (see Section 3.3.1 for its determination), we obtain the third z dimension of our signals with Equation 2.2. We therefore deduce a three dimensional picture of charge deposition along the track in the TPC.

To filter the possible delta electrons produced along the track (cf Fig. 3.6), we can apply standard Hough transforms in the (xy) , (xz) and (yz) planes for each track of the selected event. This filter is applied only once per track this time. The track is taken into account only if at

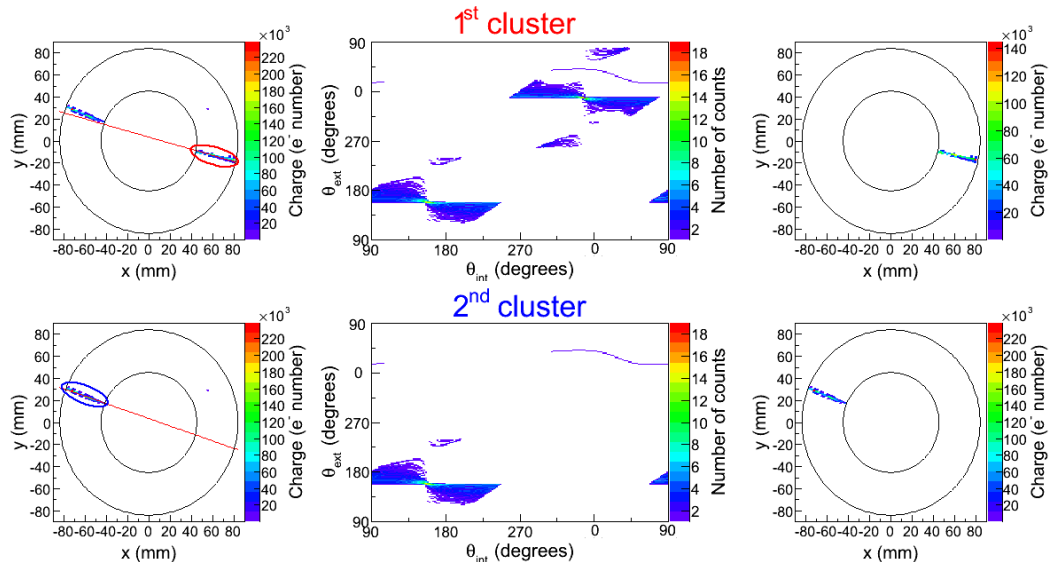


Fig. 3.5 – Two-dimensional Hough transform applied to a two-track event. From left to right is shown the hit pads before the filter, the curves in the Hough representation of the event, and finally the hit pads after filtering out the points in the new-found track.

least $R_{min} = 15$ rings (as seen in Section 2.1.2, the detection plane is decomposed in concentric of pads in both of the geometries employed) are hit when the track is not passing through the cathode. Otherwise, for low-scattering angle particles crossing the cathode, we still require the final track to contain at least $n_{min} = 10$ pads to be registered. As a result, we find the final number of tracks for each event and only the final one- and two-particle events are taken for the fitting procedure in the present analysis.

3.2.4 Track fitting and vertex finding

The energy loss in the TPC materials is negligible compared to the proton energies of ~ 150 MeV/u for a 350 MeV/nucleon beam. The charge deposition is uniform along the track. The fit of the tracks, once a correct selection and filter has been applied, can then be done with a simple minimization of each point in the track weighted by its charge in the three dimensional space. This is done by the TMinuit function [110] of ROOT.

Once we have the track parameters, we can reconstruct the interaction vertex by determining the intersection of the two proton tracks or of one proton track and the beam in case of two particles or one particle detected in the TPC respectively. The determination of the vertex position in three dimensions is done approximately, as two straight lines in three dimensions generally do not intersect. The vertex position is calculated as the mid-point of the minimal possible distance between the tracks.

To calculate the minimal distance between two lines in three dimensions, let us take two points $P_a(x_a, y_a, z_a)$ and $P_b(x_b, y_b, z_b)$ belonging to the lines l_a and l_b respectively. The distance

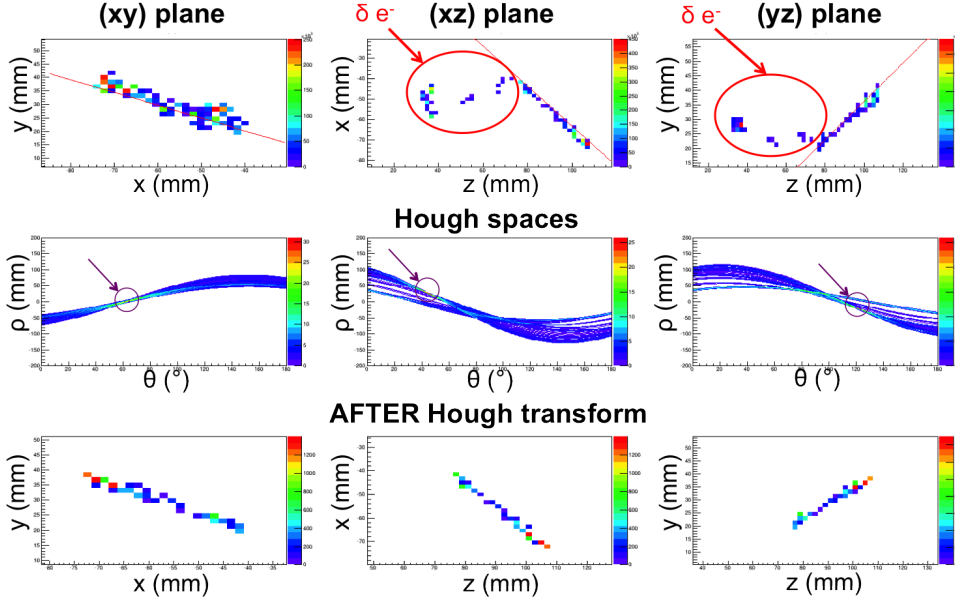


Fig. 3.6 – 3D Hough transformation showing the filtering of a track from a delta electron (circled in red on the top). From left to right is represented the three 2D Hough transformations in the (xy), (xz) and (yz) planes respectively. From top to bottom are shown the hit pads before the filter, the curves in the Hough space of the event (circled in purple are the maxima taken for the final track), and finally the hit pads after filtering.

D between P_a and P_b is then given by:

$$D^2 = (x_b - x_a)^2 + (y_b - y_a)^2 + (z_b - z_a)^2 \quad (3.3)$$

Our parametrization of the lines l_a and l_b are determined by four parameters each, in the following manner:

$$(l_a) : \begin{cases} x = p_0^a + p_1^a z \\ y = p_2^a + p_3^a z \end{cases} \quad (l_b) : \begin{cases} x = p_0^b + p_1^b z \\ y = p_2^b + p_3^b z \end{cases} \quad (3.4)$$

Applying Eq. 3.4 to the points P_a and P_b and plugging it in Eq. 3.3, we then have an expression of the distance between the two lines in function of only two variables z_a and z_b :

$$D^2 = \left((p_0^b + p_1^b z_b) - (p_0^a + p_1^a z_a) \right)^2 + \left((p_2^b + p_3^b z_b) - (p_2^a + p_3^a z_a) \right)^2 + (z_b - z_a)^2 \quad (3.5)$$

Using $p_i^b - p_i^a = dp_i$, we obtain :

$$\begin{aligned} D^2 &= dp_0^2 + (p_1^b z_b - p_1^a z_a)^2 + 2dp_0 \times (p_1^b z_b - p_1^a z_a) \\ &\quad + dp_2^2 + (p_3^b z_b - p_3^a z_a)^2 + 2dp_2 \times (p_3^b z_b - p_3^a z_a) \\ &\quad + (z_b - z_a)^2 \end{aligned} \quad (3.6)$$

With $t = z_a$ and $z_b = f(t) = f(z_a)$, we have :

$$D^2 = g(z_a, z_b) = g(t, f(t)) \quad (3.7)$$

To find the minima of the function g , we need to find the zero of the total differential of g , given by:

$$dg = \frac{\partial g(t, f(t))}{\partial t} dt + \frac{\partial g(t, f(t))}{\partial f(t)} df(t) = 0 \quad (3.8)$$

$$\Rightarrow \frac{dg}{dt} = \frac{\partial g(t, f(t))}{\partial t} + \frac{\partial g(t, f(t))}{\partial f(t)} f'(t) = 0 \quad (3.9)$$

Let us first find an expression between z_a and z_b , for example by finding the minimum of the derivative of g with respect to $f(t)$:

$$\begin{aligned} \frac{\partial g(t, f(t))}{\partial f(t)} &= 2 [p_1^b dp_0 + (p_1^b f(t) - p_1^a t) p_1^b + p_3^b dp_2 + (p_3^b f(t) - p_3^a t) p_3^b + (f(t) - t)] \\ &= 0 \end{aligned} \quad (3.10)$$

$$\Rightarrow \begin{cases} f(t) = \frac{p_1^a p_1^b + p_3^a p_3^b + 1}{(p_1^b)^2 + (p_3^b)^2 + 1} t + \frac{-(p_1^b dp_0 + p_3^b dp_2)}{(p_1^b)^2 + (p_3^b)^2 + 1} \\ f(t) = \beta t + \alpha \end{cases} \quad (3.11)$$

Now that we have found the relation for $f(t) = \beta t + \alpha$, we can use Eq. 3.11 and also calculate the derivative of g with respect to t in the same manner in order to plug them in Eq. 3.12.

$$\frac{dg}{dt} = 0 \Leftrightarrow \frac{\partial g}{\partial t} + \frac{\partial g}{\partial f(t)} \beta = 0 \quad (3.12)$$

After deriving the formulas, we finally obtain an expression for $z_a = t$ and $z_b = f(t)$:

$$\begin{aligned} z_a &= -\frac{A\alpha + C}{A\beta + B} \\ z_b &= \beta z_a + \alpha \end{aligned} \quad (3.13)$$

with

$$\begin{cases} A = \beta \times ((p_1^b)^2 + (p_3^b)^2 + 1) - (p_1^a p_1^b + p_3^a p_3^b + 1) \\ B = ((p_1^a)^2 + (p_3^a)^2 + 1) - \beta (p_1^a p_1^b + p_3^a p_3^b + 1) \\ C = \beta (p_1^b dp_0 + p_3^b dp_2) - p_1^a dp_0 - p_3^a dp_2 \end{cases} \quad (3.14)$$

These equations give us one and only one solution for the segment of minimum distance between our two tracks, and we know the exact location in space of its two points P_a and P_b , z_a and z_b with Eq. 3.13 and the other coordinates with Eq. 3.4. Therefore, we can define the vertex position (x_v, y_v, z_v) as the middle of this segment and we eventually get:

$$\left(x_v = \frac{x_a + x_b}{2}, \quad y_v = \frac{y_a + y_b}{2}, \quad z_v = \frac{z_a + z_b}{2} \right) \quad (3.15)$$

3.3 TPC performances

In the following, we present the results of the HIMAC performance tests. From the information collected by the TPC, the drift velocity is extracted for all runs in section 3.3.1. This allows us to reconstruct the hit tracks in three dimensions and apply the tracking method described in section 3.2 to calculate the resolution (section 3.3.2) which can be obtained for the vertex position. The pad multiplicity is studied in section 3.3.3 as an important parameter to check the transverse dispersion properties of the TPC gas.

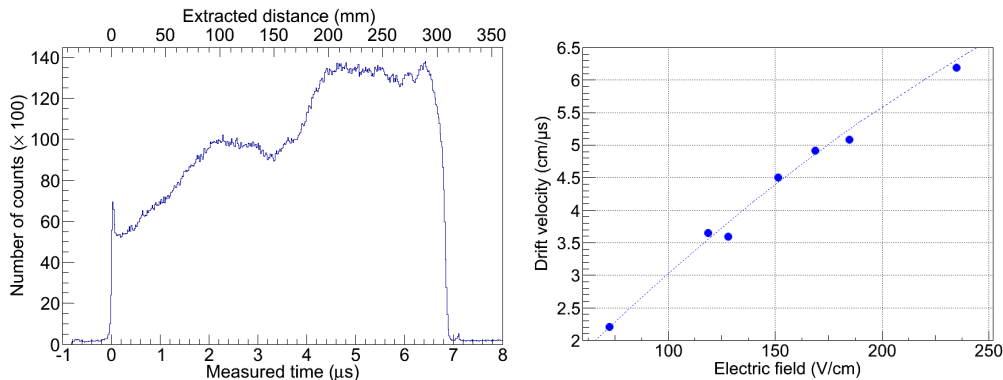


Fig. 3.7 – (Left) Measured time in μs on the bottom axis and extracted distance z along the beam line in mm on the upper axis inside the TPC for ^{20}Ne run (350 MeV/u). The time and distance 0 correspond to the Micromegas plane. (Right) Deduced drift velocity in $\text{cm}/\mu\text{s}$ as a function of the electric field applied in the MINOS TPC for several runs during the HIMAC measurements. The experimental points are compared to Magboltz simulations (dotted line) with no impurities.

3.3.1 Drift velocity

The drift velocity v_{drift} is a key parameter of the TPC and is fixed for a given electric field and gas composition including impurities (such as H_2O and O_2). As the TPC is not fully air tight, the drift velocity needs to be monitored during experiments. It is determined by using Eq. 2.2 and plotting the measured trigger time t_{pad} inside the TPC for all the events, as shown in Fig. 3.7.

This plot in terms of distances should reflect the length of the TPC for the detected hits. As a convention, we have chosen the Micromegas plane of the TPC to be the zero of the beam line axis, and therefore the statistics in the plot must start at 0 mm and stop at $z_{max} = 300 \pm 0.2$ mm. With these conditions, we can deduce the drift velocity by measuring the minimum and maximum measured trigger times t_{min} and t_{max} inside the TPC such as in figure 3.7: $v_{drift} = \frac{z_{max}}{(t_{max} - t_{min})}$. In the case of a 152 V/cm electric field and a gas mixture of Ar(82%) + CF_4 (15%) + C_4H_{10} (3%), a drift velocity of about 4.39 $\text{cm}/\mu\text{s}$ is found.

However, these drift velocities undermine the length between the two targets by 4 and 5 mm for the ^{20}Ne and ^4He beams respectively. Looking at the same run as an example, a drift velocity of 4.55 $\text{cm}/\mu\text{s}$ is needed to reproduce a distance between the two targets of 124.2(3) mm. The origin of this difference in drift velocity is under further investigation.

During the performance measurements at HIMAC, several configurations of electric field were taken, and the extracted final drift velocities are plotted in Fig. 3.7 and compared to Magboltz [95] simulations with a very good agreement consistent with no impurities in the gas of the TPC. After vertex reconstruction with the tracking algorithm, we can check that the distance between the two targets is correct. The distance between the two targets is also extracted from this graph at 124.4(3) mm in agreement with the real distance.

3.3.2 Resolutions

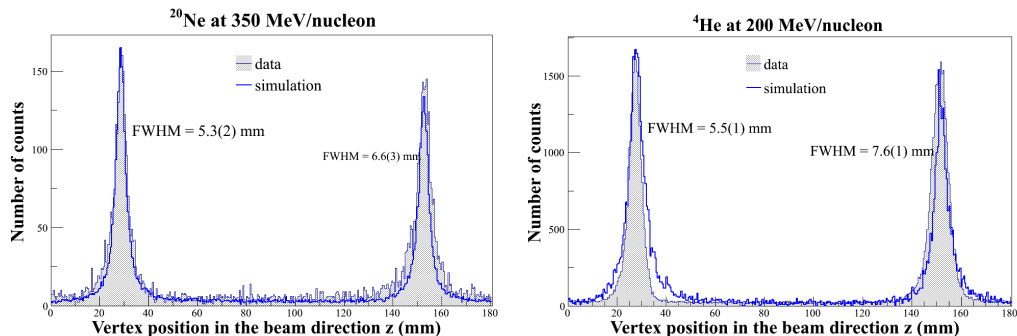


Fig. 3.8 – (Left) (Filled histogram) Vertex position along the beam axis z in mm for a run with a ^{20}Ne beam at 350 MeV/u of 20 min duration at 50000 pps and around 56 000 events with 4 tracks or less. The time and distance 0 is the position of the Micromegas plane, i.e. the beginning of the MINOS TPC. (Non-filled histogram) Results of a GEANT4 simulation performed with the same conditions on the experiment and the same software, normalized to the number of counts in the experiment. (Right) Same with a ^4He beam at 200 MeV/u of 62 min duration at 15000 pps and around 163 000 events with 4 tracks or less.

With the tracking algorithm, we can extract the vertex position for $(p, 2p)$ -like events in the case of two-particle events with the fit of the tracks and the reconstruction of the vertex point.

The resolution of the vertex position is then extracted from the vertex position along the beam line for all filtered events as shown in Fig. 3.8 on the left side for a run of ^{20}Ne beam at 350 MeV/u of 20 min duration at 50000 particles per second with two CH_2 targets placed inside the beam pipe at 124(1) mm from each other. We obtain a resolution at full-width-half-maximum of 5.3(2) mm and 6.6(3) mm for the first and the second CH_2 targets, respectively. The distance between the two targets is extracted at 124.2(3) mm.

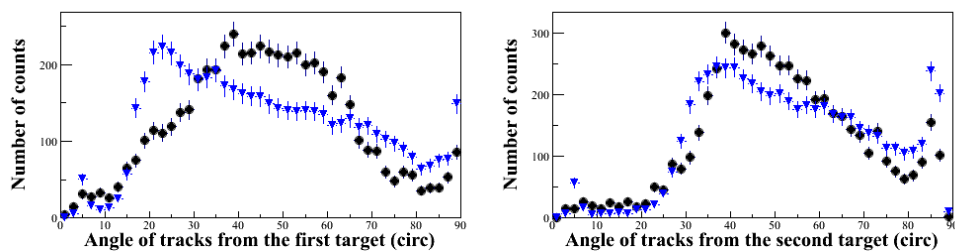


Fig. 3.9 – Angles (in degrees) of the charged particles emitted from the regions of the two CH_2 targets, on the left for the first target with $z_v=[5,50]$ mm and on the right for the second target with $z_v=[125,170]$ mm. The data points (in black) are extracted from a run with a ^{20}Ne beam at 350 MeV/u of 20 min duration at 50000 pps and compared to full-scale simulations (in blue).

The resolution of the vertex position is extracted from the vertex position along the beam line for all filtered events as shown in Fig.3.8 on the right side for a run of ^4He beam at 200

MeV/u of 62 min duration at 15000 particles per second with the same setup as above. We obtain a resolution at full-width-half-maximum of 5.5(1) mm and 7.6(1) mm for the first and the second CH₂ targets, respectively. The distance between the two targets is extracted at 123.9(1) mm.

Full-scale simulations in the same framework as Section 2.3 are performed in order to realistically compare our results. There is a fairly good agreement between experimental data and simulations. However, the simulations exhibit a poorer resolution for the first target. Intuitively, the second target should have a worse resolution because it would suffer more fragmentation events and re-interactions from the first target. This effect, in investigation, could come from a difference in kinematics. We can see in Fig. 3.9 the slight difference in angular distributions between experiment and simulation.

The runs with C targets or Al plates were not run in the same conditions because of sparking problems in the TPC. Therefore, the subtraction of the Carbon contribution to the vertex resolution cannot be performed experimentally. Simulations are underway to determine the amount of C contribution to the position reconstruction resolution.

3.3.3 Pad multiplicity

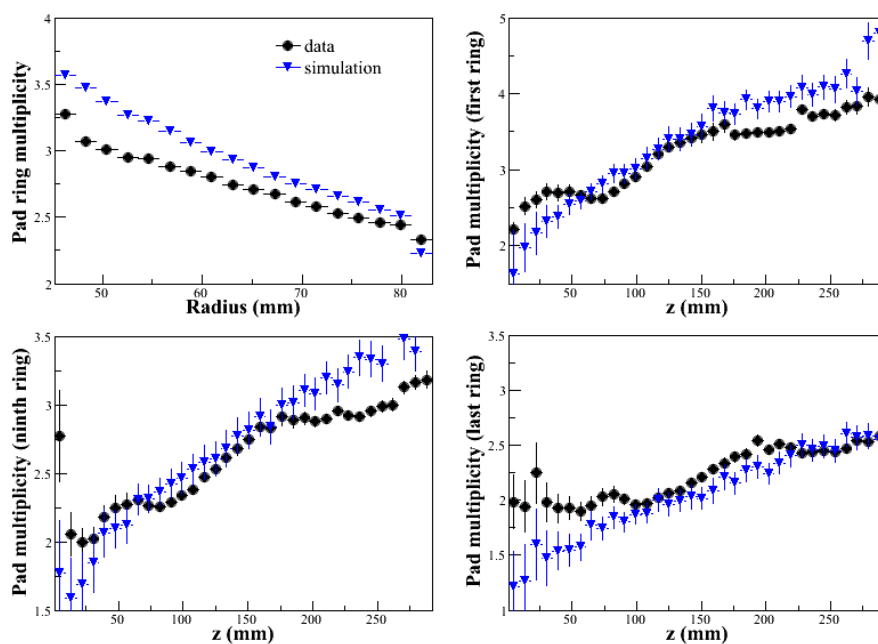


Fig. 3.10 – Pad multiplicity as a function for the experiment (in blue) and for the simulation (in black) of the radius on the Micromegas plane on the upper left. Pad multiplicity for the first, eighth and eighteenth (last) ring as a function of the position along the beam axis on the upper right, lower left and lower right respectively. This is extracted for a run with a ²⁰Ne beam at 350 MeV/u of 20 min duration at 50000 pps and around 56 000 events with 4 tracks or less.

For the projective pad geometry, we define the pad multiplicity as the number of pads hit for

each ring of the TPC annular detector. As the pads on the outer rings have a larger area, the ring multiplicity should decrease as one goes from the center of the TPC to the exterior. The ring multiplicity is extracted for each two-particle event which passed the tracking algorithm, and averaged over the number of events taken into account. Its absolute value depends on the energy threshold taken for each pad, in our case around 9 000 electrons on the detection pad. The result for a ^{20}Ne beam run at 350 MeV/u (20 min duration at 50 000 pps, with an amplification gain of the detector around 1500) is illustrated in the upper left part of Fig. 3.10 as a function of the radius of the ring. The effect of the pad size is clearly visible in this graph with a downward slope when going to the exterior of the TPC, i.e. to larger radii.

There is a specific diffusion for a given gas mixture inside the TPC, which is a function of the distance the ionized electrons have to travel in the gas. As a result, the tracks coming closer to the cathode will be more dispersed when they get to the detection plane. We have calculated the ring multiplicities for given rings (inner ring, middle ring and outer ring) as a function of the position along the beam axis of the detected point in the track. The results in the other three figures in Fig. 3.10 reveal a slight slope in transverse dispersion as we go farther from the Micromegas plane. They are compared (in black) to GEANT4 simulations and reveal a very good agreement between experiment and simulation.

CHAPTER 4

Setup of the first SEASTAR experimental campaign

The first experimental campaign using the full MINOS device with both the TPC and the liquid hydrogen target has taken place in May 2014 at the Radioactive Isotope Beam Factory in RIKEN, Japan. It is the first campaign of the Proposal for Scientific Program on the Shell Evolution And Search for Two plus Energies at the RIBF (SEASTAR). It focuses on the first spectroscopy of ^{66}Cr , $^{70,72}\text{Fe}$ and ^{78}Ni via $(p, 2p)$ knockout reactions with the DALI2 gamma detector array. The MINOS device is surrounded by DALI2 and placed at the F8 area of the RIBF facility composed of BigRIPS, a two-step separator upstream the experimental setup, and the ZeroDegree Spectrometer downstream the target, for particle identification and channel selection.

4.1 Radioactive Isotope Beam Factory

4.1.1 Primary beam production

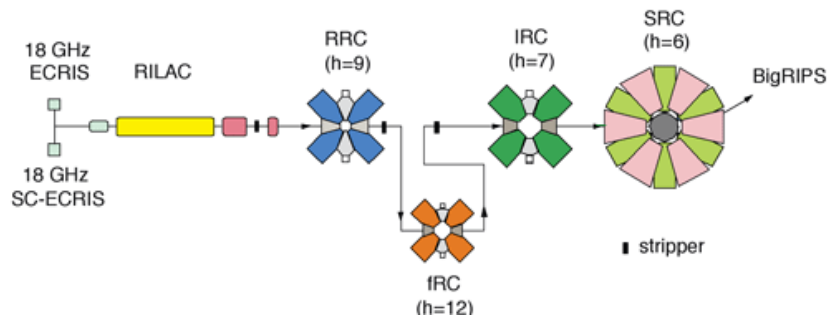


Fig. 4.1 – Scheme of the RIBF heavy-ion accelerator system in a constant energy mode of 345 MeV/nucleon.

A ^{238}U primary beam is accelerated by the RIBF heavy-ion accelerator system [38] presented in Fig. 4.1. In a constant energy mode, the primary beam is created by an ECR ion source and accelerated by the RILAC linear accelerator up to 2.5 MeV/nucleon. The produced beam is then conducted through four different cyclotrons RRC, fRC, IRC and finally the Superconducting Ring Cyclotron (SRC) to attain an energy of 345 MeV/nucleon at the injection to the RIBF

experimental beam lines shown in Fig. 4.2. Two strippers are placed after the RRC and fRC cyclotrons in Fig. 4.1. The first stripper is a He gas stripper [111] and the second stripper is a Be disk [112].

4.1.2 BigRIPS and ZeroDegree spectrometers

During the SEASTAR experiment, the BigRIPS and ZeroDegree lines [113, 114] are used, located in between the F0-F7 and F8-F11 focal planes respectively.

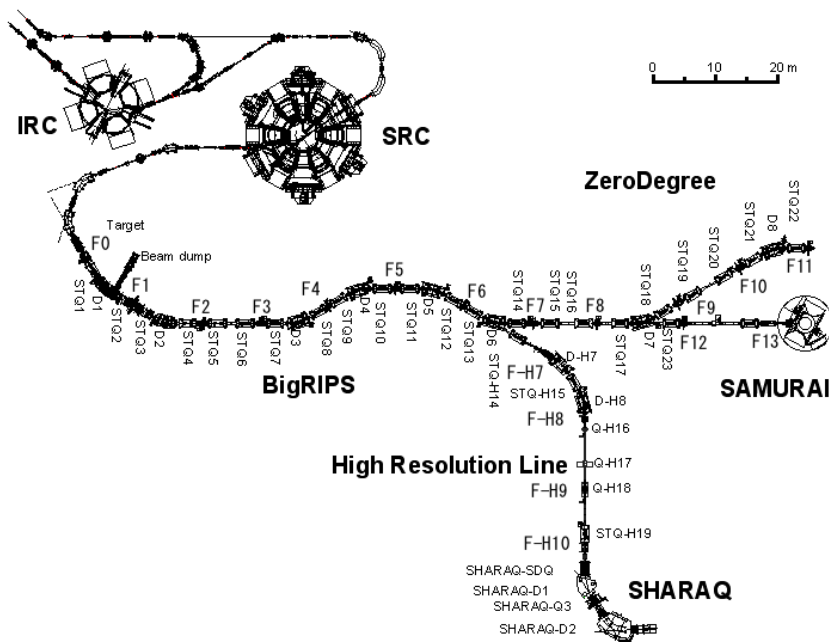


Fig. 4.2 – Scheme of the RIBF experimental beam line.

The ^{238}U primary beam impinges on a 3-mm thick ^9Be primary target at the object point F0 of the BigRIPS separator with a mean intensity of 12 pnA. It fragments into a cocktail beam that is selected by use of Aluminum wedges [115] at the F1 and F5 dispersive planes in BigRIPS up to the secondary LH_2 MINOS target and the SEASTAR setup at F8. The BigRIPS spectrometer is a two-stage separator: the first stage from F0 to F2 is used for separation of the nuclei of interest through a $B\rho\text{-}\Delta E\text{-}B\rho$ selection and the second stage for identification of the beam with a $B\rho\text{-}\Delta E\text{-}TOF$ method. Characteristics of the BigRIPS line are shown in Tab. 4.1.

Selection. The nucleus of interest is selected in the first part of the spectrometer (F0-F2) with a momentum achromatic magnetic separator. It is composed of 2 dipoles of 30° angle of curvature (D1 and D2) separated by an aluminum degrader at the F1 dispersive focal plane and four superconducting quadrupoles to ensure beam focusing. The nuclei are scattered in moment by the first dipole D1 on the the dispersive focal plane F1 and the dipole D2 after is tuned to transmit the nuclei of interest to the non-dispersive focal plane F2 while removing the other nuclei with slits at F1. The trajectory of an ion in a constant magnetic field B depends

	BigRIPS	ZeroDegree
Angular acceptance (mrad)	(H) 80 (V) 100	(H) 90 (V) 60
Momentum acceptance (%)	6	6
Maximum $B\rho$ (T.m)	(F0-F2) 9.5 (F3-F7) 8.8	(F8-F11) 8.1
Momentum dispersion (mm/%)	(F0-F2) -21.4 (F3-F7) 31.7	(F8-F9) -24.8
Momentum resolution ($\Delta X = 1$ mm)	(F0-F2) 1260 (F3-F7) 3420	(F8-F11) 1240
Length (m)	78.2	36.5

Tab. 4.1 – Characteristics of the BigRIPS line.

on its mass A , its charge $Q = Ze$ (the nuclei are totally charge stripped, as can be checked afterwards with the absence of charge states in the particle identification plots, cf. Section 5.1), and its momentum p . It is described by the equation

$$B\rho = \frac{p}{Q} = \frac{\gamma m v}{Q} = \gamma \beta \frac{A c u}{Z e} \quad (4.1)$$

where ρ is the radius of curvature, $u \approx 931.5$ MeV the atomic mass unit, c the speed of light, $\beta = v/c$ and $\gamma = (1 - \beta^2)^{-1/2}$. As the secondary beam nuclei are produced by fragmentation at F0, the velocity is constant. The selection in $B\rho$ with the first dipole D1 is then equivalent to a selection in A/Z . A beam dump is installed in the opening of the dipole to stop the fragments away from the central trajectory, corresponding to nuclei with an A/Q very different from the nuclei of interest. The selected nuclei are then transported up to the F1 dispersive focal plane with the achromatic wedge-shaped degrader whose thickness varies with the horizontal plane position. The energy and momentum lost by a nucleus (A, Z) in the degrader material are given by

$$\Delta E \propto \frac{AZ^2}{E} \propto \left(\frac{Z}{v}\right)^2 \quad \text{and} \quad \Delta p \propto \frac{Z}{v} \quad (4.2)$$

Considering a small velocity loss i.e. a constant velocity, the energy or momentum loss depends only on the charge Z of the fragments. The constant magnetic field of the dipole D2 is chosen to center the nuclei of interest and disperse the nuclei with a different charge Z , slits in the F2 focal plane stopping them. The momentum achromatic separator therefore allows to select nuclei with A/Z and Z separations.

Identification. The event-by-event identification of the resulting secondary cocktail beam is performed in the second part of the BigRIPS line (F3-F7). This achromatic part is composed of eight superconducting quadrupoles and four dipoles with a 30° angle of curvature (D3-D6), with the F4,F5,F6 momentum dispersive planes and a second degrader in F5 to improve the

separation of the secondary beam. The nuclei of interest are conducted up to the doubly-achromatic F7 focal plane, *i.e.* to a beam focused in both the horizontal and vertical planes, just before the SEASTAR experimental setup at the F8 focal plane with the secondary target. At each focal plane, detectors measure the time of flight, position (x, y), and energy loss of the nuclei with plastic scintillators, double Parallel Plate Avalanche Counters (PPAC) [116, 117], and MULTI-Sampling Ionization Chambers (MUSIC) respectively. For the BigRIPS identification part, there are two double PPACs at F3, F5, and F7, two plastic scintillators at F3 and F7, and a MUSIC detector at F7 for energy loss. The identification method is explained in detail in Section 5.1.

After the secondary reaction at F8, the beam residues are separated in the ZeroDegree spectrometer up to the F11 focal plane where the EURICA Ge array is taking data in parallel for isomer tagging. The cocktail beam after the secondary target at F8 is also identified event-by-event in the ZeroDegree beam line (F8-F11). To this end, double PPACs are placed at F8 and F11 for beam position, two plastic scintillators at F8 and F11 for time of flight, and a MUSIC detector at F11 for energy loss.

Three different beam settings were tuned for ^{67}Mn , $^{71,73}\text{Co}$ and ^{79}Cu . The incident energies at the entrance (exit) of the secondary target were ≈ 260 (≈ 200) MeV/nucleon for ^{67}Mn , $^{71,73}\text{Co}$ and ^{79}Cu . All the characteristics of the beam line for the three settings are summarized in Tab. 4.2.

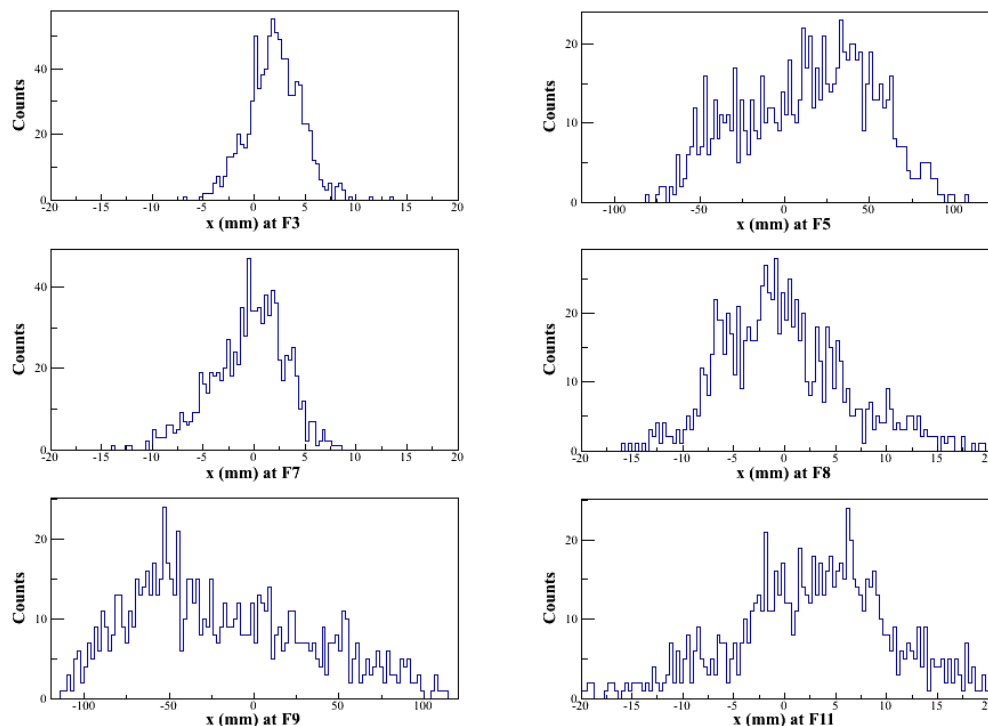


Fig. 4.3 – PPAC horizontal positions in the F3, F7, F8, F11 achromatic and F5, F9 dispersive focal planes for the $^{67}\text{Mn}(p, 2p)^{66}\text{Cr}$ reaction channel.

Primary beam	^{238}U
Primary beam intensity	12 pA
Be production target	3 mm
F1 Al degrader	8 mm
F5 Al degrader	2 mm

Setting	^{67}Mn	$^{71}\text{Co} / ^{73}\text{Co}$	^{79}Cu
$B\rho_{01}$ (D1) (T.m)	7.7490	7.7770	7.8920
$B\rho_{12}$ (D2) (T.m)	7.0260	6.9802	7.0362
$B\rho_{23}$ (T.m)	6.9994	6.9802	7.0362
$B\rho_{34}=B\rho_{45}$ (D3/D4) (T.m)	7.0162	6.9625	7.0543
$B\rho_{56}=B\rho_{67}$ (D5/D6) (T.m)	6.8002	6.7306	6.7992
$B\rho_{89}$ (D7) (T.m)	5.8300	5.6168	5.6020
$B\rho_{910}=B\rho_{1011}$ (D8) (T.m)	5.8230	5.5960	5.5914
F1 slits (mm)	± 64.2	L 42 / R 64.2	L 40 / R 64.2
F2 slits (mm)	± 4	± 4	± 4
F5 slits (mm)	± 120	L 120 / R 60	L 120 / R 65
F7 slits (mm)	± 70	± 30	± 60
Total rate at F8	~ 6 kpps	~ 5 kpps	~ 5.5 kpps
DALI2 Singles	~ 17 kcps	~ 15 kcps	~ 35 kcps
Nucleus of Interest	^{66}Cr	$^{70}\text{Fe} / ^{72}\text{Fe}$	^{78}Ni
Secondary beam intensity (purity)	12 pps (%)	45 / 6 pps (/ %)	5 pps (%)
Run duration	22.5 h	24.5 h	~ 5 d
Run numbers	38-69	107-145	208-355

Tab. 4.2 – BigRIPS and ZeroDegree settings with measured intensities.

The particle identification of the incoming (outgoing) cocktail beam is achieved by the Time Of Flight- $B\rho$ - ΔE method in the BigRIPS (ZeroDegree) spectrometer. Fully-stripped secondary ions are identified event-by-event. The particle identification of the incoming cocktail beam at the entrance of the secondary target and the identification of secondary residues are performed from $B\rho$, time of flight and ionization-chamber energy loss measurements in the BigRIPS and ZeroDegree (ZDS) spectrometers, respectively. The identification method of the nuclei will be described in Section 5.1. The horizontal positions in each focal plane given from the PPACs are presented in Fig. 4.3 for the $^{67}\text{Mn}(p, 2p)^{66}\text{Cr}$ reaction channel.

4.2 DALI2



Fig. 4.4 – Picture of the DALI2 gamma array. (Left) Half of the DALI2 crystals, seen from downstream, with the first layer crystals clearly visible. (Right) DALI2 crystals geometry shown from upstream. The last 11th layer of crystals is shown in the background.

The DALI2 gamma array [93] is composed of 186 NaI(Tl) scintillators from three different manufacturers: 66 detectors from St Gobain, 89 detectors from Scionix, and 31 detectors from Bicorn. The standard configuration of DALI2 is changed in the first layers for the SEASTAR experiment with 11 layers covering angles from 7° to 115° with the edges of the crystals. A picture of the DALI2 array is shown in Fig. 4.4. From the first to the tenth layer composed of 6 to 14 crystals of $40 \times 80 \times 160 \text{ mm}^3$ or $45 \times 80 \times 160 \text{ mm}^3$, two neighboring layers are attached to the same 5-mm thick Aluminum plate fixed on the support structure. The last layer in the forward angles is composed of 64 crystals measuring $60 \times 60 \times 120 \text{ mm}^3$. The SEASTAR layout is presented in Fig.4.5 (a), (b), and (c) for the layers 1/2, 3-10, and 11, respectively.

The DALI2 SEASTAR configuration is simulated with GEANT4 and energy resolution and photo-peak efficiency are shown in Fig. 4.6 with Doppler-shift corrections and addback (maximum distance between γ of 15 cm without energy threshold) using a target length of 100 mm and a vertex reconstruction resolution of 5 mm, consistent with the MINOS TPC tracking algorithm. The simulated energy resolution at 500 keV (1 MeV) is about 13% (11%) for $\beta = 0.6$ with a photo-peak efficiency of 42% (29%), respectively.

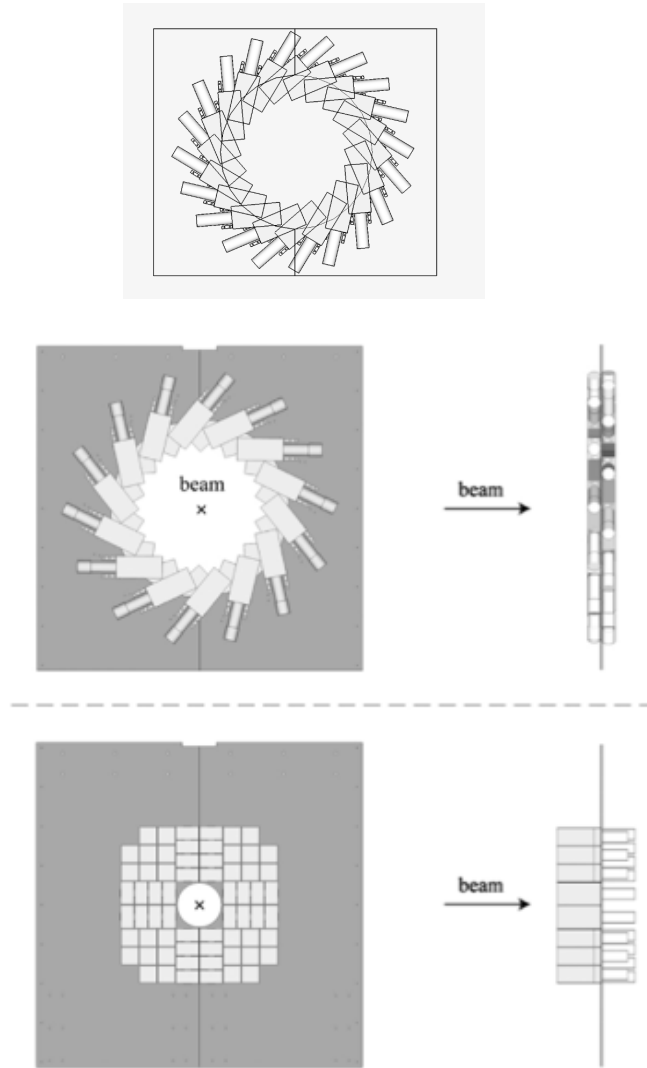


Fig. 4.5 – (Top) Layout of the new DALI2 layer of crystals for the SEASTAR experiments. (Middle) Layout of the detectors in the second to eleventh layers in the standard configuration. (Bottom) Layout of the last layer in the standard configuration.

During the experiment, the voltages of the DALI2 detectors are set between -1600 V and -1000 V to adjust the detectors in gain. For this, a ^{137}Cs source and its transition at 661.67 keV are used and the peak signal is read after amplification with an oscilloscope. The amplitude of the signal is looked at to obtain a range of about 8 MeV for all the detectors: the ADC modules have a voltage range of 8 V, therefore we adjust an amplitude around 600-700 mV. Once this rough calibration is done, an energy threshold is put in the Constant Fraction Discriminators (CFD) CAEN V812 at a constant voltage value from the fast signals of the DALI2 photomultiplier (PMT) signals, proportional to the energy signals from the PMTs going to the ADC modules. The threshold is applied through trial and error using the calibration source runs and around 70 mV is applied as a threshold which corresponds to a 200 keV energy threshold

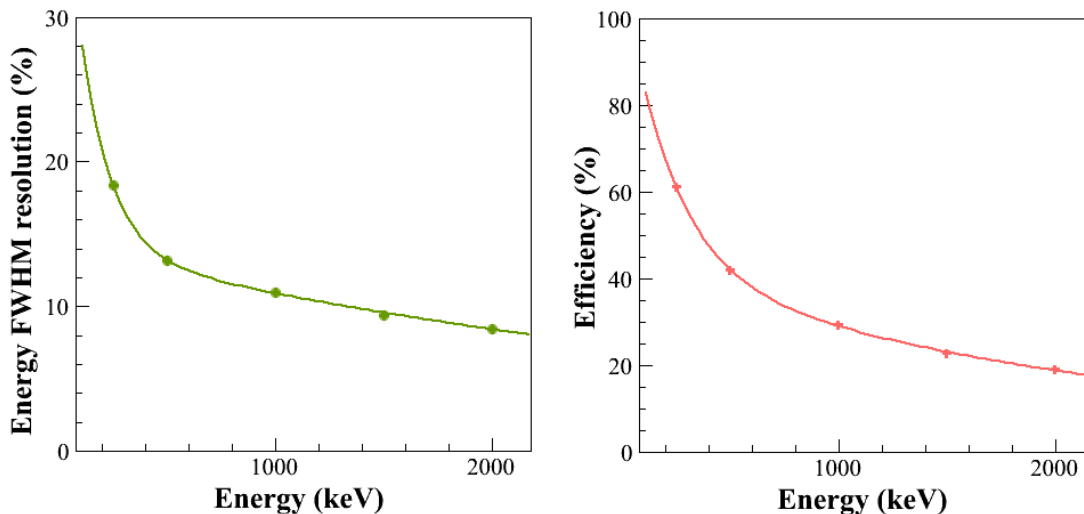


Fig. 4.6 – DALI2 GEANT4 simulated resolution (green) and photo-peak efficiency (red) at $\beta=0.6$ for the first SEASTAR campaign: target of 100 mm length and 5 mm vertex reconstruction resolution with Doppler-shift corrections and addback for hit detectors distant by less than 15 cm.

with a calibration source. With the Lorentz boost during the experiment, the γ -rays seen in the DALI2 detectors will be higher in energy with the Doppler effect at higher photon angles with respect to the beam direction. Therefore, the energy threshold is, at maximum, of 200 keV during the experiment.

4.3 MINOS configuration

The experimental setup at F8 is shown in Fig. 4.7 with the relative positions of the PPACs, DALI2, MINOS, and DSSSD. The MINOS structure is composed of two parts to fit inside the DALI2 structure: the lower support is inserted below the DALI2 one and placed at the F8 experimental area. The upper support of the MINOS structure with the beam pipe, cryostat and electronics is lifted up by a crane and inserted in DALI2 by opening the DALI2 structure in half layers in the beam area. The upper support is then connected to the lower part of the MINOS structure. The MINOS and DALI2 structures are then aligned with a laser from downstream in the beam direction and from the side of the setup in the vertical direction.

During the SEASTAR campaign, the liquid hydrogen target was 100(1) mm thick with an overall curvature of the Mylar windows of 2.7 mm, shown in more details in Section 5.5, Fig. 5.16.

The MINOS TPC is equipped with the Micromegas detector in the projective pad geometry (cf. Section 2.1.2) and read out for the first time in experiment with the new AGET chips in the FEC cards and the Feminos cards described in Section 2.1.4. Premix bottles of the MINOS TPC gas mixture are used for the gas flushing of the TPC, at usual flows of 8 to 10 liters per hour, to keep water (oxygen) impurities below 1200 ppm (50 ppm). The TPC mesh voltage is

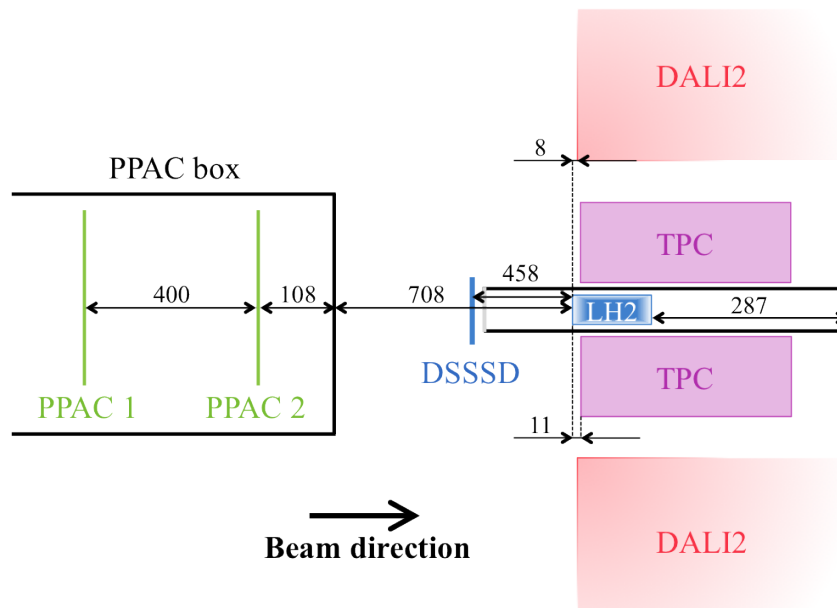


Fig. 4.7 – SEASTAR experimental scheme at F8 representing the distances between the F8 double PPACs, DALI2, MINOS and DSSSD in mm. The DALI2 structure start represented here corresponds to the edge of the first layer of detectors.

set between 450 and 470 V depending on the beam intensity of the setting (for the Cr setting, the voltage was put at 470 V) for a resulting gain between 6000 and 13000. The high voltage of the cathode is fixed at 6 kV so as to keep the TPC data taking window under $10 \mu\text{m}$, leading to a drift field of around 185 V/cm. The electronics are set in a gain range of 120 fC, the lowest one possible, as the low signals in the TPC permit it. We set the shaping time to 334 ns, the best compromise between loss of signal in the integration and long data processing time. A pedestal run such as shown in Fig. 4.8 is performed at the beginning of each run for the MINOS electronics to check the mean pedestal value and the noise levels of all the channels. The mean pedestal values are set at channel 250 before the experiment with a pedestal run performed without beam while during the run the pedestals are only checked.

Finally, the threshold of data saving for the pad signals are put to 5σ in order to discard the noise of the electronics and reduce the final amount of data and 8 (0) time bins are taken before (after) each signal's threshold to take the most of it for the analysis of the signals afterwards.

4.4 Trigger and data acquisition

During the SEASTAR experiment, the MINOS data acquisition (DAQ) system is enslaved to the RIBF DAQ [118] and is considered as a standard detector in the DAQ system, as in during the HIMAC experiment. Due to the great number of detectors in the experimental setup, a trigger logic is needed to optimize the data acquisition time. The two acquisitions are running with a common trigger. Therefore, during data processing and saving, the overall data acquisition system is blocked: it is called the dead time. The more the intensity of the cocktail beam, the

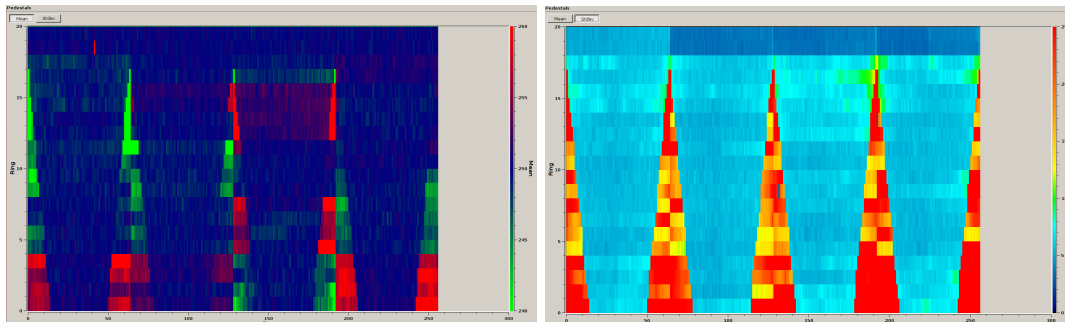


Fig. 4.8 – Result of a pedestal check performed at the beginning of a run for all the channels of the MINOS electronics. The ordinate corresponds to the ring of the TPC (the lower part is the inner ring of the TPC while the upper part corresponds to the outer ring of the TPC) and the abscissa to all the channels of each TPC ring. (Left) Mean pedestal value after equalization during the electronics configuration. (Right) Standard deviation σ , i.e. noise level, from the mean pedestal value. As this pedestal run is performed with the constant pad plane, there are less and less channels connected to an actual pad on the detector. These unconnected pads not connected to the ground are seen with a higher standard deviation value in orange or red.

more the dead time will be a liability.

The synchronization of the different detectors are made via the event number. The common trigger logic in the experiment is done with the GTO (General Trigger Operator), an FPGA (Field Programmable Gate Array) module created by H. Baba (RIKEN, Japan). It can accept in input up to 16 different signals to trigger the acquisition. The different triggers used during the SEASTAR experiment are the same as during a standard spectroscopy experiment: (i) the F7 Downscaled trigger corresponds to the incoming beam rate and is used for transmission and cross section measurements, it is downscaled by a factor 20 for the Cr setting due to the high overall beam intensity at F8, (ii) the F7 \times F11 and (iii) the F7 \times F11 $\times\gamma$ correspond to incoming beams transmitted in ZeroDegree with or without gamma detection. To obtain a common dead time, the GTO receives also as an input the End Of Busy signals from the different data processing parts of the setup and doesn't take any data before its receives all the End of Busy signals. For the beam line detectors and DALI2, VMI VME7807 and VMI VME7768 modules (VME CPU boards) are in charge of the data processing and can deliver the End Of Busy signal to the GTO. As for the MINOS system, its own acquisition provides an End Of Busy signal which can then be transmitted. The overall electronics scheme is presented in Appendix C.

LUPU (Logic Unit for Programmable Operation) modules are time stamp modules. The time information is stored according to input trigger and the LUPU module generates internal clocks for each detector while synchronizing an external clock for the overall system. In the case of the EURICA detector, taking data completely separately from the F8 area, this time stamp information is vital to merge the data afterwards.

Dead time. The slowest detector will determine the dead time of the entire setup. Let us estimate the MINOS dead time first. AGET chips in the electronics Front-End Cards are

read in parallel during an acquisition and contain 64 physical channels and 4 non instrumented channels, with 512 time bins used for the acquisition window. The AGET ADC has a $F_{ADC} = 25$ MHz conversion frequency which leads to a conversion time T for the MINOS electronics of $T = 512(N_{hitchannels} + N_{noisechannels})/F_{ADC}$ with $N_{hitchannels}$ the number of hit channels in the most hit ADC (i.e. with the most number of channels hit) and with $N_{noisechannels}$ the number of channels read out by the ADC but containing only noise (i.e. pseudo channels). As an illustration in the case of 2 pseudo channels, events with no real track inside the TPC should lead to a readout digitization time of $90\mu s$ and events with $N_{hitchannels} = 6$ maximum hit channels should lead to a readout time of $180\mu s$. In the SEASTAR experimental conditions of a 5 kHz incident beam and assuming 6 hit channels maximum, we expect a ZeroDegree trigger about 50% of the time compared to the incident beam intensity and a DALI2 trigger about 50% of the time with energy thresholds set to about 150 keV. We therefore expect a trigger rate of 1200 kHz. From GEANT4 simulations [41], reactions leading to charged particles through the TPC should represent less than 10% of the events. If we take 200 Hz real events in the TPC out of the 1200 Hz of trigger as a conservative value, we obtain a total acquisition occupancy for MINOS of 13%, which should lead to a dead time of the order of 20 %.

The dead time of DALI2 is of the order of $100\mu s$ with the current electronics and acquisition, while the beam detectors are the longer ones with $\sim 200\mu s$ dead time. During the experiment, a mean dead time around 10 % was found with a trigger rate of 500 Hz (for the Cr setting) and a mean maximum of 4 channels hit per AGET chip for MINOS. The measured values are consistent with our above estimates. The MINOS acquisition is not the limiting factor in the SEASTAR experiment, determined probably by the beam detectors, especially the ionization chambers due to a rather slow CAMAC electronics.

CHAPTER 5

Data analysis

From the raw data taken during the experiment, we need to reconstruct observables such as energy, time, or position through calibration. From there, we extract the quantities of interest: the Doppler corrected gamma energy spectrum of ^{66}Cr and the intrinsic momentum distribution of the knocked-out proton.

In a first step, the particle identification method for the incident nuclei in BigRIPS and for the emitted nuclei in ZeroDegree is used to distinguish the nuclei and reactions of interest. In a second step, the DALI2 gamma array is calibrated in energy with the calibration runs performed before and after each settings with several γ -ray sources at different energies. In a third step, we consider the MINOS TPC: the drift time needs to be determined over time as the TPC is not fully air tight to reconstruct the knocked-out proton trajectories in three dimensions and reconstruct the vertex position with the tracking algorithm. Once those calibrations are made, it is possible to obtain γ -ray spectra and to check the energy dependence over DALI2 detector angle and vertex position to place the MINOS structure with respect to the DALI2 structure in the beam direction. We then discuss the inclusion of the beam tracking with the PPAC from the beam line and the additional Si detector used for the first SEASTAR campaign. These beam trajectories enable to analyze events with only one proton detected in the TPC. In the last section, we discuss how to extract the total momentum distribution of the knocked-out proton from the incident nucleus.

5.1 Particle Identification

The particle identification of the incident nuclei in BigRIPS and of the emitted nuclei in ZeroDegree is performed event by event. It guarantees an unambiguous measurement from the plastic and PPAC detectors placed upstream and downstream the secondary hydrogen target. We select the beams with a $B\rho$ - ΔE - $B\rho$ method and use a $B\rho$ - ΔE -TOF method for identification which is described in the following.

5.1.1 $B\rho$ - ΔE -TOF identification method

$$B\rho = \frac{P}{Q} \Rightarrow \frac{A}{Q} = \frac{B\rho}{\beta\gamma} \frac{c}{m_u} \quad (5.1a)$$

$$\frac{dE}{dx} = \frac{4\pi e^4 Z^2}{m_e v^2} N z \left[\ln \frac{2m_e v^2}{I} - \ln(1 - \beta^2) - \beta^2 \right] \quad (5.1b)$$

$$TOF = \frac{L}{\beta c} \quad (5.1c)$$

The identification of the nuclei in the BigRIPS or ZeroDegree spectrometers for the incident or emitted beams respectively is done event by event with the determination of their charge Z and of their charge-to-mass ratio A/Q from the measurement of $B\rho$, ΔE , and Time-Of-Flight (TOF) using Eq. 5.1 as explained in Ref. [119]:

L corresponds to the flight path length, v ($\beta = v/c$, $\gamma = 1/\sqrt{1 - \beta^2}$ with c the velocity of light) is the velocity of the particle, $m_u = 931.494$ MeV is the atomic mass unit, and m_e (e) is the electron mass (elementary charge). z , N , and I represent the atomic number, the atomic density, and mean excitation potential of the material, respectively. Z , A and Q correspond to the atomic, mass and charge state number of the particle, respectively. The energy loss ΔE is described in Eq. 5.1b by the Bethe-Bloch formula [120, 121].

5.1.2 Identification in BigRIPS

$$TOF = \frac{L_{35}}{\beta_{35} c} + \frac{L_{57}}{\beta_{57} c} \quad (5.2a)$$

$$Z = \frac{\sqrt{m_e c^2 \beta_{35}^2}}{\sqrt{4\pi e^4 N z \left[\ln \frac{2m_e c^2}{I} - \ln \frac{\beta_{35}^2}{1 - \beta_{35}^2} - \beta_{35}^2 \right]}} \quad (5.2b)$$

$$\left(\frac{A}{Q} \right)_{35} = \frac{B\rho_{35}}{\beta_{35} \gamma_{35}} \frac{c}{m_u} \quad (5.2c)$$

$$\left(\frac{A}{Q} \right)_{57} = \frac{B\rho_{57}}{\beta_{57} \gamma_{57}} \frac{c}{m_u} \quad (5.2d)$$

We measure the TOF (cf. Eq. 5.1c) using thin plastic scintillation counters installed at F3 (F8) and F7 (F11) for BigRIPS (ZeroDegree), respectively (cf. Fig. 4.2 for the foci positions). These achromatic foci generate small beam spots and ensure a typical root mean squared time resolution of approximately 40 ps, which corresponds to a TOF resolution of 0.017% for a 300 MeV/nucleon particle.

To deduce the Z of fragments between F3 and F7, we use the energy loss measured using the Multi-Sampling Ionization Chamber (MUSIC) [122] at F7 which enables a resolution of about 0.5% σ in Z with the help of the Bethe-Bloch formula. In the BigRIPS spectrometer, we use the twofold $B\rho$ measurement deduced from Eq. 5.1 to obtain Eq. 5.2 for the TOF , Z , and A/Q values, with the subscripts 35 and 57 to identify the F3-F5 and F5-F7 sections of the BigRIPS spectrometer, respectively.

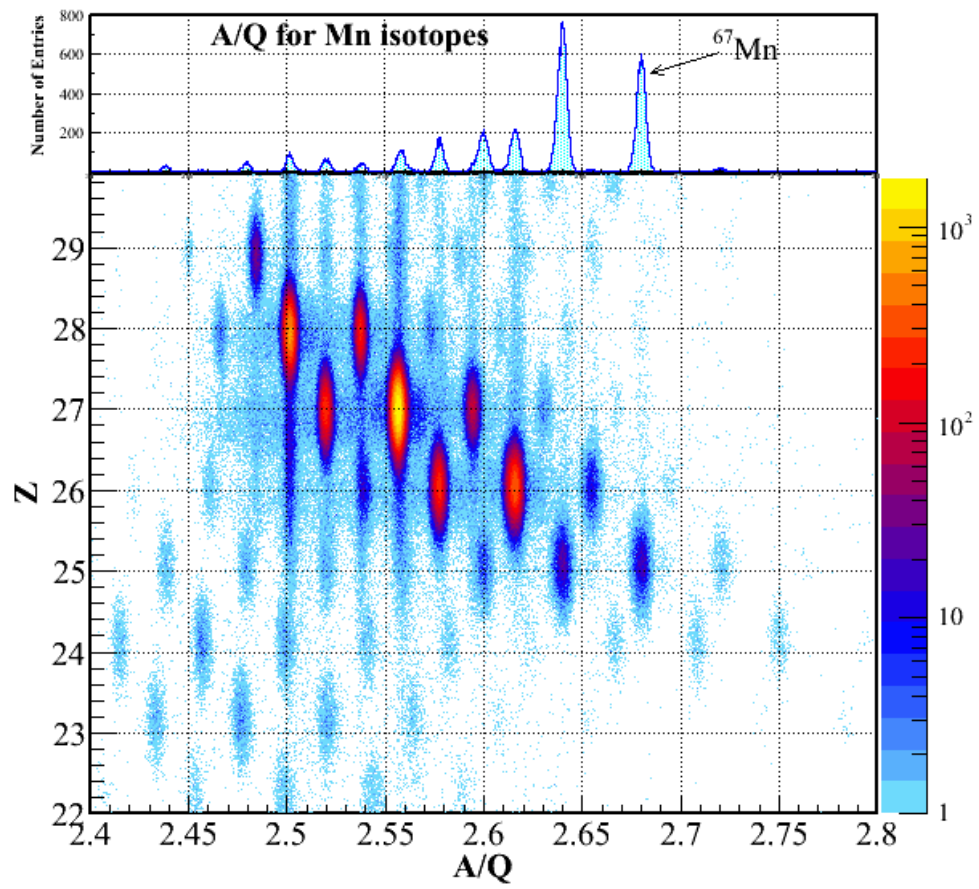


Fig. 5.1 – (Bottom) BigRIPS PID. (Top) Projection in A/Q for Mn isotopes, i.e. $Z=25$.

Trajectory reconstruction of the beam [123, 124, 125] in the two halves of the second stage in F3-F5 and F5-F7 via the positions and angles of the fragments with position-sensitive Parallel Plate Avalanche Counters (PPAC) [116, 117] at F3, F5, and F7 are used to measure the $B\rho$ (cf. Eq. 5.1a).

Assuming no charge change (i.e. no change in the A/Q value) in BigRIPS between the F3-F5 and F5-F7 sections, we then have $(A/Q)_{35} = (A/Q)_{57}$ and obtain Eq. 5.3 from Eq. 5.2:

$$\frac{\beta_{35}\gamma_{35}}{\beta_{57}\gamma_{57}} = \frac{B\rho_{35}}{B\rho_{57}} \quad (5.3)$$

The fragment velocities β_{35} and β_{57} before and after F5, respectively, can then be deduced from Eqs. 5.2a and 5.3 and are given in Eq. 5.4.

$$\begin{aligned} \beta_{35} &= \frac{(a_1 \times L_{35} + cL_{57} \times TOF)}{\left(a_1 c \times TOF + \left[1 - \left(\frac{B\rho_{57}}{B\rho_{35}} \right)^2 \right] \times L_{35} L_{57} \right)} \\ \beta_{57} &= \frac{(a_1 \times L_{35} + cL_{57} \times TOF)}{\left(c^2 \times TOF^2 + L_{35}^2 \left[\left(\frac{B\rho_{57}}{B\rho_{35}} \right)^2 - 1 \right] \right)} \\ a_1 &= \sqrt{c^2 TOF^2 \left(\frac{B\rho_{57}}{B\rho_{35}} \right)^2 + \left[\left(\frac{B\rho_{57}}{B\rho_{35}} \right)^4 - \left(\frac{B\rho_{57}}{B\rho_{35}} \right)^2 \right] L_{35}^2 + \left[1 - \left(\frac{B\rho_{57}}{B\rho_{35}} \right)^2 \right] L_{57}^2} \end{aligned} \quad (5.4)$$

Calibration parameters for the BigRIPS A/Q and Z identification are given by the BigRIPS team and automatically implemented so that no correction is necessary for the analysis. The resulting PID plot for the BigRIPS spectrometer is presented in Fig. 5.1. The residual events on the bottom left part of the figure and vertical lines in the identification are due to signal pileups in the plastic scintillators and in MUSIC, respectively.

For the BigRIPS spectrometer we obtain an A/Q root mean square resolution of 0.087% for the Manganese isotopes, compared to a nominal A/Q resolution of 0.038%. Since the resolution is sufficient for a clear separation of isotopes, we did not try to improve it further.

5.1.3 Corrections for the ZeroDegree identification

For the ZeroDegree spectrometer, we apply the same identification method on the F9-F11 area of the spectrometer, with the resulting PID shown in Fig. 5.2 in the top left figure. However further corrections are needed in order to obtain a sufficient A/Q resolution.

We use the method described in Ref. [119], and apply corrections for the region of ^{67}Mn and ^{66}Cr . We first look at the horizontal position X in F9, named F9X below, and plot it with respect to A/Q in the bottom left part of Fig. 5.2. For the region of interest at $A/Q=2.68$ for ^{67}Mn , there is a F9X dependence for A/Q . We linearly correct this A/Q with: $(A/Q)_{new} = A/Q + 0.00005 \times (F9X - 100)$. The same procedure is then applied in the F9 and F11 focal plane on the horizontal direction and angle up to third order and a first order correction on the charge of the F8 plastic detector. The final identification plot obtained in ZeroDegree is shown

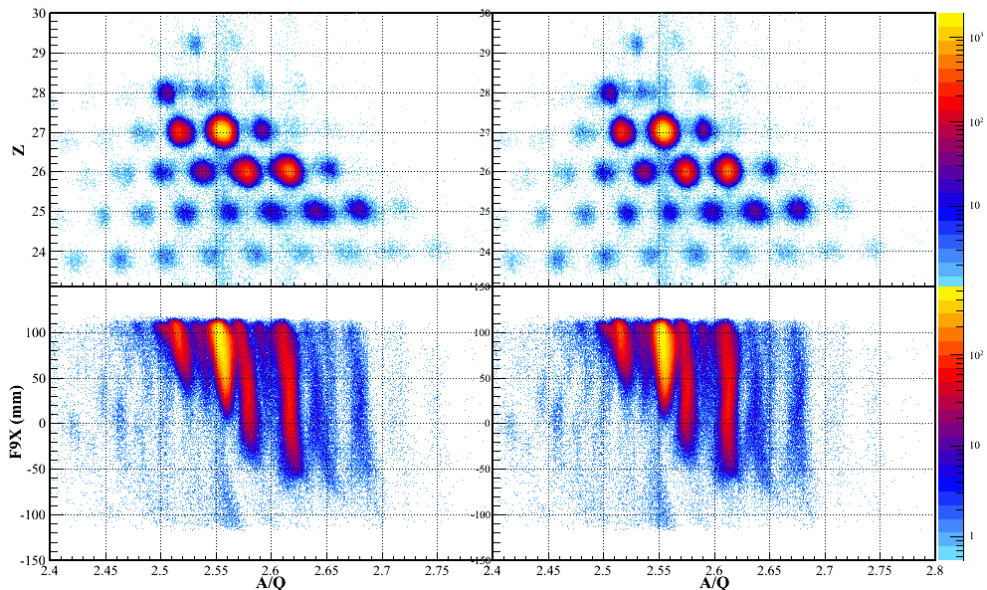


Fig. 5.2 – (Left) ZeroDegree particle Identification plot on the top figure and F9X position with respect to A/Q on the lower figure before any corrections. (Right) ZeroDegree particle Identification plot on the top figure and F9X position with respect to A/Q on the lower figure after a linear correction in F9X.

in Fig. 5.3. From LISE predictions [126], the 24^+ charge states correspond to about 0.1% of ^{66}Cr and therefore do not need to separate the different charge states in the ionization chamber.

We obtain a root mean square A/Q resolution of 0.17% for ^{66}Cr for a nominal A/Q resolution of 0.084% for the ZeroDegree spectrometer. From this particle identification, we can then apply cuts on the nuclei of interest to select a reaction channel. In BigRIPS we will select the incident ^{67}Mn and select the $(p, 2p)$ residue ^{66}Cr in ZeroDegree.

5.1.4 Efficiency and beam line transmission

Efficiency. We take the physics runs with a cut on ^{67}Mn in BigRIPS to calculate the ZeroDegree PPAC efficiencies (relative to BigRIPS) for this nucleus. For this, we look at the ZeroDegree line if a signal has been found in the ZeroDegree ionization chamber (MUSIC). By counting this, we take into account also the transmission of the beam in ZeroDegree. Therefore, the PPACs in the ZeroDegree line will have a decreasing number of counts with the next focal plane. However, we can still monitor relative PPAC efficiencies in a focal plane. We obtain the overall efficiencies shown in Tab. 5.1. All of the PPACs have 90 % efficiency or more, except for the PPACs at F11 with 70-80 %.

The beam tracking can be performed with one of the PPAC planes in a focal plane, which enables an even higher overall efficiency of the line of more than 90 %.

Transmission The most important energy loss in the beam line occurs in the hydrogen target. The transmission of the beam line therefore depends a lot on the transmission or absorption in the hydrogen target. To determine an overall efficiency taking into account this

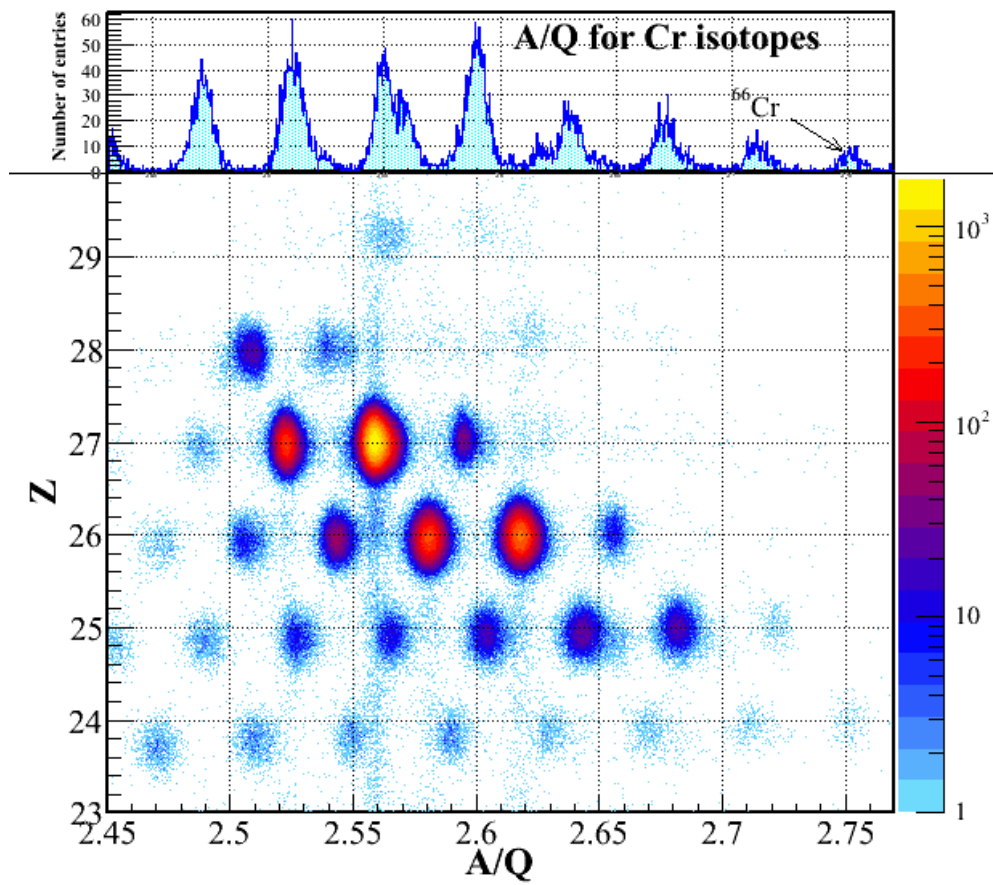


Fig. 5.3 – (Bottom) ZeroDegree PID after corrections. (Top) Projection in A/Q for Cr isotopes, i.e. $Z=24$.

	Nuclei (number)	Nuclei (%)
Total	121074	100 %
PPAC8 1A	117559	97 %
PPAC8 1B	116163	96 %
PPAC8 2A	114475	95 %
PPAC8 2B	111893	92 %
PPAC9 1A	111513	92 %
PPAC9 1B	107817	89 %
PPAC9 2A	108166	89 %
PPAC9 2B	110037	91 %
PPAC11 1A	105984	88 %
PPAC11 1B	100922	83 %
PPAC11 2A	97329	80 %
PPAC11 2B	90333	75 %

Tab. 5.1 – ZeroDegree PPAC efficiencies convoluted with the transmission of the cocktail beam in the ZeroDegree line.

probability of re-interaction in the target, we take a transmission run with ^{67}Mn centered in BigRIPS and ZeroDegree, with the hydrogen target filled. Looking at the F7 downscaled triggers, we count the number of ^{67}Mn transmitted in ZeroDegree with respect to the number of ^{67}Mn arriving through the BigRIPS line. Out of the 142 ^{67}Mn arriving at the F8 area, 87 of them are transmitted up to F11. This gives us a $T = 61(8)$ % overall transmission, including the efficiencies and acceptances of the beam line.

5.2 DALI2 Calibration

5.2.1 Energy calibration

Three different γ -ray sources are used for calibration: ^{88}Y , ^{137}Cs , and ^{60}Co . The ^{88}Y has two γ -ray transitions at 898.04 keV and 1836.06 keV, ^{137}Cs one transition at 661.66 keV, and ^{60}Co two transitions at 1173.24 keV and 1332.50 keV. The sources are placed at the side end of the MINOS beam pipe or on the beam pipe exit window, as the pipe is closed by Mylar windows on both ends to maintain the vacuum around the hydrogen target. Each calibration run was taken for at least half an hour to obtain enough statistics to distinguish the transitions from the noise.

For the spectroscopy of ^{66}Cr , the systematics suggest a first transition around 400 keV. As our lowest transition is situated at 661.66 keV with ^{137}Cs , an extrapolation is made of the linearity below this value. NaI scintillators are known to be not linear below 400 keV [127], therefore we check the variation of the calibrations at low energy with the ^{133}Ba source (γ -ray at 356 keV) calibration run performed during the second SEASTAR campaign and obtain an overall calibration error of 5 keV for all energies for the 186 scintillators of DALI2.

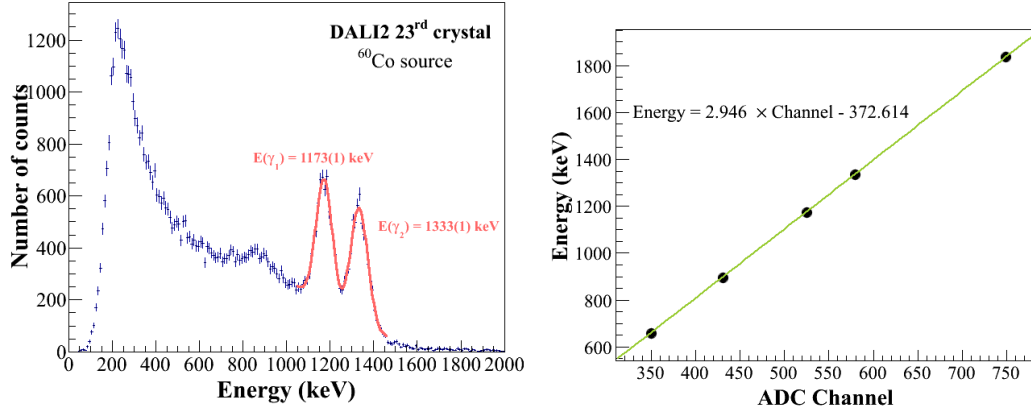


Fig. 5.4 – (Left) Energy spectrum of ^{60}Co after calibration for the 23rd DALI2 crystal, fitted with an exponential background summed with a double gaussian function. (Right) Linearity between the ADC channel and energy for the same detector.

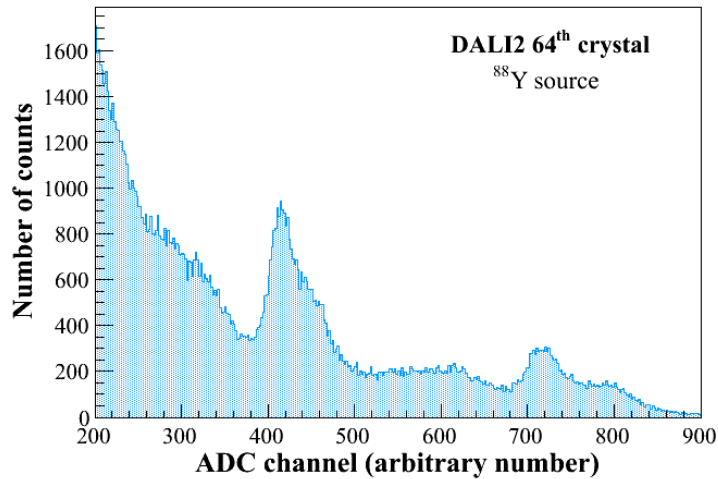
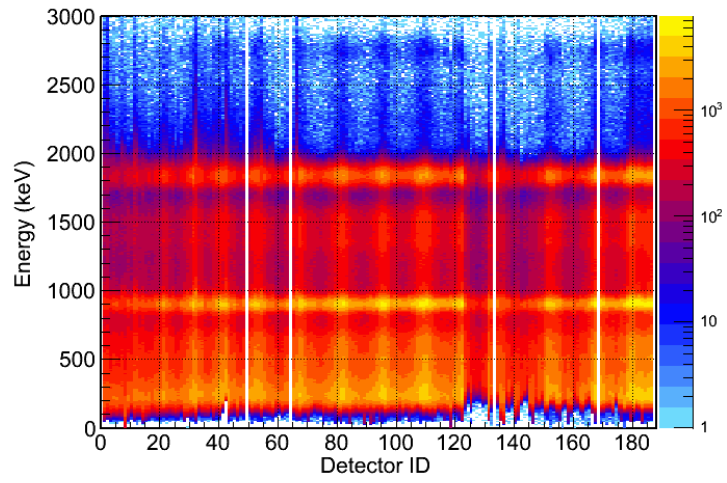
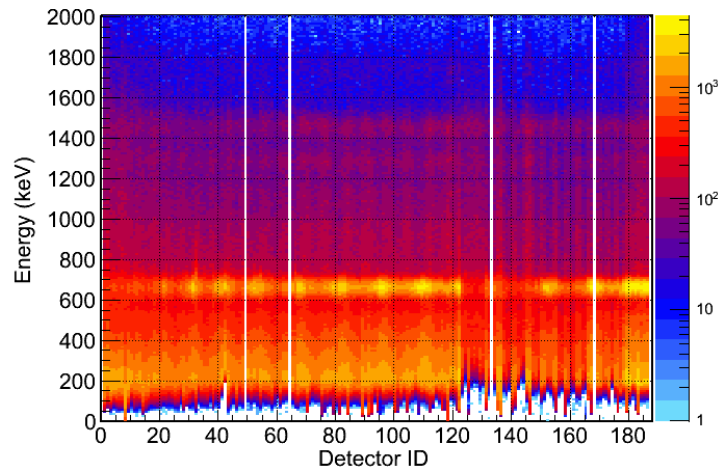


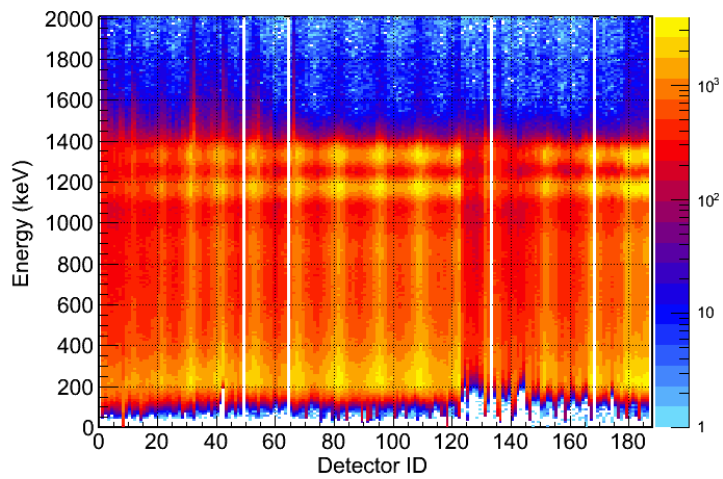
Fig. 5.5 – (Right) Raw spectrum (in ADC channels) of ^{88}Y for the 64th DALI2 detector. The two transitions are each divided in two bumps because of the non linearity.



(a) ^{88}Y source



(b) ^{137}Cs source



(c) ^{60}Co source

Fig. 5.6 – Energy spectra for the three calibration sources and the 186 DALI2 detectors.

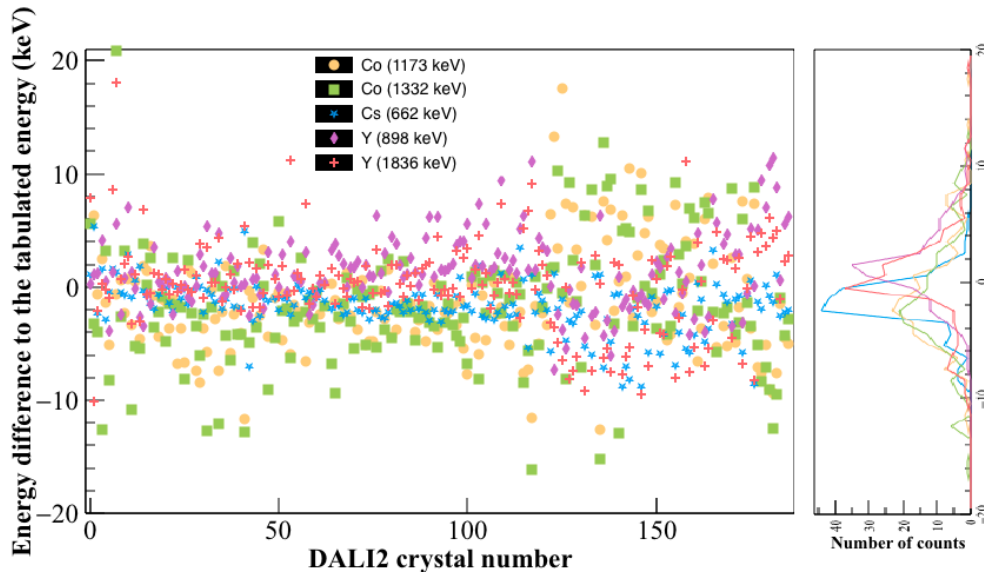


Fig. 5.7 – (Left) Energy difference between measured and tabulated energy transitions of the calibration sources for the 182 DALI2 crystals taken in the analysis. (Right) Projection of this energy difference for all the detectors.

The 186 DALI2 detectors have a similar energy range but a slightly different gain and need to be aligned in energy for the experiment. Each detector has an energy range up to around 8 MeV with 4096 channels in the ADC module. The raw ADC channel information is assumed proportional to the real energy in a NaI scintillator. Therefore, the five transitions in each crystal are fitted with a gaussian and exponential background to determine the linear function for energy calibration in keV. An example of ^{60}Co final fitted energy spectrum for one DALI2 crystal is shown on the left side of Fig. 5.4, as well as its fitted linearity between ADC channel and energy on the right side of Fig. 5.4.

As the scintillators are sensitive to the beam intensity and to the magnetic residual field of the downstream dipole, the crystal gain varies within the SEASTAR campaign with different settings. From a detailed analysis of crystal gain during the SEASTAR campaign performed by Ryo Taniuchi (PhD from the University of Tokyo in charge of the ^{78}Ni spectroscopy) it was determined that less than 1 % gain variation occurred for the DALI2 detectors at 1 MeV, which validates the use of a single calibration file through the whole Cr setting. When needed and useful, we applied a second order polynomial function for the correspondence from ADC channel to energy. We have also put out four detectors from the analysis: one of them never gave any signal (i.e. the detector was broken, ID 133) and the other three detectors (ID 49, 64, and 168) were very non linear as some of the transitions became divided (cf. Fig. 5.5 on the right for the 64th crystal). We obtained the calibrations shown in Fig. 5.6 for the different γ -ray sources.

For the five transitions in the calibrations, the difference between the measured and tabulated energies are plotted for all the detectors and shown in Fig. 5.7. The full-width half maximum (FWHM) resolutions of those peaks is also shown in Fig. 5.8.

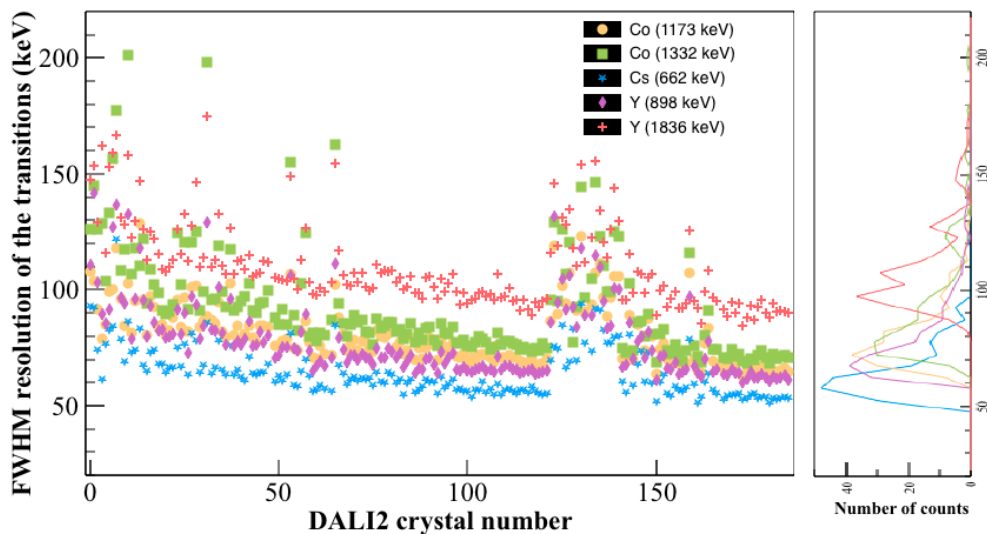


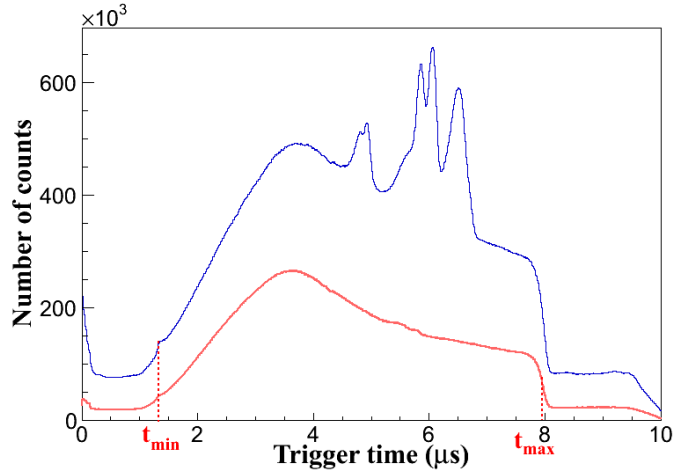
Fig. 5.8 – (Left) FWHM resolutions for the energy transitions of the calibration sources for the 182 DALI2 crystals taken in the analysis. (Right) Projection of this FWHM resolution for all the detectors.

5.2.2 Efficiency

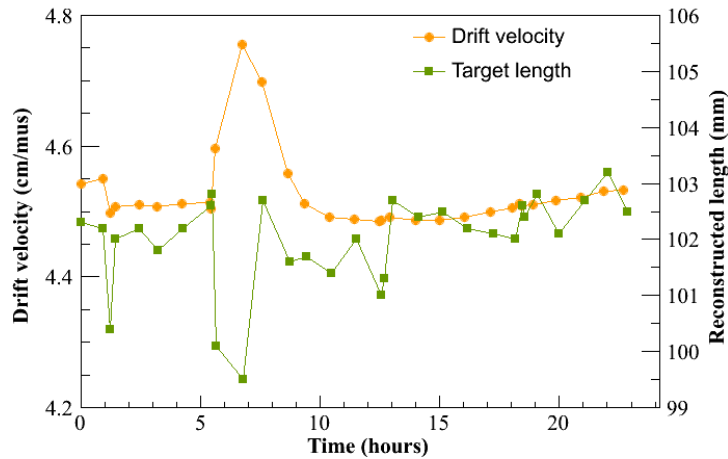
To determine the DALI2 efficiency, we rely on the GEANT4 simulations for the experiment and benchmark the simulations on a calibration run. Looking at the ^{137}Cs source, we can fit the transition at 661.66 keV with a gaussian and exponential background both for the calibration spectrum and for the GEANT4 simulation response by placing the source in the same position as in the calibrations and using the individual resolutions of the detectors. For the simulation, we fit with a sum of gaussian and exponential function and calculate the integral of this function in the region of the peak to determine the number of γ in the peak. Divided by the 100000 γ s simulated with GEANT4, we then obtain an efficiency of 25 % with a 661.66 keV source. For the calibration run, we also fit the transition in the same interval with the gaussian and exponential sum. However we need to calculate the number of γ -rays emitted $\gamma_{emitted}$ during the run of $t = 1585$ s duration using the activity $a(^{137}\text{Cs}) \approx 7485.3(142.2)$ Bq of the source during the run. The efficiency of DALI2 ϵ_{DALI2} is then given by:

$$\epsilon_{DALI2} = \frac{\gamma_{measured}}{\gamma_{emitted}} = \frac{\gamma_{detected} \times f_{DS}}{a(^{137}\text{Cs}) \times t \times \epsilon_{lifetime}} \quad (5.5)$$

with $\epsilon_{lifetime} \approx 48.9$ % of accepted triggers with respect to the real triggers from the source during the acquisition, $f_{DS} = 1$ the downscaling factor of the acquisition and $\gamma_{detected} \approx 1.326 \times 10^6$ the number of γ s in the integral of the fit. We finally obtain a measured DALI2 efficiency of $\epsilon_{DALI2} = 23(1)$ %. The measured and simulated efficiencies are comparable, and the small difference can be due to the indetermination in the position of the target of a few millimeters and to the indetermination in the efficiency fit.



(a) Time drift in μs inside the TPC during the ^{66}Cr setting. In blue are shown all the events for one run, whereas the red curve shows the events where less than 10 pads for each ring are hit.



(b) Deduced drift velocity (yellow) in $\text{cm}/\mu\text{s}$ and reconstructed target length (green) in mm over the ^{66}Cr setting

Fig. 5.9 – Time drift in the TPC for one run and drift velocity and target length over the ^{66}Cr setting.

5.3 MINOS Calibration

5.3.1 Drift velocity

In the TPC, the only uncertainty is the drift velocity in the gas as impurities in the TPC change over time (cf. Section 3.3.1). As defined in section 2.1.2.2, we use Eq. 2.2 and plot all of the trigger times t_{pad} measured by the TPC during a run, as shown in Fig. 5.9a. For the events with less than 10 pads per ring hit, we plot the trigger time (in red), thus getting rid of the sparks registered by the TPC and background events. Electrons which are ionized at the level of the Micromegas plane have a drift ~ 0 , while those ionized at the very end of the

TPC (cathode) should have a drift time corresponding to 300 mm of drift length. We therefore obtain a distribution of correlated trigger events with the lowest time drift t_{start} and longest time drift t_{stop} which reflect the length of the TPC with the Micromegas plane and the cathode plane respectively. On each side uncorrelated trigger events appear as a background constant in the acquisition window of the electronics.

The minimum trigger time t_{min} does not depend on the drift velocity as it corresponds to an electron ionization at the Micromegas mesh. It depends only on the electronics trigger from the RIBF DAQ and on the delay time first applied to the MINOS electronics. We can therefore determine this time for the overall SEASTAR campaign. As seen in Fig. 5.9a, there is not a sharp slope to indicate the start of the TPC (unlike the cathode plane of the TPC which corresponds to a rather sharp slope), and we rather use the end of the upward slope as t_{min} value at the kink seen between the start of the TPC and the increase of statistics moving in the direction of the beam because of the forward angle production of knocked-out protons. As for the end of the TPC with t_{max} , it directly reflects the drift velocity and has to be measured continuously. For each run, we then plot as in Fig. 5.9a the trigger times in the TPC and determine the mid-point in the downward slope which can be fitted as a Fermi function: $f(t) = p_0 / (\exp((t - p_1)/p_2) + 1) + p_3$.

The Micromegas plane of the TPC is chosen as the origin of the beam line axis. Therefore the drift velocity must be calculated to obtain a position distribution of the TPC length ($L_{TPC} = 300$ mm), starting $z_{min} = 0$ mm and stopping at $z_{max} = 300$ mm.

We can then determine the drift velocity for every run, as $v_{drift} = L_{TPC} / (t_{max} - t_{min})$. We can monitor in this way the drift velocity over time, as shown in Fig. 5.9b in yellow over the ^{66}Cr setting. The TPC is then calibrated, the tracking algorithm defined in Section 3.2 can be applied, and the reaction vertex can be reconstructed. One can look at the vertex reconstructed in the beam direction, as its distribution should reflect the target length. The liquid hydrogen target of around 102(1) mm thickness can be compared to the reconstructed target length and serves to double check our drift velocity measurement, as is shown in green in Fig. 5.9b. The peak in drift velocity after about 5 h of run results in a slight target difference of around 2 mm, well below the vertex resolution. It occurs after a gas bottle change, which can affect the levels of impurities and gas mixture percentages differences.

5.3.2 Inclusion of beam tracking: PPAC and DSSSD

With the geometrical efficiency of MINOS, some $(p, 2p)$ reactions can produce a proton at very forward angle not seen in the TPC. To be able to reconstruct the interaction vertex with only one proton, we need to reconstruct the beam trajectory in this case. We use the two PPACs at F8 before the target to measure the beam position and direction. However, when possible, we can use the Si detector (DSSSD) placed just in front of the MINOS structure and one of the PPACs to reconstruct the beam as the track reconstruction will be more accurate in this case as the DSSSD is placed much closer to the target [41].

Assuming that the z position of the PPACs and DSSSD is known (cf. Fig. 4.7), we then need to adjust the x and y relative positions to align the two PPAC planes and the DSSSD with the DALI2 and MINOS setup and have 6 variables to adjust. First, we take care of the PPAC position relative to the TPC. It is performed using a $(p, 2p)$ reaction channel with

$x_{offset}(PPAC1/2)$	- 2 mm
$y_{offset}(PPAC1/2)$	+ 1 mm
$y_{offset}(DSSSD)$	+ 5 mm
$y_{offset}(DSSSD)$	+ 3 mm

Tab. 5.2 – PPAC and DSSSD offsets applied for the first SEASTAR campaign.

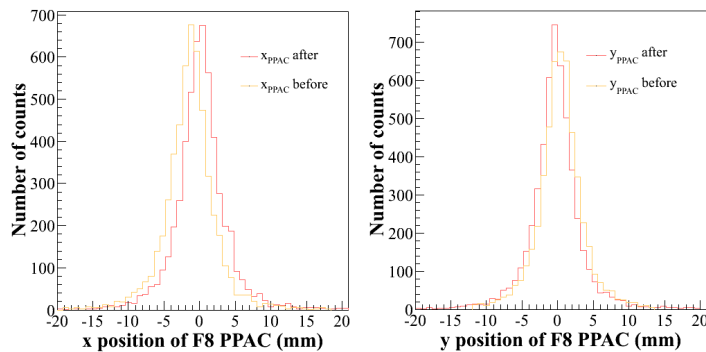


Fig. 5.10 – Differences in x (left) and y (right) reconstructed vertices from either the TPC for the two protons or one proton from the TPC and the beam from the PPAC trajectory. In orange is represented the two different distributions before corrections in position, and in red after corrections in position.

enough statistics ($^{69}\text{Co}(p, 2p)^{68}\text{Fe}$) and matching the vertex point distributions for a two-proton detection with the TPC or with one of the protons and the beam trajectory. We hence plot the difference from the two reconstructed vertices, as shown in Fig. 5.10 in x and y directions. The maximum of the distributions should be at the origin. The offsets in these distributions give us the offsets needed to be applied to position the PPACs. The position resolution of the PPAC detectors in the Cr region is given by Ref. [116] with a σ of about $600 \mu\text{m}$.

Once the shifts are correctly applied to the PPAC, we can position the DSSSD with respect to the PPACs by comparing the position of the beam by the DSSSD and the reconstruction of the beam position by the PPACs on the DSSSD plane. The offsets of the DSSSD are chosen to match the centroids of the DSSSD and the PPACs positions, shown in Fig. 5.11 with the 2D plots before any correction on the DSSSD position, using the same method as for the PPACs. The overall offsets used during the experiment are given in Tab. 5.2.

5.3.3 Doppler correction with MINOS

Once a reaction channel is chosen for the analysis and the MINOS TPC data has been analyzed to reconstruct the vertex of interaction, we can merge this vertex information with the DALI2 information to apply a Doppler correction to the γ -ray energies event-by-event. This is done for a test case with more statistics, $^{69}\text{Co}(p, 2p)^{68}\text{Fe}$, to check the intrinsic positions of DALI2 with respect to the MINOS TPC and hydrogen target.

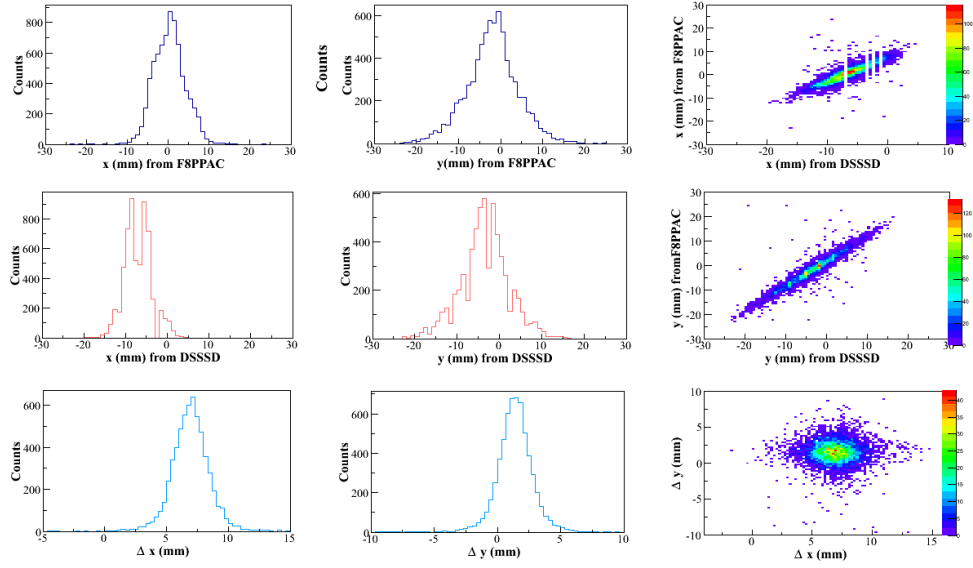


Fig. 5.11 – (Before any position correction on the DSSSD) x and y positions from the DSSSD and PPAC at F8 in the DSSSD plane along the beam on the four upper left figures. On the bottom part are the differences Δx and Δy between the DSSSD and PPAC reconstruction of the beam. On the right hand side are plotted 2D dimensional diagrams with the two different x and y beam tracking coordinates.

As the reaction nuclei travel at a relativistic energy, the γ -rays produced by its de-excitation are subject to a relativistic Doppler shift. The γ -ray energies measured by the DALI2 crystals will depend on the reaction vertex point (x_v, y_v, z_v) reconstructed by MINOS. If we take a γ -ray produced at an angle θ with respect to the beam direction with a beam velocity β_v at the vertex position, the Doppler corrected energy E_{Dopp} will be related to the uncorrected energy E_γ in the following way:

$$E_{Dopp} = \frac{1 - \beta_v \cos\theta}{\sqrt{1 - \beta_v^2}} E_\gamma \quad (5.6)$$

The angle θ is directly dependent on the reaction vertex and is calculated for each DALI2 detector at each event with the position of the hit scintillator and the vertex position on the beam axis z .

As Compton scattering of γ -rays is non negligible above 100 keV compared to photoelectric absorption as shown in example for NaI in Fig. 5.12 from Ref. [127], some crystals will only see a part of the γ -ray energy. It is then needed to add those energies to get back the initial energy: this procedure is called addback. This method needs to take into account the size and position of all the crystals to determine the nearest crystals. We use the mean interaction points of the crystals generated by the GEANT4 simulation of DALI2 and create a table for each crystal of all the crystals with a mean interaction point distant by less than our maximum distance for addback. This maximum distance for addback is taken from 15 to 25 cm in experiment, at 15 cm in our ^{66}Cr analysis, due to simulated average distance between two consecutive gamma

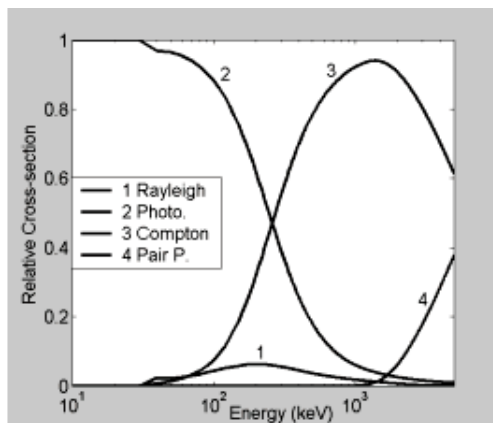


Fig. 5.12 – NaI(Tl) scintillator relative cross sections for photoelectric absorption (noted photo.), Rayleigh scattering, Compton scattering, and pair production (noted Pair P.) with respect to the γ ray energy.

interactions points and to the average distance between neighbouring crystal centers in the setup.

5.4 Reference measurement: ^{68}Fe

5.4.1 Dependence over angle and vertex

We take the case of a $^{69}\text{Co} (p, 2p) ^{68}\text{Fe}$ reaction to test our Doppler correction and see our dependence with respect to the angle of the detectors and to the vertex position along the beam. We can calibrate with different settings within the SEASTAR campaign the relative positions of the MINOS and DALI2 structures by minimizing the dependence of the γ -ray transition with respect to the position along the beam and to the angle of the detector hit. This work has been performed jointly with Corinne Louchart (TU Darmstadt) for the $^{70,72}\text{Fe}$ setting by varying the offset between the TPC and the γ array in a centimeter every 2 mm. For each of those choices of position offsets, we then vary independently the velocities before β_{before} and after β_{after} the target from the estimates obtained by LISE simulations with $\beta'_{before/after} = [\beta_{before/after} - 0.03, \beta_{before/after} + 0.03]$ with a 0.005 step. In each of these β combinations we reconstruct the Doppler corrected spectra for our test case and estimate the difference in the transition energy of the short-lived $4_1^+ \rightarrow 2_1^+$ between the beginning and end of the target. We also do the same to estimate the dependence between backward and forward angles of DALI2. We choose the short-lived $4_1^+ \rightarrow 2_1^+$ transition in ^{68}Fe to check this dependence as a lifetime of a few ten of ps will shift the reaction vertex and therefore false the Doppler correction, thus producing a shift in the energy peak. A position offset of $z_{offset}=7$ mm backwards was acknowledged for the SEASTAR campaign as the best compromise in energy and angle dependence with the joint analysis of the $2_1^+ \rightarrow 0_1^+$ ^{74}Ni transition from the $^{70,72}\text{Fe}$ setting.

The final optimization in position results in Fig. 5.13 for the dependence over angle with the energy plotted for each DALI2 detector.

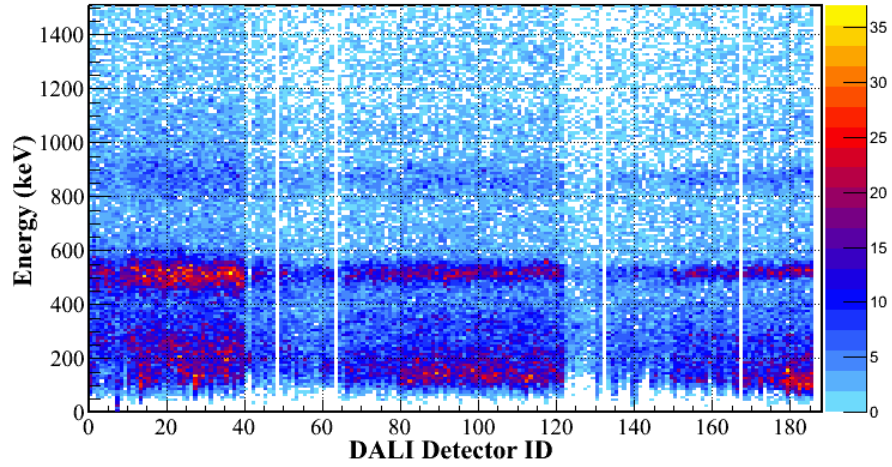


Fig. 5.13 – Doppler corrected energy for each of the DALI2 crystals.

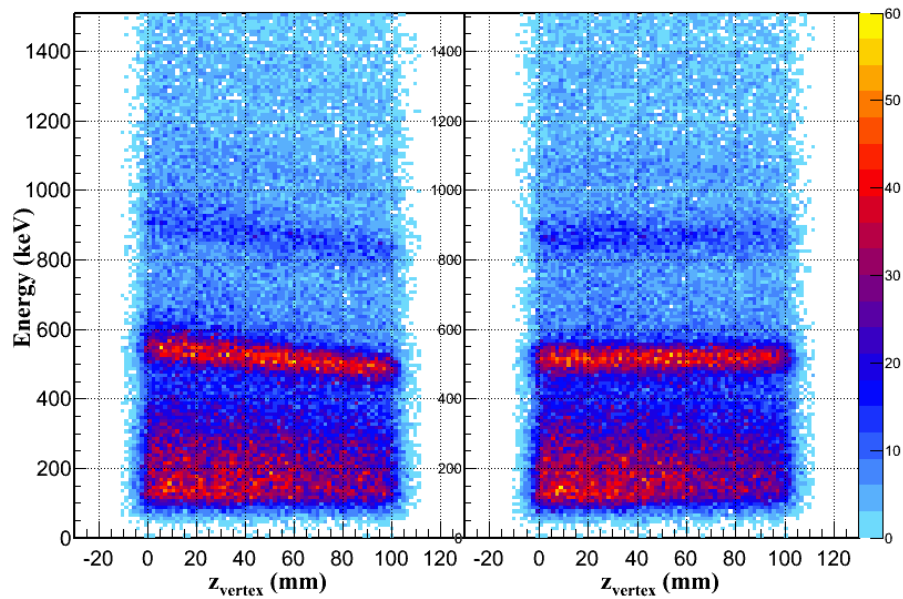


Fig. 5.14 – Doppler corrected energy with respect to the vertex position along the beam (Left) without MINOS reconstruction (Right) with MINOS reconstruction.

One can compare the dependence of γ -ray energy over the vertex position z_v along the beam, shown in Fig. 5.14. on the left figure. We plotted the Doppler corrected energy without taking into account the reconstructed vertex (i.e. taking a constant vertex position at the mid-target). We clearly see the dependence of energy over the target length and the resulting broadening of transitions. On the right, we can see the Doppler corrected energy with the reconstructed vertex taken and we correct the effect of the target thickness thanks to the tracking.

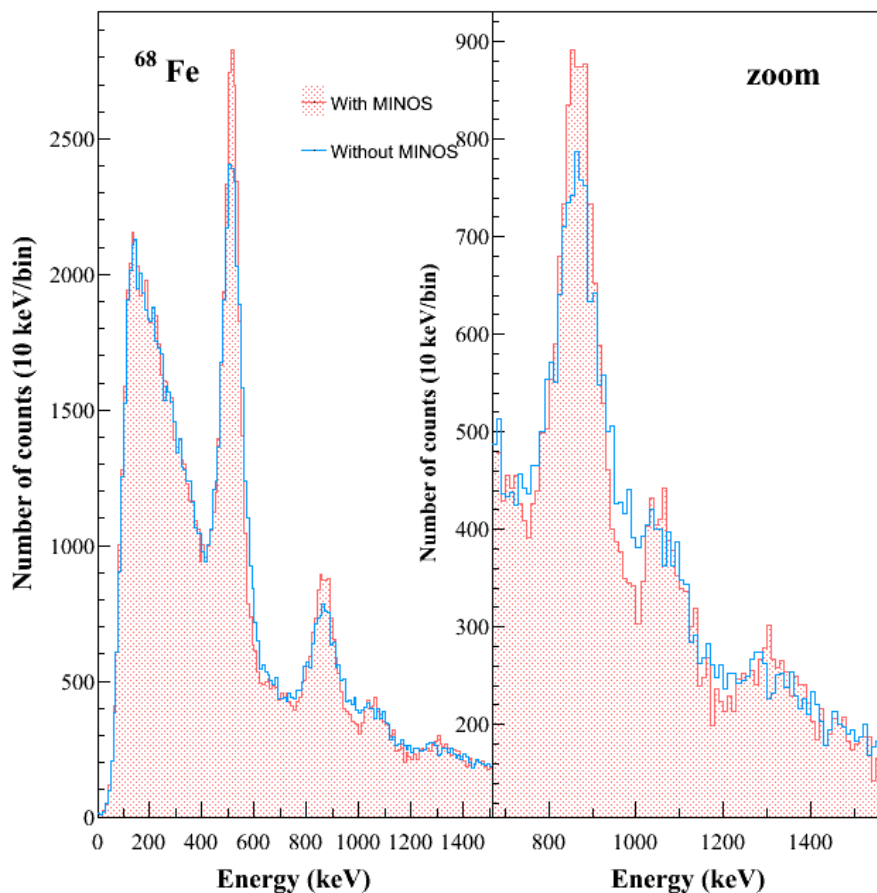


Fig. 5.15 – Doppler corrected energy spectrum of ^{68}Fe with addback and gamma multiplicities after addback below 4.

5.4.2 Energy spectrum of ^{68}Fe

^{68}Fe is a good reference measurement with two known transitions [128], assumed to be the $2_1^+ \rightarrow 0_1^+$ and $4_1^+ \rightarrow 2_1^+$ transitions from systematics and theory comparison. We can therefore compare the tabulated transitions at 522(1) keV and 867(1) keV to the measured transitions during this experiment, taking into account the lifetime of the states which will lower the peak position. The 4_1^+ state is short-lived compared to our sensibility. However, the 2_1^+ state has a lifetime of $\tau \approx 60(7)$ ps [74], which will result in about 10 mm travel in the target. This difference in position being higher than our vertex resolution with MINOS, we need to take the lifetime into account in the DALI2 simulations with GEANT4. In the case of a 386/480/520 keV transition, simulations yield an offset of 8/11/13 keV for a 50 ps half-life.

We obtain the spectrum of ^{68}Fe presented in Fig. 5.15, with the known two first transitions, measured at 515(8) keV and 867(3) keV respectively. Two new transitions are measured during this campaign, which are being analyzed in collaboration with L. X. Chung (VINATOM, Viet-



Fig. 5.16 – Scheme of the LH_2 target of 102.7(10) mm when cooled down and filled with hydrogen.

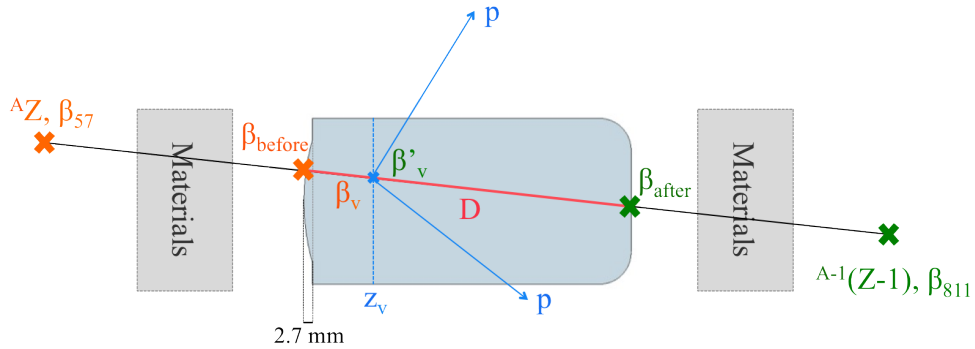


Fig. 5.17 – Scheme of the analysis in momentum distribution difference in a $(p, 2p)$ reaction.

nam). As a preliminary result, the four transitions appear all in coincidence with each other. Their cross section is being measured and the results will be compared to state-of-the art shell model calculations from F. Nowacki [67].

5.5 Momentum distribution of the knocked-out proton

To obtain the momentum of the knocked-out proton, the velocity at the reaction vertex needs to be implemented with higher accuracy than for gamma spectroscopy. For this, we measure the real travelled distance in the target as well as compute the velocity in the target using energy loss tables from the GEANT4 electromagnetic calculator [96].

As explained in Section 2.1.1, the entrance window of the LH_2 target is curved when the target is filled with hydrogen. In the effective 38 mm diameter entrance window, there is a maximum curve of 2.7 mm in the center for the first SEASTAR campaign at 1 bar internal pressure. The scheme of the hydrogen Mylar target is shown in Fig. 5.16. The exit window is also slightly curved in the corners but we have considered it flat to simplify.

We use the beam tracking by PPACs and DSSSD if available analyzed before to know the 3D position of the beam track in the target. To calculate the distance D travelled in the target, we create a disk which will be our entrance window and find the intersection of this disk with the

beam track in three dimensions (cf. Fig. 5.17). The resulting equation is a 2^{nd} degree equation and the physical solution will be chosen in the 2.7 mm in beam direction at the beginning of the target.

Knowing this travelled distance, it is now possible to calculate the velocity before β_v and after β'_v the reaction at the vertex position (x_v, y_v, Z_v) . Using the velocities measured inflight for every event β_{57} and β_{911} in the F5-F7 and F9-F11 areas respectively, we calculate the velocities at the reaction vertex position with the calculated travelled distance and with the energy losses tables by putting all the materials in the beam line.

In a $(p, 2p)$ knockout reaction, the momentum of the knocked-out proton is just the difference between the momentum of the incident nucleus and the momentum of the outgoing nucleus and is defined in Eq. 5.7.

$$\Delta P = \beta_v \gamma_v m_Z - \beta'_v \gamma'_v m_{Z-1} \quad (5.7)$$

To ensure that energy losses and beta extractions are correct, we first check the velocity matching for a direct beam at the target location, i.e. for unreacted and elastic events, from BigRIPS and ZeroDegree information. We have considered the high-intensity ^{69}Co beam as a test case.

Just before the target, the ^{69}Co beam has a mean velocity of $\beta_{beforeLH_2} \approx 0.64$, and a mean energy of 280 MeV/u, i.e. 53500 MeV/c. At the end of the target, the ^{69}Co beam has a mean velocity of $\beta_{afterLH_2} \approx 0.582$, and a mean energy of 215 MeV/u, i.e. 46950 MeV/c. The momentum distribution difference should be centered on zero and its FWHM corresponds to our momentum resolution.

The final plot obtained for the momentum resolution after taking the curvature of the target into account is shown in Fig. 5.18. We obtain a small offset in distribution of 1.3 MeV/u with a momentum resolution of 105 MeV/c in σ . We believe this small offset originates in incorrect energy loss estimate. The limiting factors to the momentum distribution are: *(i)* only total momentum distributions can be extracted and not parallel momentum distributions because of the lack of measurement of the angle of the beam after the target. *(ii)* Another important contribution to this resolution is the straggling of the beam in the target which induces errors in the estimations of the velocities before and after the target. *(iii)* Finally, the resolution of the reconstructed vertex with MINOS induces an error on the momentum distribution of the order of 12 MeV/c for ^{69}Co as an example.

We can then take the test case of $^{69}\text{Co}(p, 2p)^{68}\text{Fe}$, and consider the beam trajectory with the curvature of the entrance window and obtain the distribution difference on the lower side of Fig. 5.18. The width of the momentum distribution is now of 180 MeV/c to be compared to an intrinsic resolution of 105 MeV/c. We should also include in the measured momentum resolution the uncertainty caused by the vertex resolution ($\sigma(z_v) \approx 2.2$ mm). For ^{69}Co at 210 MeV/nucleon, a 2.2 mm travelled length produces 179 MeV/c loss, whereas for ^{68}Fe at 210 MeV/u, 2.2 mm in the target gives 167 MeV/c energy loss. This results in about 12 MeV/c uncertainty. The measured total momentum resolution is then of 180(12) MeV/c.

To calculate the contribution from the knocked-out proton in the momentum distribution, one needs to subtract this total momentum resolution with the intrinsic resolution obtained with the transmission measurement. The knocked-out proton then has a width of 75(12) MeV/c. Theoretical momentum distributions have been calculated by C. Bertulani (Texas A&M, USA) from his formalism published in Ref. [37]. Calculations for the studied $^{69}\text{Co}(p, 2p)^{68}\text{Fe}$ case

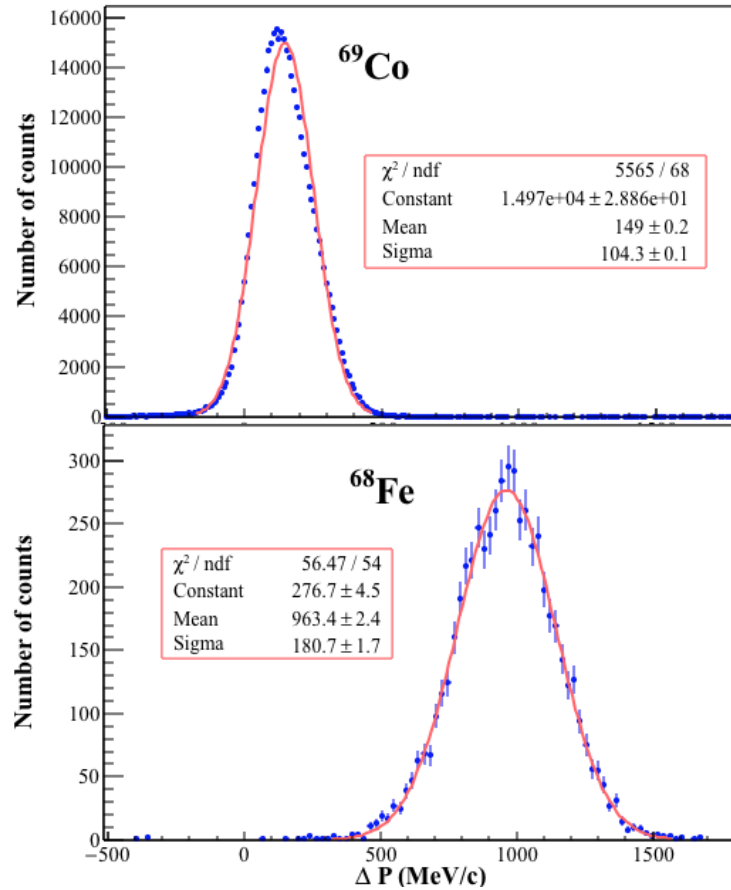


Fig. 5.18 – (Top) Direct ^{69}Co beam. Momentum difference distribution at the exit of the target between upstream (BigRIPS) and downstream (ZeroDegree). The distribution should be centered at zero and its width represents the intrinsic momentum resolution of the system. The target profile and beam trajectories are taken in consideration on an event-by-event basis. (Bottom) Momentum difference distribution inside the target by taking into account the vertex position with MINOS for the $^{69}\text{Co}(p, 2p)^{68}\text{Fe}$ case.

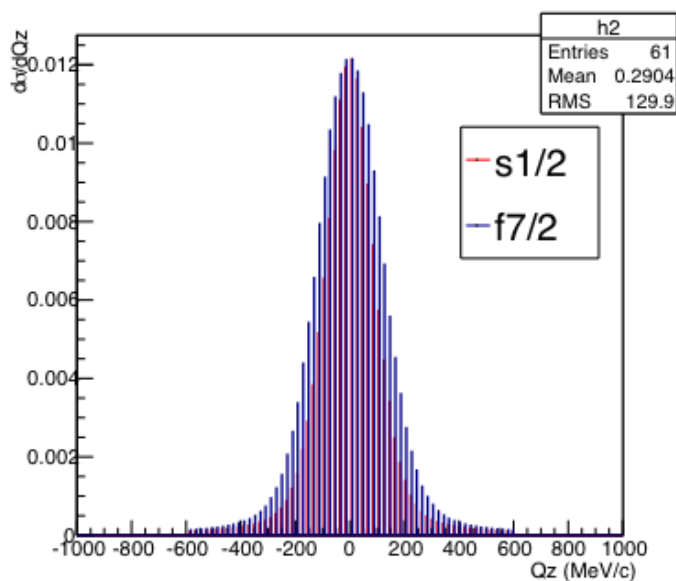


Fig. 5.19 – Momentum distributions for an $s_{1/2}$ and $f_{7/2}$ knocked-out proton in $^{69}\text{Co}(p, 2p)^{68}\text{Fe}$ from eikonal/DWIA calculations.

are shown in Fig. 5.19 for an $s_{1/2}$ and $f_{7/2}$ wave. As a first remark, the theoretical and experimental momentum distributions have comparable widths. However, the $s_{1/2}$ and $f_{7/2}$ waves have less than 50 MeV/c difference in width, which cannot be distinguished with the experimental momentum resolution for this reaction channel. The analysis of other reaction channels is ongoing to determine their momentum distributions and compare with calculations by C. Bertulani.

CHAPTER 6

Results and Interpretation

This chapter is dedicated to the experimental results and their interpretation. The energy spectrum of ^{66}Cr from in-beam spectroscopy, inclusive and exclusive cross sections are presented. The results are then interpreted by comparison to shell model calculations for the nuclear structure and within the eikonal formalism for the reaction part. The cross section analysis is very preliminary and still in progress.

6.1 Energy spectrum

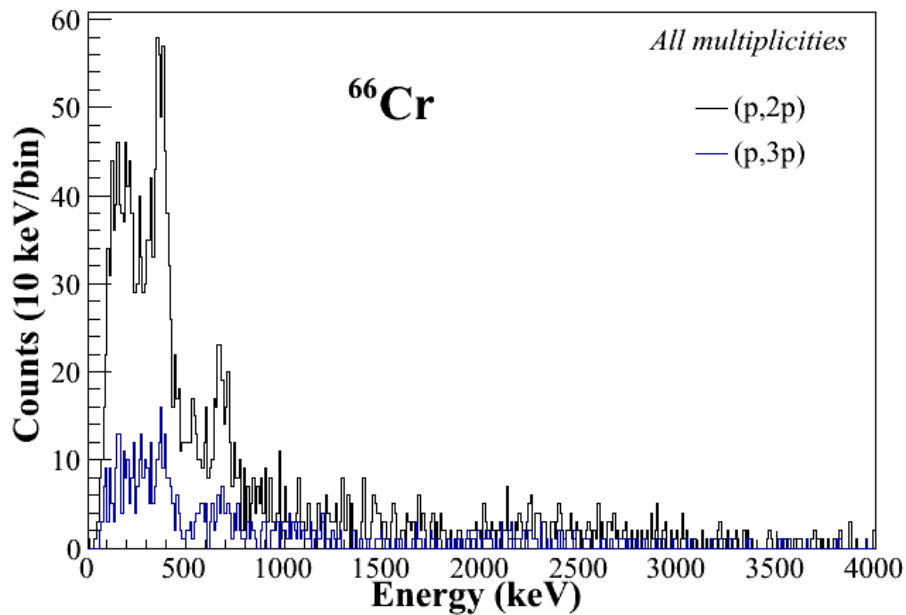


Fig. 6.1 – Doppler-corrected γ -ray spectra of ^{66}Cr populated from $^{67}\text{Mn}(p, 2p)$ in black and $^{68}\text{Fe}(p, 3p)$ reactions in blue with addback correction (maximum distance of 15 cm without energy threshold). All multiplicities are shown.

^{66}Cr . The $^{67}\text{Mn}(p, 2p)^{66}\text{Cr}$ and $^{68}\text{Fe}(p, 3p)^{66}\text{Cr}$ reaction channels are selected from the PID in the BigRIPS and ZeroDegree spectrometers created in Section 5.1. The DALI2 and MINOS calibrations (Sections 5.2 and 5.3) are taken into account as well as the position optimization

between the DALI2 and MINOS structures from the ^{68}Fe test case (Section 5.2). Addback of γ -rays distant by less than 15 cm was performed mainly to infer the high energy structure of the spectrum. Eventually, the ^{66}Cr energy spectrum is created with addback, as seen in Fig. 6.1. The contributions from $(p, 2p)$ and $(p, 3p)$ reactions are summed up in Fig. 6.2.

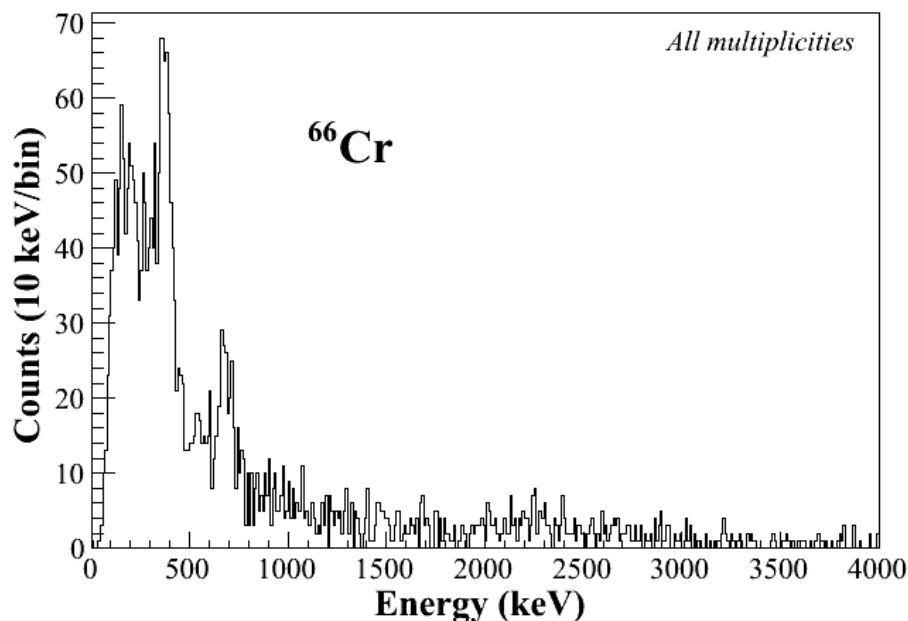


Fig. 6.2 – Doppler-corrected γ -ray spectrum of ^{66}Cr populated from the summed $^{67}\text{Mn}(p, 2p)$ and $^{68}\text{Fe}(p, 3p)$ reactions with addback correction (maximum distance of 15 cm). All multiplicities are shown.

As a first step, an energy spectrum is produced by taking all the DALI2 crystal multiplicities to find all transitions populated in the experiment. Then, all the different multiplicities are looked at and higher multiplicities are removed in the final spectrum shown in Fig. 6.3 to reduce the atomic background while conserving the statistics in the transitions. Two peaks are found in the spectrum which would yield one or two γ rays in an event. Due to the limitation of statistics, we looked at multiplicities lower than five γ . Two transitions are measured for the first time at 386(9) keV and 683(9) keV. These energy values are obtained from a fit: it contains the simulated GEANT4 response of DALI2 for the two different transitions and a background with a two exponential function for low and high energies. In the simulations, we consider the experimental intrinsic resolutions of each crystal as a function of energy obtained with a square root fit from the five peaks of the three sources (cf. Fig. 5.8). Due to limited statistics, no other transition is observed. An accumulation of statistics is found between 2 and 2.5 MeV but difficult to assign to transitions.

Gamma-gamma coincidences are analyzed for the two transitions. Per event, a gate is set on one of the two transitions and all the other γ rays detected in DALI2 crystals at the same time fill the coincidence spectrum. In Fig. 6.4 are shown the spectra in coincidence with the

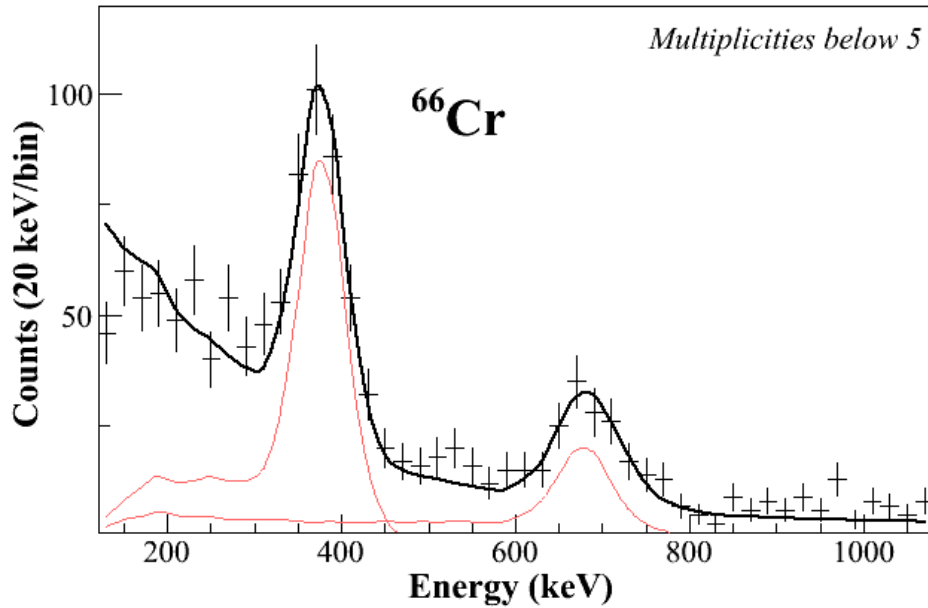


Fig. 6.3 – Doppler-corrected γ -ray spectrum of ^{66}Cr populated from the summed $(p, 2p)$ and $(p, 3p)$ reactions: the experimental data points, the simulated response of each transition (red), and the sum of these simulated transitions with a two-exponential background (black). Multiplicities below five are shown.

first and second transitions. With a gate on the first transition at 386(9) keV, the second one at 683(9) keV is clearly visible and vice versa, revealing a coincidence between the two transitions. With the gate on the first transition, the self-coincidence seen comes from random coincidences of photons.

We now discuss the spin assignment of the populated states. From relative intensities of the transitions and their coincidences and from the systematics along the Cr isotopic chain (cf. Section 1.3.2), the first two γ -ray lines are assigned to the $2_1^+ \rightarrow 0_1^+$ and $4_1^+ \rightarrow 2_1^+$ transitions with the latter transition feeding the $2_1^+ \rightarrow 0_1^+$ transition. The proposed level scheme of ^{66}Cr is presented in Fig. 6.5. As another argument, the ground state of ^{67}Mn has been assumed to be a $5/2^-$ from the systematics in Ref. [129] (there seems to be an error in the Fig. 5 of this reference showing a $5/2^+$ ground state for ^{67}Mn). To produce positive parity states, the proton needs to be knocked out from odd orbital angular momentum orbitals. As in ^{67}Mn the proton shells are filled up to the $f_{7/2}$ shell, containing five out of eight possible protons, the proton knockout will occur in the pf shells. The proton knockout occurring in the $f_{7/2}$ shell ($l = 3$) will then lead to $J = \{ 7/2 - 5/2, \dots, 5/2 + 7/2 \} = \{ 1^+, \dots, 6^+ \}$ states. The relative intensities of the first 2^+ and 4^+ states populated from $(p, 2p)$ and $(p, 3p)$ are similar for ^{66}Cr as well as for ^{68}Fe where the $4_1^+ \rightarrow 2_1^+$ transition is unambiguously assigned in the literature [128].

The half-lives of the γ -ray emitting states shift the emission point of the γ rays compared to the reaction vertex position. This produces a shift in the Doppler corrected energy spectrum, for example 8 keV for a 50 ps half-life and a 386 keV transition. This is shown for a 370 keV

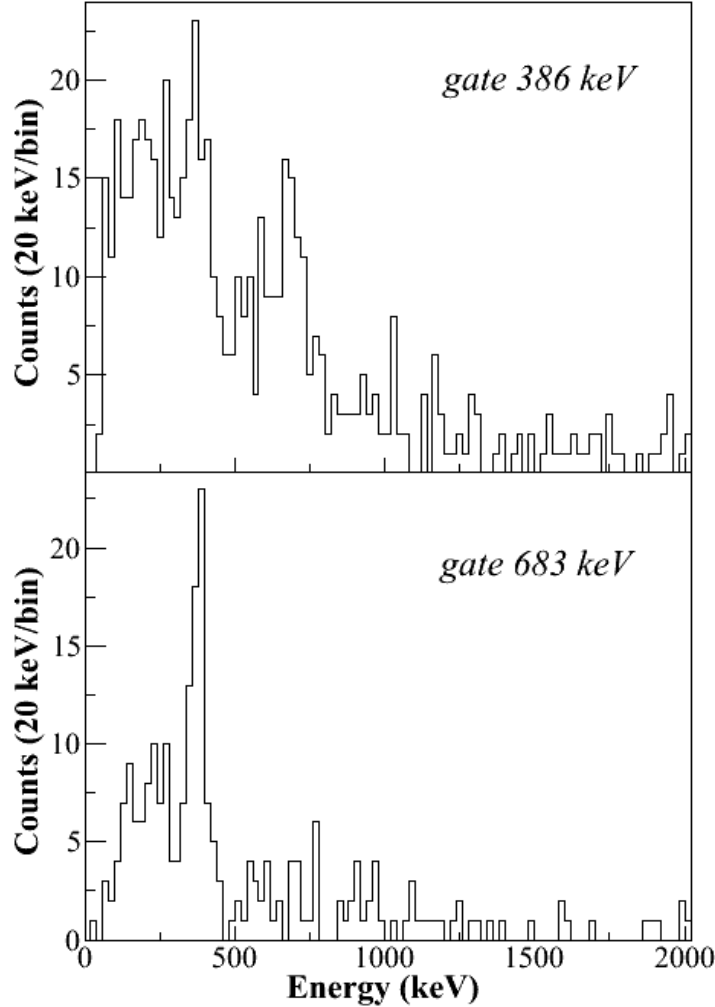


Fig. 6.4 – Gamma-gamma coincidence spectra for multiplicities below five with a gate on (top) the first transition at 386(9) keV and on (bottom) the second transition at 683(9) keV.

transition and different lifetimes in Fig. 6.6. Therefore the γ rays are not Doppler corrected with the real vertex position and velocity and the peak positions will shift towards lower energies. The peak will deform on the lower energy side with a higher width of the transition. In agreement with known half-lives in this mass region and with the measured widths of the transitions too wide without lifetime, we considered the half-life of 2_1^+ states to be consistent with 50 ps for ^{66}Cr in the simulation for the fit. The uncertainty on this half-life is considered to be ± 50 ps and is included in the energy uncertainties for the $2_1^+ \rightarrow 0_1^+$ transition. 4_1^+ states are considered short-lived ($\tau_{1/2} < 10$ ps). The half-life uncertainty is added quadratically to statistical and energy calibration (5 keV) uncertainties to produce the total uncertainty given above.

The measured 2_1^+ excitation energy of ^{66}Cr is lower than the measured 2_1^+ state of ^{64}Cr and the $R_{4/2}$ ratio given with the second excited state measurement, showing that neutron-rich Cr

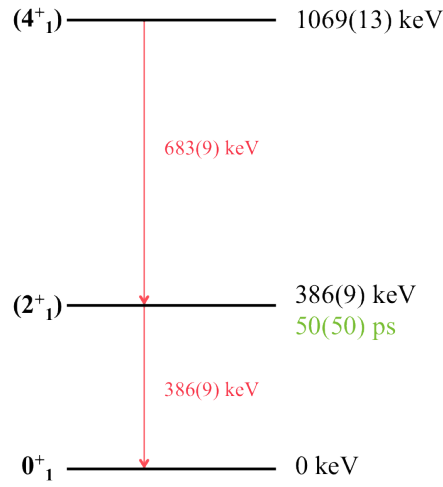


Fig. 6.5 – Proposed level scheme of ^{66}Cr .

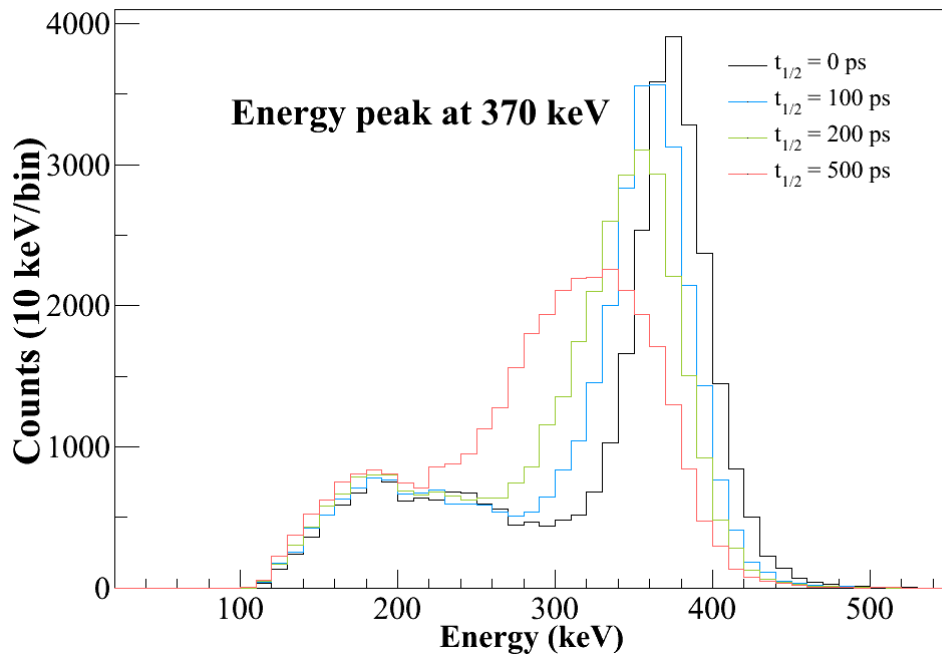


Fig. 6.6 – Simulated 370 keV transition responses for 0, 100, 200, 500 ps half-lives.

isotopes are more collective beyond $N=40$.

^{65}Cr . The energy spectrum of ^{65}Cr is also extracted from the $^{66}\text{Mn}(p, 2p)^{65}\text{Cr}$ and $^{67}\text{Fe}(p, 3p)^{65}\text{Cr}$ reaction channels and shown in Fig. 6.7. For now, no identification of the possible transitions has been performed due to the lack of systematics for the Cr odd isotopes in this region of

development of collectivity and due to the absence of comparison to theoretical models. Nevertheless, three possible transitions arise at around 400, 500, and 700 keV, as well as a bump between 1500 and 2000 keV. This work in progress will be further analyzed in a later stage.

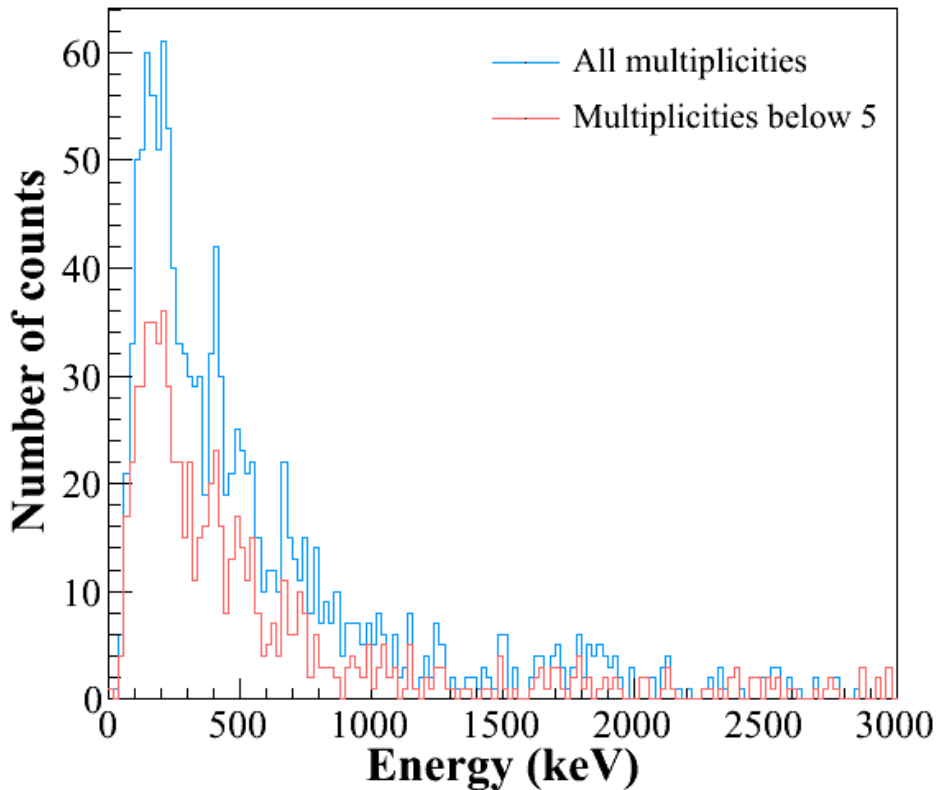


Fig. 6.7 – Doppler-corrected experimental γ -ray spectra of ^{65}Cr populated from $^{66}\text{Mn}(p, 2p)$ reaction with adback (all multiplicities in blue and multiplicities below 5 γ in red).

6.2 Cross section

6.2.1 Inclusive cross sections

The cross section is an effective area that quantifies the likelihood of a scattering event when an incident beam particle impinges on a target. The inclusive cross section σ_{incl} in our experiment represents the probability of $(p, 2p)$ knockout reactions for ^{66}Cr and ^{65}Cr . For the case of $^{67}\text{Mn}(p, 2p)^{66}\text{Cr}$ as an example, the cross section is given by

$$N(^{66}\text{Cr}) = \sigma_{incl} n_{dc} I(^{67}\text{Mn}) \quad (6.1)$$

where $N(^{66}\text{Cr})$ is the number of ^{66}Cr nuclei produced in the target and $I(^{67}\text{Mn})$ is the number of ^{67}Mn entering the target. $n_{dc} = \rho_{LH_2} L_{LH_2} N_A / M_H$ is the number of scattering centers per cm^2 in a 102 mm target length with a hydrogen target length $L_{LH_2} = 102(1)$ mm and density $\rho_{LH_2} =$

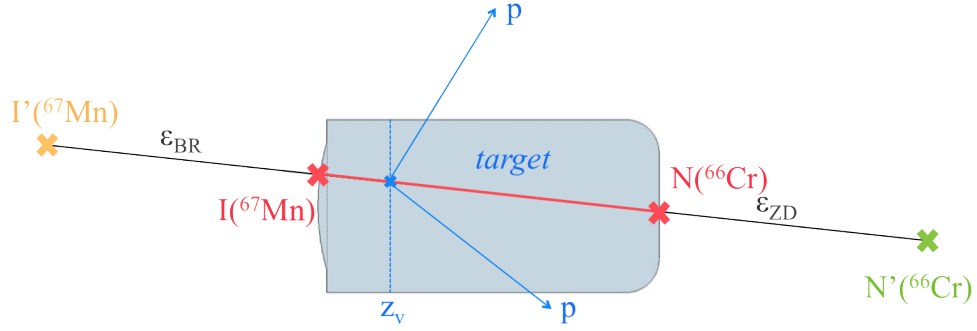


Fig. 6.8 – Scheme for inclusive $(p, 2p)$ cross section measurement.

	Number of BigRIPS nuclei	Number of ZeroDegree nuclei	Inclusive cross section
$^{67}\text{Mn}(p, 2p)^{66}\text{Cr}$	49762	67	5.1(9) mbarn
$^{68}\text{Fe}(p, 3p)^{66}\text{Cr}$	917063	13	54(16) μ barn
$^{66}\text{Mn}(p, 2p)^{65}\text{Cr}$	70897	39	2.1(4) mbarn
$^{67}\text{Fe}(p, 3p)^{65}\text{Cr}$	713251	5	27(12) μ barn

Tab. 6.1 – Inclusive knockout cross sections and number of counts in the different reaction channels for the F7 DS (Downscaled by 20) trigger.

70.973 kg/m³ at atmospheric vapor pressure, the Avogadro number $N_A = 6.02 \times 10^{23}$ atoms/mol, and $M_H = 1.008$ g/mol. We then obtain for the target $n_{dc} = 4.32 \times 10^{23}$ diffusing centers per cm². However, we can only measure the number of ^{67}Mn in the BigRIPS spectrometer and the ^{66}Cr in the ZeroDegree spectrometer. The overall transmission of the BigRIPS and ZeroDegree lines, including the efficiency and acceptances of the beam line, need to be taken into account and we finally have

$$\sigma_{incl} = \frac{N'(^{66}\text{Cr})}{I'(^{67}\text{Mn})} \frac{1}{T n_{dc}} \quad (6.2)$$

where $T = 0.61(8)$ is the total transmission of the experimental line measured in Section 5.1 taking into account the efficiencies of the beam detectors but also the transmission loss in the hydrogen target, as well as the acceptance of the ZeroDegree line. Charge state changes are not considered in this calculation, in agreement with their absence in the ionization chambers and LISE calculations [126] predicting 1% or less of charge states in the region. The scheme of inclusive cross section measurement is shown in Fig. 6.8. The number of incident nuclei $I'(^{67}\text{Mn})$ is measured with the downscaled F7 trigger and the number of nuclei of interest $N'(^{66}\text{Cr})$ in ZeroDegree is counted with the same trigger to use the transmission in the same conditions and take into account the acceptance of ZeroDegree. The same method is applied to determine inclusive $(p, 3p)$ cross sections.

We finally obtain the inclusive cross sections shown in Table 6.1. From Ref. [130], the removal of k deeply bound protons is a constant ten to hundred times the removal of $(k + 1)$

deeply bound protons. Form the data extracted, the inclusive cross section of $(p, 2p)$ is 94 and 78 times larger than the $(p, 3p)$ cross section for ^{66}Cr and ^{66}Cr respectively, which is in rough agreement with Ref. [130].

We can compare the $(p, 3p)$ inclusive cross sections with the experimental data of Ref. [71] at around 130 MeV/nucleon in the N=40 region. The inclusive cross section of $^{68}\text{Ni}(p, 3p)^{66}\text{Fe}$ at N=40 is measured at $\sigma_{incl} = 1.42(25)$ mbarn while the inclusive cross section of $^{70}\text{Ni}(p, 3p)^{68}\text{Fe}$ at N=42 drops at $\sigma_{incl} = 0.49(5)$ mbarn, which was claimed to indicate a significant change in nuclear structure between N=40 and N=42. They also measure the $^{66}\text{Fe}(p, 3p)^{64}\text{Cr}$ inclusive cross section at $\sigma_{incl} = 0.13(5)$ mbarn. If we compare to our knockout data, the N=42 $(p, 3p)$ inclusive cross section for ^{66}Cr is of the same order of magnitude, although smaller by a factor ~ 2.5 . At this stage, the discrepancy could come from differences in both structure or reaction mechanism, one being an heavy-ion induced two-nucleon removal, the other one being a two proton removal from a proton target. An analysis of several $(p, 2p)$ and $(p, 3p)$ inclusive cross sections is ongoing and should allow a more systematic comparison with heavy-ion induced cross sections.

The $^{66}\text{Co}(^9\text{Be}, X)^{65}\text{Fe}$ reaction has been recently measured at the NSCL (MSU, USA). The analysis will be soon available with exclusive cross sections [131].

6.2.2 Exclusive cross sections

To determine the exclusive cross sections of the two transitions in ^{66}Cr , the spectra from the $(p, 2p)$ and $(p, 3p)$ channels are analyzed separately with all the DALI2 multiplicities and fit with the GEANT4 simulation peaks produced in Section 6.1. The normalizing factors $A_{1/2}$ of the peaks taken to fit the experimental spectrum will enable us to obtain the number of γ rays $N(\gamma_{1/2})$ produced by

$$N(\gamma_{1/2}) = \frac{A_{1/2}N_{sim}}{N_{incident}} \quad (6.3)$$

with $N_{sim} = 50000$ the number of events simulated to produce the DALI2 simulated peaks and $N_{incident}$ the number of incident nuclei with the F7 trigger (one needs to multiply by the Downscaled factor 20 the number of nuclei counted for the inclusive cross sections with the F7 DS trigger).

The exclusive cross sections are then given in Tab. 6.2 using

$$\sigma_{excl}(\gamma_{1/2}) = \frac{A_{1/2}N_{sim}}{N_{incident} \times \epsilon_{MINOS} \times n_{dc}T} \quad (6.4)$$

with n_{dc} the number of atoms per cm^2 in the target and T the overall transmission as used in Section 6.2.1. $\epsilon_{MINOS} = 96(4)\%$ is the MINOS efficiency to detect at least one proton for a 10 cm target length, given by simulations on the $^{79}\text{Cu}(p, 2p)^{78}\text{Ni}$ case and presented in Section 2.3.

As the two transitions are in coincidence with each other, when a $4_1^+ \rightarrow 2_1^+$ transition is detected, the $2_1^+ \rightarrow 0_1^+$ γ -ray is also emitted. To calculate the exclusive cross sections to each of the transitions, one then needs to subtract the coincident transition cross sections. We see no other transition in the spectrum, and therefore no other feeding source for the exclusive cross sections. For the 2_1^+ state, we subtract the feeding from the 4_1^+ state and obtain the exclusive

	$^{67}\text{Mn}(p, 2p)^{66}\text{Cr}$	$^{68}\text{Fe}(p, 3p)^{66}\text{Cr}$
$\sigma_{excl}(0_1^+)$	1.9(13) mbarn	15(25) μ barn
$\sigma_{excl}(2_1^+)$	1.0(8) mbarn	14(16) μ barn
$\sigma_{excl}(4_1^+)$	2.2(5) mbarn	25(11) μ barn
$\sigma_{excl}(6_1^+)$	< 0.2(2) mbarn	< 12(11) μ barn
σ_{incl}	5.1(9) mbarn	54(16) μ barn

Tab. 6.2 – Exclusive knockout cross sections for the 0_1^+ , 2_1^+ , 4_1^+ , and 6_1^+ states.

Excited states	Spectroscopic amplitudes for the populated orbitals
0_1^+	0.00509 from the $f_{5/2}$ orbital
2_1^+	0.655 from the $f_{7/2}$ orbital 0.00275 from the $p_{3/2}$ orbital 0.0140 from the $f_{5/2}$ orbital 3.81×10^{-5} from the $p_{1/2}$ orbital
4_1^+	0.596 from the $f_{7/2}$ orbital 0.00109 from the $p_{3/2}$ orbital 0.00217 from the $f_{5/2}$ orbital
6_1^+	0.0414 from the $f_{7/2}$ orbital

Tab. 6.3 – Spectroscopic amplitudes calculated for the 0_1^+ , 2_1^+ , 4_1^+ , and 6_1^+ states, assuming no other populated transition in ^{66}Cr .

cross section presented in Tab. 6.2. For the 0_1^+ ground state, we can extract an exclusive cross section by taking the inclusive cross section and subtracting the 4_1^+ and 2_1^+ feedings. We can also extract a maximum exclusive cross section for the possible 6_1^+ excited state around 900 to 1000 keV from the suggested shell model calculations predicting a 6_1^+ excited state around 960 keV.

We can compare the $(p, 3p)$ exclusive cross sections with the $^{38}\text{Si}(^9\text{Be}, X)^{36}\text{Mg}$ experiment reported in Ref. [52]. The first excited state can be measured and the exclusive cross sections measured for the 0_1^+ ground state and 2_1^+ first excited state of $\sigma_{excl}(0_1^+) \approx 58(9)$ μ barn and $\sigma_{excl}(2_1^+) \approx 42(8)$ μ barn. The extracted cross sections here are of the same order of magnitude than for ^{36}Mg and the ground state and excited state both have similar exclusive cross sections.

We can compare in a preliminary study the $(p, 2p)^{66}\text{Cr}$ exclusive cross sections with theory using:

$$\sigma_{i \rightarrow j} = \sum_{n,l} C^2 S(i \rightarrow j, nl) \sigma_{sp}^i(n, l). \quad (6.5)$$

with the spectroscopic factors $C^2 S$, the ratios of single particle cross sections from Shell Model calculations σ^{sp} , and the exclusive cross section $\sigma_{i \rightarrow j}$ from state i to state j . The spectroscopic amplitudes S , shown in Tab. 6.3, are given by the shell model calculations with the LNPS-m interaction described below in Section 6.3 from F. Nowacki. The single-particle cross sections

$\sigma_{excl}(0_1^+)$	14 μbarn
$\sigma_{excl}(2_1^+)$	1.8 mbarn
$\sigma_{excl}(4_1^+)$	1.7 mbarn
$\sigma_{excl}(6_1^+)$	0.11 mbarn
σ_{incl}	3.6 mbarn

Tab. 6.4 – Theoretical exclusive ($p, 2p$) knockout cross sections for the 0_1^+ , 2_1^+ , 4_1^+ , and 6_1^+ states of ^{66}Cr from the single-particle cross sections with the eikonal/DWIA formalism and the spectroscopic amplitudes from the shell model calculations with the LNPS-m interaction.

are given by C. Bertulani (Texas A & M, USA) within the eikonal/DWIA formalism [37] for the $1f_{7/2}$ orbital at $E_2 = 260$ and $E_1 = 200$ MeV/nucleon ^{67}Mn incident energies with

$$\sigma_{sp}(1f_{7/2}, E_1) = 3.045 \text{ mbarn}$$

and

$$\sigma_{sp}(1f_{7/2}, E_2) = 2.429 \text{ mbarn.}$$

The ^{67}Mn energy at the vertex position is comprised between 260 and 200 MeV/nucleon between the beginning and end of the target. To calculate the single-particle cross section at vertex position, we take the mean vertex position found for the reaction at around 50.96 mm from the beginning of target and obtain from LISE calculations its corresponding mean energy $E_m \approx 232$ MeV/nucleon. We then perform a linear regression to find the single particle cross section for the mean incident energy E_m :

$$\sigma_{sp}(1f_{7/2}, E_m) = \sigma_{sp}(1f_{7/2}, E_1) - \frac{E_1 - E_m}{E_1 - E_2} \times (\sigma_{sp}(1f_{7/2}, E_1) - \sigma_{sp}(1f_{7/2}, E_2)) \approx 2.755 \text{ mbarn.}$$

We consider the contributions from the p orbitals negligible and the $1f_{7/2}$ and $1f_{5/2}$ single-particle cross sections comparable. We can then calculate the exclusive cross sections up to the 6_1^+ excited state, presented in Tab. 6.4.

The theoretical and experimental exclusive cross sections are comparable for the excited states: it implies that these first excited states mainly come from the knockout in the $1f_{7/2}$ or $1f_{5/2}$ orbitals. For the 0_1^+ ground state, the theoretical cross section is smaller than the experimental one. This discrepancy could come from the missing $1f_{5/2}$ orbital in the calculations. The resulting theoretical ($p, 2p$) inclusive cross section is a bit smaller than the experimental one. This seems natural as only f orbitals have been taken into account in the single-particle cross sections. These theoretical calculations are very preliminary and other orbitals will be included to check the evolution of the 0_1^+ exclusive cross section. Further analysis needs to be performed to understand these discrepancies: the single-particle cross sections of the $f_{5/2}$ orbital and others will be included and calculations for other excited states of ^{66}Cr will be performed with shell model to see if other states are populated in the theory.

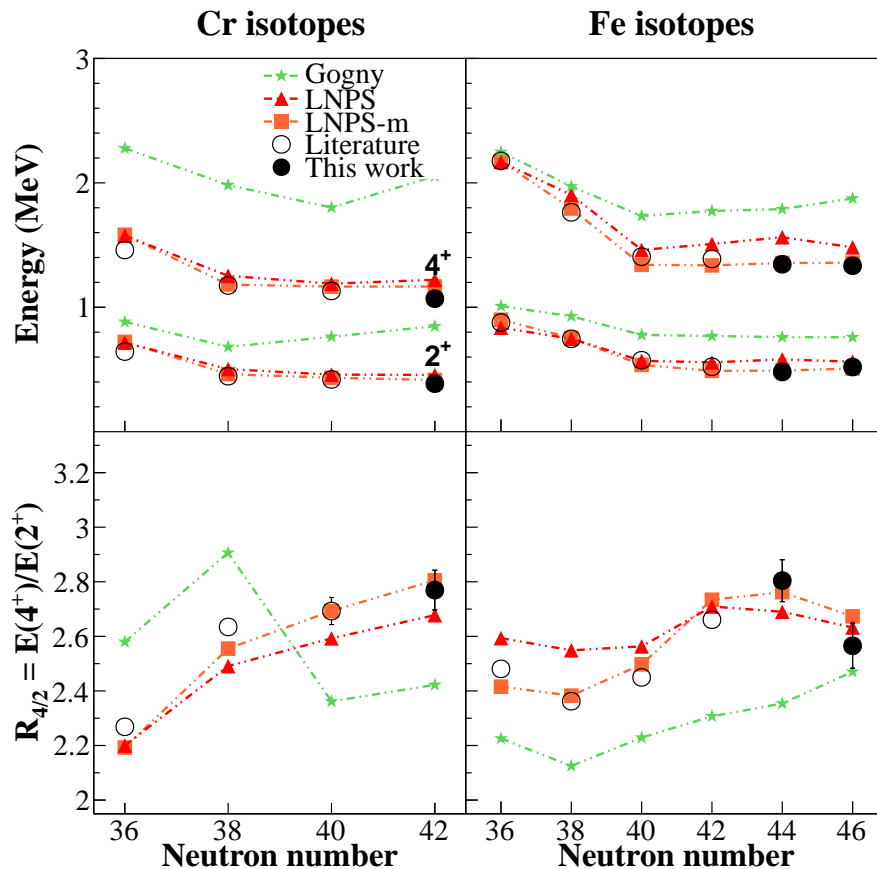


Fig. 6.9 – Systematics of Cr and Fe isotopes compared to the shell model calculations using the LNPS original [67] and modified interactions, and also to the Hartree-Fock-Bogoliubov + 5-dimension Collective Hamiltonian calculations using the Gogny force [68, 69].

6.3 ^{66}Cr and collectivity beyond $N=40$ below ^{78}Ni

The evolution of 2_1^+ and 4_1^+ states is presented on top of Fig. 6.9 for the Cr and Fe chains. The $^{70,72}\text{Fe}$ isotopes have been analyzed by C. Louchart (TU Darmstadt, Germany) using the same analysis code and method. The measured 2_1^+ , 4_1^+ energies reveal a rather flat behavior from $N=38$ to $N=42$, which points to a lack of deformation evolution beyond $N=40$. ^{66}Cr is therefore also deformed and the data suggest an indication of the extension of the Island of Inversion beyond $N=40$ for ^{66}Cr and $^{70,72}\text{Fe}$.

Collective model. Let us first look at the systematics with a simple collective model as described by Bohr and Mottelson [132]. Consider the assumption of a pure rigid rotor, the rotational energies in the nucleus can be written as

$$E_{rot} = \frac{\hbar^2}{2\mathfrak{S}} J(J+1) \quad (6.6)$$

with \mathfrak{S} the moment of inertia of the system, and J the total angular momentum of the excited state. The energies can be expressed as a function of $J(J+1)$. We then obtain $E_{rot}(J) \propto J(J+1)$

and $R_{4/2} = 4 \times 5 / (2 \times 3) \approx 3.33$. The Cr isotopic chain shows a maximum of collectivity for ^{66}Cr with the lowest 2_1^+ energy and highest $R_{4/2}$ ratio of 2.8. This value is high but lower than 3.3, showing that neutron-rich Cr isotopes, although very collective, are not rigid rotors.

The actual maximum of deformation cannot be inferred from such a simplified model and we need to compare our experimental results with a theory to confirm the extension of the Island of the Inversion within the model and to quantify the maximum of deformation in this region.

Gogny interaction. We compare the results with the beyond-mean field HFB database [68] and with Ref. [129] for the Fe isotopes recalculated for a better convergence of the results, derived from Hartree-Fock-Bogoliubov (HFB) calculations with the Gogny D1S interaction. The HFB approximation takes into account pairing correlation in this mean-field model, and some of the terms in a Gogny formulation have a finite range defined by a gaussian $\exp(-(\vec{r}_1 - \vec{r}_2)^2/\mu^2)$ while all the terms in a Skyrme formulation have zero-range $\delta(\vec{r}_1 - \vec{r}_2)$. The calculations, shown in Fig. 6.9 with the green stars, reproduce the trend of 2_1^+ and 4_1^+ energies in Cr and Fe isotopes up to $N=38$ and $N=40$ respectively but are all giving too high excited state energies. However, from $N=40$ and $N=42$ in the Cr and Fe chains, the calculations do not follow the trend. For Cr isotopes, the HFB-based calculation indicates a lowering of the collectivity from $N=40$ with a lower $R_{4/2}$ ratio and an increase of excited state energies from $N=42$. For Fe isotopes, the 2_1^+ and 4_1^+ energies appear to follow the trend but the $R_{4/2}$ ratio beyond $N=38$ steadily increases without reproducing the local maximum at $N=44$ seen in the data. With the HFB-based calculations, the Cr and Fe isotopes stay deformed up to $N=50$ with a slight decrease of collectivity compared to $N=40$. The interpretation of the discrepancies between our data and predictions with the Gogny D1S force are still to be done. As a second step, the inclusion of an explicit tensor term in the Gogny force could improve the experimental results in this region. In another step, a further comparison to other beyond the mean field calculations such as the full Generator Coordinate Method (GCM) with the Gogny interaction [133] and Skyrme interactions [134] may help to understand the discrepancies.

LNPS and LNPS-m interaction. Furthermore, state-of-the-art shell model calculations were performed by F. Nowacki (IPHC Strasbourg, France) which successfully described the new Island of Inversion at $N=40$ [67]. In this model, a core of ^{48}Ca is used with a valence space composed of the pf proton orbitals and $p_{1/2}$, $f_{5/2}$, $g_{9/2}$, and $d_{5/2}$ neutron orbitals. The valence space includes the entire pf proton orbitals because the $p_{3/2}$ and $f_{5/2}$ proton orbital energies are inverted between $N=40$ and $N=50$ in this shell model picture. The overall 2_1^+ , 4_1^+ trends in systematics and observed plateaus are reproduced by the calculations. The $d_{5/2}$ neutron orbital is essential in this LNPS interaction to correctly reproduce the trend in the Cr and Fe isotopes at $N=40$.

However calculations with the LNPS initial effective hamiltonian from Ref. [67] show too low predictions for the 2_1^+ excitation energies of the most neutron-rich Cr isotopes. An extra binding $gd - gd$ monopole term is added in the hamiltonian denoted here LNPS-m, to optimize the interpretation of the physics of the overall region. The physics at $N=40$ remains unchanged with respect to this new LNPS-m hamiltonian (in respect for example to the occupancies and wave function decomposition for ^{64}Cr shown in Tab. I and II of Ref. [67]).

Using the rotational limit, we can make a connection between the laboratory and intrinsic

Tab. 6.5 – Energies and quadrupole deformation properties of Cr isotopes. Energies are in MeV, $B(E2)$ in $e^2 \text{ fm}^4$, and quadrupolar momenta in $e \text{ fm}^2$. Experimental energies are the same as Fig. 6.2. .

	^{62}Cr	^{64}Cr	^{66}Cr	^{68}Cr
$E^*(2_1^+)$ exp.	0.44	0.42	0.39	-
$E^*(2_1^+)$ theo.	0.46	0.43	0.42	0.41
Q_{spec}	-38	-38	-39	-38
$B(E2)_{\downarrow th.}$	378	388	389	367
Q_{int} from Q_{spec}	135	136	137	132
Q_{int} from $B(E2)$	138	140	140	136
$\langle \beta \rangle$	0.33	0.33	0.32	0.30
$E^*(4_1^+)$ exp.	1.17	1.13	1.07	-
$E^*(4_1^+)$ theo.	1.18	1.13	1.06	1.15
Q_{spec}	-49	-49	-46	-47
$B(E2)_{\downarrow th.}$	562	534	562	530
Q_{int} from Q_{spec}	135	134	134	130
Q_{int} from $B(E2)$	141	140	141	137
$\langle \beta \rangle$	0.34	0.33	0.32	0.31

frames using the relations from Ref.[67]:

$$Q_{int} = \frac{(J+1)(2J+3)}{3K^2 - J(J+1)} Q_{spec}(J), \quad K \neq 1,$$

and

$$B(E2, J \rightarrow J-2) = \frac{5}{16} e^2 |\langle JK20 | J-2, K \rangle|^2 Q_{int}^2,$$

for $K \neq \frac{1}{2}, 1$, with Q_{int} and Q_{spec} the intrinsic and spectroscopic quadrupole momenta, and $B(E2, J \rightarrow J-2)$ the reduced transition probabilities. The quadrupole properties of these nuclei are summarized in Tab. 6.5. The calculated high $B(E2)$'s around $400 e^2 \text{ fm}^4$, high intrinsic and spectroscopic quadrupole moments all in agreement, and deformation β around 0.3 are consistent with a first-order description of the studied isotopes as prolate deformed rotational nuclei.

In the Cr chain, the deformation is nearly constant, reflected by almost constant 2_1^+ , 4_1^+ excitation energies. To find the maximum of deformation, an inspection of the wave function content is needed to find the percentage of different particle-hole excitations in the ground states of Cr isotopes, as presented in Tab. 6.6. The isotopes with the higher percentage of two-particle two hole excitations or more corresponds to the more deformed nucleus. A maximum is then found at N=40 for ^{64}Cr with the intrinsic shape of deformation $\beta \sim 0.33$, a reduced transition probability $B(E2)_{\downarrow th} \sim 388 e^2 \text{ fm}^4$, and sizable $6p6h$ excitations with respect to other Cr isotopes. To understand the flat yet decreasing 2_1^+ excitation energies in the Cr chain up to N=42 while the deformation decreases after N=40, we need to extract the different contributions

Tab. 6.6 – Occupation of neutron intruder orbitals and percentage of particle-hole excitations across the $N = 40$ gap in the ground states of Cr isotopes. The last column features the pairing correlations energy differences (in MeV) evaluated between the ground state and the 2_1^+ state.

Nucleus	$n^\nu(g_{9/2} + d_{5/2})$		0p0h	2p2h	4p4h	6p6h	$\Delta E_{Pairing}^*$
	IPM	SM					
^{60}Cr	0	1.8	14	75	7	0	1.84
^{62}Cr	0	3.5	1	25	71	3	1.49
^{64}Cr	0	4.3	0	8	71	20	1.25
^{66}Cr	2	5.2	0	40	56	3	1.13
^{68}Cr	4	6.0	6	79	11	0	1.24

of ground and excited states energies. As already described in Section 1.2.1 with Eq. 1.2, the Hamiltonian can be decomposed into a monopole and multipole term, the latter one coming for the most part from pairing and quadrupole correlations. From this decomposition, we extract the pairing expectation values for the ground state and the first 2^+ state. We can then obtain, shown in Tab. 6.6, the pairing correlations energy differences evaluated between the ground state and the 2_1^+ state. We observe a steady decrease of pairing correlations up to ^{66}Cr . While the quadrupoles correlations decrease and should result in higher first excited state energies, the decrease in pairing correlations is the reason for the decrease of 2_1^+ excited state energy from ^{64}Cr to ^{66}Cr . There is therefore a delicate interplay between quadrupole and pairing correlations which determines the final apparent spectra in the Cr isotopes. ^{66}Cr is found still in the Island of Inversion but the maximum of deformation is found for ^{64}Cr at $N=40$.

The Fe chain exhibits the same behavior, with smallest 2_1^+ excitation energy and larger $R_{4/2}$ for ^{70}Fe at $N=44$. Similarly, the inspection of quadrupole moments, intrinsic shape of deformation and inspection of the wave function content all show a maximum for the $N=42$ Fe isotope instead and ^{70}Fe shows the smallest 2_1^+ excitation energy because of pairing correlations difference and not because of larger quadrupole correlations.

The present LNPS-m interaction reproduces better the data than the initial LNPS interaction by introducing more intruder configurations in the ground state of the nuclei. This point may be an indication of the extension of the Island of Inversion towards $N=50$ and should be investigated by further measurements. The experimental results and interpretation have been recently accepted for publication (cf. Appendices). Shell-model calculations at $N=50$ have not been conducted as they might have a too restrictive neutron valence space and the $s_{1/2}$ orbital might influence the deformation at $N=50$.

Preliminary calculations in an extended $pf - sdg$ $0\hbar\omega$ valence space indicate that the actual Island of Inversion is relayed from $N=46$ by quadrupole excitations across the $N=50$ gap [135], as already observed in light nuclei along the Mg chain with the merging of the $N=20$ to $N=28$ Islands of Inversion [63, 136].

Based on these new measurements, it seems important to extend the shell model valence space (at least the $3s_{1/2}$ orbital) and perform predictions up to $N=50$ to further investigate

the possibility of the disappearance of $N=50$ as a magic number below ^{78}Ni . Such quantitative predictions would be a strong motivation for further (and more exotic) experiments, as well as the development of new generation RIB facilities.

CONCLUSION

The MINOS device has been developed until mid-2013 for in-beam spectroscopy of very exotic nuclei from proton knockout reactions. The hydrogen target has been conceived and built from the experience from the PRESPEC target [89] and fully tested in RIKEN in Summer 2013. The Time Projection Chamber has been developed based on the design of the PANDA TPC prototype [94] and the expertise from CEA-IRFU in conceiving gas detectors and Micromegas detectors. At first, different solutions for the subparts of the TPC were tested in a test chamber, MIMAC, with an α source and cosmic-ray measurements. Cosmic rays were detected for the first time using the MIMAC chamber in early 2013 and validated the use of a Micromegas detector as having enough amplification to induce well-above noise signals on the detection pads. The first TPC prototype was finished in May 2013, and we used a cosmic-ray bench to estimate the efficiency of the TPC. We obtain a 73.3(7) % efficiency for cosmic muons, leaving a bit less energy than 300 MeV protons, which validates the 100 % efficiency of the MINOS TPC for protons at the targeted energies of 50-200 MeV.

Full-scale GEANT4 simulations of two physics cases, the spectroscopy of ^{52}Ar and ^{78}Ni with $(p, 2p)$ knockout reactions, calculated with the tracking algorithm software the expected vertex position resolutions around 4 mm Full Width Half Maximum (FWHM) with the MINOS TPC geometry and a geometrical and tracking efficiency of more than 90 %.

The MINOS device was then shipped to Japan for an in-beam test and physics experiments. An in-beam performance test was performed at the HIMAC medical facility (Chiba, Japan) with two thin targets instead of the thick hydrogen to validate the tracking algorithm and the vertex position resolution. I developed a complete tracking algorithm for the offline analysis based on the Hough transform to select and filter the tracks from the raw data. Vertex position resolutions of 5 to 8 mm FWHM were found for the two CH_2 targets without particle identification of the residue nor subtraction of the Carbon contribution in the resolution. These values were consistent with realistic simulations vertex resolution, validating the TPC with respect to the specifications for in-beam experiments of less than 5 mm FWHM. The results of this in-beam test and the tracking algorithm are presented in an article in preparation. I implemented an online analysis for the MINOS TPC inside the Anaroot online of the RIBF to read and analyze the RIBF data stream during experiments.

The first physics campaign took place in May 2014 with the first SEASTAR campaign [39] with the first spectroscopy of ^{66}Cr , $^{70,72}\text{Fe}$, and ^{78}Ni . The ^{66}Cr was the first measurement using MINOS. The analysis of the ^{66}Cr spectroscopy revealed two transitions at 386(9) and 683(9) keV assigned to the $2_1^+ \rightarrow 0_1^+$ and $4_1^+ \rightarrow 2_1^+$ transitions respectively from systematics and shell

model calculations, as well as width comparison with the detector simulated responses. These measurements suggest a maximum of collectivity for ^{66}Cr at $N=42$ with the lowest 2_1^+ excited state energy and the highest $R_{4/2}$ ratio. An interpretation with shell model calculations by F. Nowacki (IPHC, France) shows that the maximum of quadrupole collectivity occurs at $N=40$ along the Cr isotopic chain. ^{66}Cr is still placed in the Island of Inversion region of $N=40$ and the shell model calculations as well as comparison with HFB-based calculations [68, 129] suggest an extension of the $N=40$ Island of Inversion towards $N=50$ below ^{78}Ni . The spectroscopy of $^{70,72}\text{Fe}$ performed by C. Louchart (TU Darmstadt, Germany) revealed the same trend then for Cr isotopes, with a maximum of deformation at $N=42$. The full data set and our shell-model interpretation suggests a large collectivity for neutron-rich Cr and Fe, possibly up to $N=50$, questioning the robustness of the $N=50$ shell closure below ^{78}Ni . The results of the Cr and Fe isotopes spectroscopy have been submitted recently in a joint article, shown in Appendix. Inclusive and exclusive knockout cross sections were also measured. The interpretation of exclusive cross sections for ^{66}Cr is still preliminary as only f orbitals were included in the theoretical considerations and the inclusion of other orbitals will be performed to compare with the experimental cross sections. The extraction of parallel momentum distributions has been tested for ^{68}Fe without success but other nuclei will be analyzed from the same physics experiment.

The analysis of ^{78}Ni is under development by R. Taniuchi (University of Tokyo, Japan) and should lead to complementary and very exciting results. To extend to more neutron-rich isotopes the study of the $N=40$ Island of Inversion and its possible merging towards $N=50$, the spectroscopy of ^{68}Cr and ^{74}Fe could be performed at the RIBF in a coming future when a factor ten upgrade of the primary ^{238}U beam intensity will be achieved.

The MINOS has been operational since May 2014 with the first SEASTAR campaign, and a second SEASTAR campaign took place in May 2015 as well as another experiment to study the di-neutron correlations in halo nuclei [44] in November 2014. In the coming years, the third and last SEASTAR campaign will take place with the spectroscopy of lighter nuclei such as ^{52}Ar and ^{62}Ti . The SEASTAR campaigns will provide a benchmark for $(p, 2p)$ and (p, pn) knockout cross sections. For in-beam γ -ray spectroscopy experiments at the RIBF, the limiting factor is the intrinsic resolution of the NaI(Tl) detectors. The MINOS TPC will provide high gain when used in combination with a high-resolution γ -ray detector array, such as the high-resolution Ge array AGATA at FAIR. The gain in luminosity with AGATA is compared to a standard ^9Be target and to DALI2 for ^{68}Fe in Fig. 6.10.

The concept of MINOS may lead to new developments and experimental techniques. The MINOS target surrounded by a large TPC could also be used inside a solenoid to perform missing mass spectroscopy experiments by measuring the total energy of recoiling protons by their bending in the magnetic field of the solenoid while their scattering angle is also determined from their tracks in the TPC. A device like MINOS that provides vertex tracking and a very thick target could be used to produce hypernuclei in inverse kinematic from NN collisions. With the use of a hydrogen target, exclusive measurements with low background will then be possible. The production vertex of strangeness and the decay of the λ hyperon could be tracked by a tracker surrounding the thick hydrogen target. In the near future, a quasifree scattering

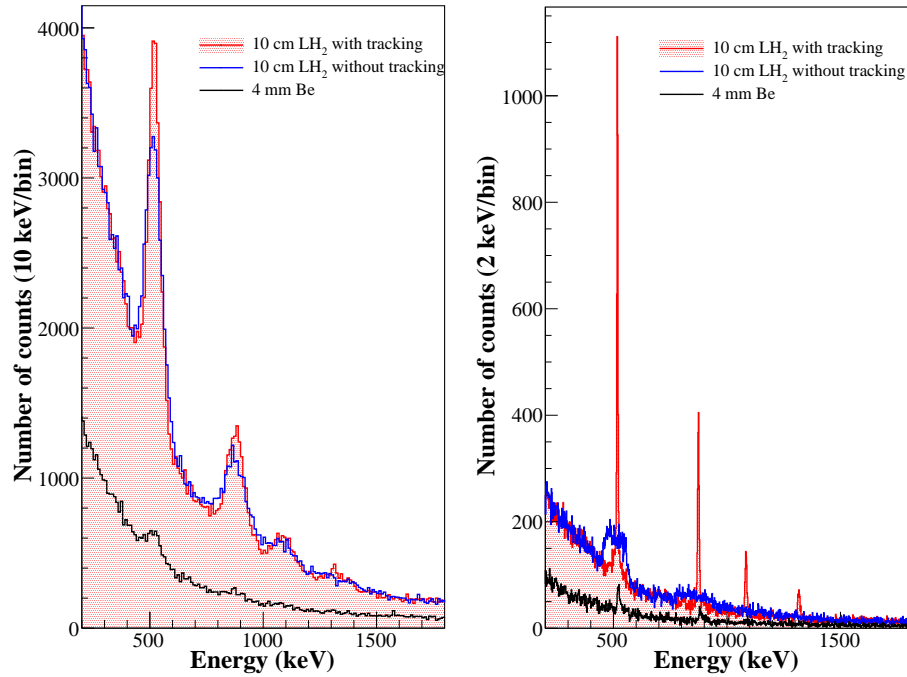


Fig. 6.10 – Simulations of transitions in ^{68}Fe with a standard ^9Be target in black, with a 10 cm LH_2 target without and with tracking from the MINOS TPC in blue and red respectively. On the left is represented the simulation for the DALI2 array and on the right for AGATA, for a 100 pps beam during 4.5 days. For the DALI2 simulation, the SEASTAR configuration is used with the individual detector resolutions from the experiment. For AGATA, the configuration of 5 triplets and 5 doublets of AGATA clusters is used, such as used at GSI (2013).

program at energies between 500 to 1000 MeV/nucleon will be undertaken at GSI/FAIR by the R3B collaboration. The proton tracking will be performed by a new highly segmented Si array and the total kinetic energy of the scattered protons will be determined with the CALIFA calorimeter [137]. Quasifree scattering from very exotic nuclei could also be performed by use of a thick liquid hydrogen target with similar design than the MINOS target.

Appendices

APPENDIX A

MINOS tracking algorithm characteristics

Energy threshold of the pads	$q_{min} \approx 9000 e^-$
Hough transform in 2D (binnings and intervals)	$\Delta\theta_{int/ext} = 2^\circ$ $\theta_{int/ext} \in [0^\circ, 360^\circ]$
Minimum number of points in track	$n_{min} = 10$
Condition C_{ring} in the 4 first rings of the TPC	$N_{pads} \geq 3$
Events with number of tracks considered in 3D	$0 < N_{track} < 5$
Hough transform in 3D (binnings and intervals)	$\Delta\rho_{xy/xz/yz} = 2^\circ$ $\Delta\rho_{xy/xz/yz} = 3 \text{ mm}$ $\rho_{xy} \in [-45 \text{ mm}, 45 \text{ mm}]$ $\rho_{xz/yz} \in [-300 \text{ mm}, 300 \text{ mm}]$ $\theta_{xy/xz/yz} \in [0^\circ, 180^\circ]$
Minimum number of rings touched (if not crossing the cathode)	$R_{min} = 15$

Tab. A.1 – Conditions applied in the present study for the tracking algorithm.

APPENDIX B

Beam line characteristics

Tab. B.1 – Characteristics of the *Zero Degree* Spectrometer settings.

Mode	Large acceptance achromatic	Medium resolution achromatic	Medium resolution dispersive	High resolution dispersive
Angular acceptance (mrad)	(H) 90 (V) 60	40 60	40 60	30 30
Momentum acceptance (%)	6	6	4	2
Momentum dispersion (mm/%)	-24.8 (F8-F9)	-21.2 (F8-F9)	40.6 (F8-F11)	62.9 (F8-F11)
Momentum resolution ($\Delta X = 1$ mm)	1240	2080	4070	6410
Maximum $B\rho$ (T.m)	8.1	9.7	9.8	10.2

Plane	Distance (mm)
F0	0
F1	10791
F2	22833
F3	31633
F4	43425
F5	54917
F6	66409
F7	78201
F8	89501
F9	102042
F10	113442
F11	125984

Tab. B.2 – Distance between the different focal planes in BigRIPS (F0-F8) and ZDS (F9-F11).

APPENDIX C

Electronics scheme

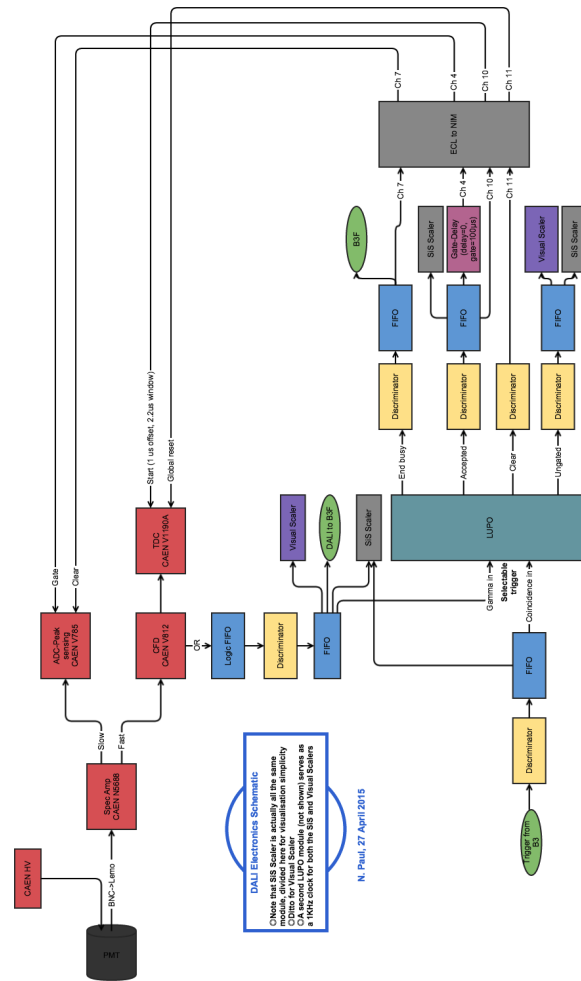


Fig. C.1 – Scheme of the DALI2 electronics.

APPENDIX D

Accepted article

Extension of the N=40 Island of Inversion towards N=50: Spectroscopy of ^{66}Cr , $^{70,72}\text{Fe}$

C. Santamaria,^{1,2} C. Louchart,³ A. Obertelli,^{1,2} V. Werner,^{3,4} P. Doornenbal,² F. Nowacki,⁵ G. Authelet,¹ H. Baba,² D. Calvet,¹ F. Château,¹ A. Corsi,¹ A. Delbart,¹ J.-M. Gheller,¹ A. Gillibert,¹ T. Isobe,² V. Lapoux,¹ M. Matsushita,⁶ S. Momiyama,^{2,7} T. Motobayashi,² M. Niikura,⁷ H. Otsu,² C. Péron,¹ A. Peyraud,¹ E. C. Pollacco,¹ J.-Y. Roussé,¹ H. Sakurai,^{2,7} M. Sasano,² Y. Shiga,^{2,8} S. Takeuchi,² R. Taniuchi,^{2,7} T. Uesaka,² H. Wang,² K. Yoneda,² F. Browne,⁹ L.X. Chung,¹⁰ Zs. Dombradi,¹¹ S. Franchoo,¹² F. Giacoppo,¹³ A. Gottardo,¹² K. Hadynska-Klek,¹³ Z. Korkulu,¹¹ S. Koyama,^{2,7} Y. Kubota,^{2,6} J. Lee,¹⁴ M. Lettmann,³ R. Lozeva,⁵ K. Matsui,^{2,7} T. Miyazaki,^{2,7} S. Nishinura,² L. Olivier,¹² S. Ota,⁶ Z. Patel,¹⁵ N. Pietralla,³ E. Sahin,¹³ C. Shand,¹⁵ P.-A. Söderström,² I. Stefan,¹² D. Steppenbeck,⁶ T. Sumikama,¹⁶ D. Suzuki,¹² Zs. Vajta,¹¹ J. Wu,^{2,17} and Z. Xu¹⁴

¹CEA, Centre de Saclay, IRFU, F-91191 Gif-sur-Yvette, France

²RIKEN Nishina Center, 2-1 Hirosawa, Wako, Saitama 351-0198, Japan

³Institut für Kernphysik, Technische Universität Darmstadt, 64289 Darmstadt, Germany

⁴WNSL, Yale University, P.O. Box 208120, New Haven, CT06520, USA

⁵IPHC, CNRS/IN2P3, Université de Strasbourg, F-67037 Strasbourg, France

⁶Center for Nuclear Study, University of Tokyo, RIKEN campus, Wako, Saitama 351-0198, Japan

⁷Department of Physics, University of Tokyo, 7-3-1 Hongo, Bunkyo, Tokyo 113-0033, Japan

⁸Department of Physics, Rikkyo University, 3-34-1 Nishi-Ikebukuro, Toshima, Tokyo 172-8501, Japan

⁹School of Computing Engineering and Mathematics, University of Brighton, Brighton BN2 4GJ, United Kingdom

¹⁰Institute for Nuclear Science & Technology, VAEI, 179 Hoang Quoc Viet, Cau Giay, Hanoi, Vietnam

¹¹MTA Atomki, P.O. Box 51, Debrecen H-4001, Hungary

¹²Insitut de Physique Nucléaire Orsay, IN2P3-CNRS, 91406 Orsay Cedex, France

¹³Department of Physics, University of Oslo, N-0316 Oslo, Norway

¹⁴Department of Physics, The University of Hong Kong, Pokfulam, Hong Kong

¹⁵Department of Physics, University of Surrey, Guildford GU2 7XH, United Kingdom

¹⁶Department of Physics, Tohoku University, Sendai 980-8578, Japan

¹⁷State Key Laboratory of Nuclear Physics and Technology, Peking University, Beijing 100871, P.R. China

We report on the measurement of the first 2^+ and 4^+ states of ^{66}Cr and $^{70,72}\text{Fe}$ via in-beam γ -ray spectroscopy. The nuclei of interest were produced by $(p,2p)$ reactions at incident energies of 260 MeV/nucleon. The experiment was performed at the Radioactive Isotope Beam Factory, RIKEN using the DALI2 γ -ray detector array and the novel MINOS device, a thick liquid hydrogen target combined with a vertex tracker. A low-energy plateau of 2^+ and 4^+ energies as a function of neutron number was observed for $N \geq 38$ and $N \geq 40$ for even-even Cr and Fe isotopes, respectively. State-of-the-art shell model calculations with a modified LNPS interaction in the $pf_{9/2}d_{5/2}$ valence space reproduce the observations. Interpretation within the shell model shows an extension of the Island of Inversion at $N=40$ for more neutron-rich isotopes towards $N=50$.

PACS numbers: 21.10.Re, 21.60.Cs

Atomic nuclei are the place of a complex interplay between single-particle configurations and correlations which strongly determine their quantum coherent wavefunctions. All over the nuclear chart, the so-called *magic* numbers of nucleons define boundaries of large areas of deformation. This picture, mainly established for stable nuclei and neighbors, is re-examined at the light of new available nuclei with an unbalanced proton-to-neutron ratio, with the underlying question of the persistence or evolution of magic numbers [1, 2]. Specific terms of the nuclear interaction can induce the formation of shell gaps or the lowering of relative orbital energies which, combined with correlations, sometimes lead to energetically favored intruder states as the ground state configuration [3–8]. Regions where two-particle two-hole ($2p2h$) configurations are favored over normally-filled orbitals by quadrupole correlations have been termed as *Islands of Inversion* (IoI) [9–11]. The $N=20$ IoI in

the vicinity of ^{32}Mg has provided unique information on shell evolution [12]. This IoI does not show any decrease in collectivity for Mg isotopes at $N > 24$ and merges with the $N=28$ deformation region [8, 13]. For Fe and Cr isotopes at $N=40$, a similar IoI has been claimed [14] while ^{68}Ni shows a marked pf neutron shell closure with a high excitation energy of the 2^+ state [15] and small $B(E2; 0^+ \rightarrow 2^+)$ ($B(E2)^\dagger$) value [16]. On the other hand, mass measurements show that the $N=40$ gap is weak for ^{68}Ni [17, 18] and it has been proposed that the low $B(E2)^\dagger$ value in ^{68}Ni may not be due to a $N=40$ shell closure but might come from a neutron-dominated excitation [19]. The removal of only two protons from the $f_{7/2}$ orbital has a drastic effect on the collectivity in Fe isotopes and changes the energy of the 2^+ state from 2033 keV in ^{68}Ni to 573 keV and 517 keV in ^{66}Fe and ^{68}Fe , respectively [20, 21]. A similar behavior is observed in the Cr isotopes, where

the 2_1^+ energies decrease gradually beyond $N=32$ [22, 23] with the lowest 2_1^+ energy measured in this mass region at 420(7) keV for ^{64}Cr [24]. This sudden onset of deformation along the Fe and Cr chains has also been inferred from $B(E2)\uparrow$ systematics [14, 25, 26]. Those first observables demonstrate an increase of collectivity for both Cr and Fe isotopes as a function of neutron number beyond $N=38$, which is also supported by mass measurements [27]. This is well reproduced within the shell model with a $pf g_{9/2} d_{5/2}$ valence space for neutrons and pf valence space for protons outside a ^{48}Ca core [28]. Significant neutron excitations above the $1g_{9/2}$ orbital to its quadrupole partner $2d_{5/2}$ have been shown to play a major role in this effect. Beyond-mean field calculations based on a collective Hamiltonian lead to similar predictions [29, 30]. The scarce experimental data available on Cr and Fe isotopes beyond $N=40$ indicate that no maximum of collectivity has been reached. Whether the structural evolution of the heavier isotopes mimics the merging found for Mg isotopes depends on the persistence of the $N=50$ shell closure below ^{78}Ni [31]. In this Letter, we present the first spectroscopy of ^{66}Cr and $^{70,72}\text{Fe}$ and characterize the evolution of collectivity inside the $N=40$ IoI towards $N=50$.

The experiment was performed at the Radioactive Isotope Beam Factory (RIBF), operated jointly by the RIKEN Nishina Center and the Center for Nuclear Study of the University of Tokyo. A ^{238}U beam was accelerated to 345 MeV/nucleon and impinged on a 3-mm thick ^9Be primary target at the entrance of the BigRIPS separator [32] with a mean intensity of 12 pnA. The secondary beam was selected by the $B\rho\text{-}\Delta E\text{-}B\rho$ method with 8-mm and 2-mm thick aluminum wedges at two dispersive planes. Two beam settings were tuned for ^{67}Mn and $^{71,73}\text{Co}$, respectively. Fully-stripped secondary ions were identified on an event-by-event basis. The particle identification of the incoming cocktail beam at the entrance of the secondary target and the identification of secondary residues were performed from $B\rho$ reconstruction, time of flight, and ionization-chamber energy loss measurements in the BigRIPS and ZeroDegree (ZDS) spectrometers [33]. The incident energies at the entrance (exit) of the secondary target were ~ 260 (~ 200) MeV/nucleon for ^{67}Mn and $^{71,73}\text{Co}$. Their intensities were measured to be 12 s^{-1} , 45 s^{-1} , and 6 s^{-1} , respectively. The total beam intensity on target for each of the two settings was about 6 kHz. This experiment was the first performed with the SEASTAR [34] setup composed of the DALI2 high-efficiency gamma spectrometer [35] and the new MINOS device integrating a liquid hydrogen target and a Time Projection Chamber (TPC) as a vertex tracker [36] (see Fig. 1). The SEASTAR setup ensured a gain in luminosity of 3.5 compared to the use of a solid Be target with the same energy loss. The vertex tracker

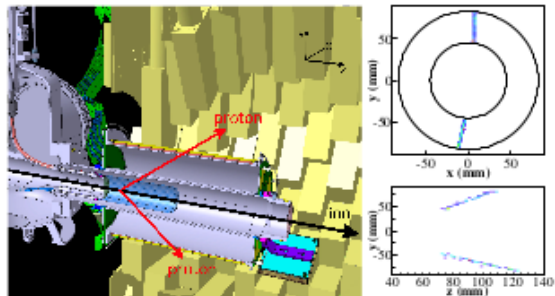


FIG. 1: (Color online) (Left) Drawing of the setup. The MINOS TPC (grey) and target (blue) are surrounded by the DALI2 array (yellow) in a compact geometry. (Right) A typical $^{67}\text{Mn}(p, 2p)^{66}\text{Cr}$ event measured with MINOS. The induced charges produced by ionization electrons were collected on the Micromegas detector in the xy transverse plane (top) whereas the directions of the tracks along the z axis were obtained from the drift time (bottom).

(i) improved the Doppler correction for the decay of short lived states by minimizing target effects and (ii) selected only the reaction events that occurred inside the target. The target cell was 102(1) mm long and filled with pure liquid hydrogen at 20 K, leading to an effective target thickness of 735(8) mg/cm². The entrance and exit target windows added up to 275 μm of Mylar. Beam particles were tracked with two position-sensitive parallel-plate avalanche counters [37] upstream of the target. Secondary residues were mostly produced from hydrogen-induced $(p, 2p)$ knockout reactions. MINOS measured the emitted proton trajectories, from which the vertex was reconstructed. As an example, a typical $(p, 2p)$ event is shown in the right panel of Fig. 1. Events with one or two protons were detected and reconstructed with a 95% efficiency and a vertex position resolution along the beam axis better than 5 mm Full Width at Half Maximum (FWHM) [38]. The 300-mm long cylindrical TPC was flushed with a gas mixture of Ar (82%), isoC₄H₁₀(3%) and CF₄ (15%) at room temperature and atmospheric pressure. The electron drift velocity was measured to be 4.5 cm/ μs , for a 180 V/cm homogeneous electrical potential, in agreement with simulations. Ionization electrons from tracks of charged particles through the TPC volume were amplified by a bulk Micromegas [39] plane composed of 3604 constant-area pads divided into 18 rings. The longitudinal direction of the tracks was determined from the electron drift time measured with new custom-made readout electronics [40]. This work was the first sizable experiment using AGET chips [41], a key component to handle a trigger of several hundred Hz. The DALI2 array was composed of 186 NaI scintillator detectors with an energy threshold of ~ 200 keV and covering angles from 7 to 115 degrees

(integrated along the target length) relative to the beam axis in a close geometry around the MINOS device as illustrated in Fig. 1. Energy calibrations were performed with ^{88}Y , ^{137}Cs , and ^{60}Co gamma sources giving a 2.9 % sigma energy resolution for a 1333 keV γ -ray transition. The setup was estimated to have a 32 % (20 %) full-energy photopeak detection efficiency for a 500 keV (1 MeV) transition emitted in-flight at 250 MeV/nucleon without addback. The Doppler correction of γ -ray transitions emitted in-flight was performed by taking into account the reaction vertex and the projectile velocity, reconstructed from MINOS. The procedure was validated on known short-lived cases. Addback was performed for γ -ray energies greater than 200 keV when the center of hit detectors were less than 15 cm apart.

The Doppler-corrected γ -ray spectra for ^{66}Cr , and $^{70,72}\text{Fe}$ are shown in Fig. 2. Two transitions are visible for all three nuclei. In the case of ^{66}Cr the transition energies were found at 386(10) keV and 683(9) keV, for ^{70}Fe at 480(13) keV and 866(10) keV, and for ^{72}Fe at 520(16) keV and 814(12) keV. Due to limited statistics, no other transition was observed. Gamma-gamma coincidences are illustrated in the insets of Fig. 2. From relative intensities and from the systematics along the Fe and Cr chains, the first two γ -ray lines were assigned to the $2_1^+ \rightarrow 0_1^+$ and $4_1^+ \rightarrow 2_1^+$ transitions. Note that one proton knockout reactions from the fp shells can naturally lead to $J=4$ states, and that the relative intensities of the first 2^+ and 4^+ states populated from $(p, 2p)$ and $(p, 3p)$ are similar for the three studied nuclei, as well as for the cases of ^{68}Fe and ^{74}Ni for which the $4^+ \rightarrow 2^+$ transitions are unambiguously assigned in the literature. Absolute cross sections will be discussed elsewhere. These energy values were obtained from a fit containing the simulated response of DALI2 [42] and background consisting of two exponentials. The experimental intrinsic resolution of each crystal was considered in the simulations. The summed simulated spectra are shown with the experimental data in Fig. 2, as well as the simulated responses for individual transitions. The half-lives of the γ -ray emitting states affect the peak positions after applying the Doppler correction. In the case of a 386/480/520 keV transition, simulations yield an offset of 8/11/13 keV for a 50 ps half-life. In the simulations, we considered the half-life of 2_1^+ states to be 50 ps for ^{66}Cr and $^{70,72}\text{Fe}$, in agreement with known half-lives in this mass region and with the measured widths of the transitions. The uncertainty on this half-life was considered of ± 50 ps for all the nuclei and was included in the energy uncertainties for the $2_1^+ \rightarrow 0_1^+$ transition. 4_1^+ states were considered short-lived ($\tau_{1/2} < 10$ ps). These half-life uncertainties, dominating the 2_1^+ energy ones, were added quadratically to statistical and energy calibration (5 keV) uncertainties.

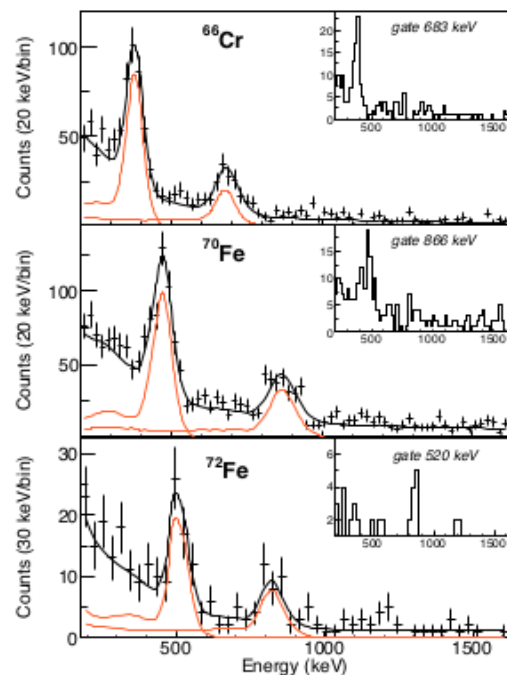


FIG. 2: (Color online) Doppler-corrected γ -ray spectra of ^{66}Cr , ^{70}Fe , and ^{72}Fe , populated from $(p, 2p)$ and $(p, 3p)$ reactions: data, simulated responses for all transitions (orange), and sum of the simulated transitions with a two-exponential background (black). Multiplicities below five are shown. (Insets) Gamma-gamma coincidence spectra.

The systematics of 2_1^+ energies and the ratio $R_{4/2} = E(4_1^+)/E(2_1^+)$ of even-even nuclei belong to the first observables that can be measured with rare isotopes and provide information on their collectivity. The evolution of 2_1^+ and 4_1^+ states is presented in Fig. 3. At first glance, the measured 2_1^+ , 4_1^+ energies reveal a rather flat behavior from $N=38$ to $N=42$ for Cr isotopes and from $N=40$ to $N=46$ for Fe isotopes, suggesting that the bulk deformation properties of these isotopes do not evolve much beyond $N=40$ and that ^{66}Cr and $^{70,72}\text{Fe}$ stay within the IoI. In a simple collective model, one expects the maximum of collectivity along an isotopic chain to lead to a minimum 2_1^+ energy and a $R_{4/2}$ ratio close to 3.3 in case of pure rotational states. In this framework, the picture obtained from this measurement is consistent. The Cr chain shows increasing collectivity towards ^{66}Cr with the lowest 2_1^+ energy measured in the region of ^{66}Cr while the $R_{4/2}$ ratio increases. The same picture is true for Fe isotopes from $N=40$, while a change is observed at $N=46$: both the 2_1^+ energy and the $R_{4/2}$ ratio consistently indicate a lessening of the collectivity from $N=44$. This change, occurring at

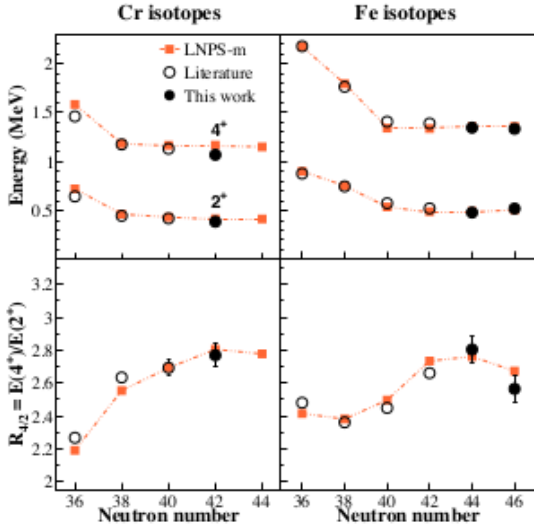


FIG. 3: (Color online) Systematics of $E(2_1^+)$ and $E(4_1^+)$ energies and $R_{4/2} = E(4_1^+) / E(2_1^+)$ for Cr and Fe isotopes. Experimental energies from Refs. [21, 24, 43] and from the present work are compared to large-scale shell model calculations. Most error bars are too small to be seen.

the $g_{9/2}$ *mid-shell*, is observed for the first time in the $N=40$ Island of Inversion. Although this behavior would be typical for an isolated $g_{9/2}$ single shell, the actual situation turns out to be more subtle.

To further quantify the collectivity in neutron-rich Cr and Fe isotopes beyond $N=40$, shell model calculations were carried out in the valence space that successfully described the new IoI at $N=40$ [28]. This valence space was composed of the pf proton orbitals and $p_{1/2}$, $f_{5/2}$, $g_{9/2}$, and $d_{5/2}$ neutron orbitals. The effective Hamiltonian used in this work, called LNPS-m, was based on the LNPS Hamiltonian from Ref. [28]. Minor modifications to the LNPS interaction were applied on the monopole and pairing parts of the effective Hamiltonian to describe a broader region [44–46]. In addition, LNPS calculations underpredict the 2_1^+ excitation energies of the most neutron rich Cr and Fe isotopes, which was interpreted as missing intruder configurations in their ground state. This mechanism is cured and validated by introducing 150 keV additional gd - gd monopole strength in the present LNPS-m interaction. The physics at $N=40$ remains unchanged with respect to the LNPS Hamiltonian (see for example occupancies and wavefunction decomposition for ^{64}Cr in Table I and Table II of Ref. [28]) but the root mean square for all the states in Fig. 3 amounts to 49 keV with the present LNPS-m Hamiltonian against 89 keV with the original LNPS. More detailed results with the LNPS-m interaction will be discussed elsewhere. The need and

TABLE I: Quadrupole deformation properties of Cr and Fe isotopes. Energies are in MeV, $B(E2) \downarrow$ in $e^2 \text{fm}^4$, and Q in $e \text{fm}^2$. Experimental energies are the same as Fig. 3.

	^{62}Cr	^{64}Cr	^{66}Cr	^{68}Cr	^{66}Fe	^{68}Fe	^{70}Fe	^{72}Fe
$E^*(2_1^+)$ exp.	0.44	0.42	0.39	-	0.57	0.52	0.48	0.52
$E^*(2_1^+)$ theo.	0.46	0.43	0.42	0.41	0.54	0.49	0.49	0.51
Q_{spec}	-38	-38	-39	-38	-37	-40	-39	-33
$B(E2) \downarrow$ th.	378	388	389	367	372	400	382	279
Q_{int} from Q_{spec}	135	136	137	132	131	140	135	116
Q_{int} from $B(E2)$	138	140	140	136	137	142	139	118
$\langle \beta \rangle$	0.33	0.33	0.32	0.30	0.29	0.30	0.28	0.24
$E^*(4_1^+)$ exp.	1.17	1.13	1.07	-	1.41	1.39	1.35	1.33
$E^*(4_1^+)$ theo.	1.18	1.13	1.06	1.15	1.34	1.34	1.36	1.36
Q_{spec}	-49	-49	-46	-47	-47	-51	-48	-40
$B(E2) \downarrow$ th.	562	534	562	530	553	608	574	377
Q_{int} from Q_{spec}	135	134	134	130	129	141	132	111
Q_{int} from $B(E2)$	141	140	141	137	139	146	142	115
$\langle \beta \rangle$	0.34	0.33	0.32	0.31	0.29	0.30	0.29	0.23

impact of this extra term are discussed hereafter. The overall 2_1^+ , 4_1^+ systematics and observed plateaus are reproduced by the calculations. The collectivity of these nuclei can be estimated using the rotational limit where a connection between the laboratory and intrinsic frames is established using relations (1) and (2) of Ref. [28]. The quadrupole properties of these nuclei are summarized in Table I. The calculated $B(E2) \downarrow$ values, quadrupole moments and deformations are consistent with a first-order description of the studied isotopes as prolate deformed rotational nuclei. An interesting feature for the studied nuclei is that the intrinsic wave functions for the ground, 2_1^+ and 4_1^+ states for all studied nuclei are shown to be similar with a relative variation of neutron occupancy $n^\nu(g_{9/2} + d_{5/2})$ of less than 3 % along the band states. In the Cr chain, the calculations show that the deformation is nearly constant with a maximum achieved at $N=40$ where the quadrupole collectivity translates into the development of an intrinsic shape of deformation $\beta \sim 0.33$. This feature is reflected by almost constant 2_1^+ and 4_1^+ excitation energies. Nevertheless, inspection of the wave function content in Table II shows varying particle-hole excitations as a function of the neutron number, and a maximum at $N=40$ with sizable $6p6h$ excitations admixtures. Similar conclusions can be drawn for Fe isotopes and details on their wave functions can be obtained from calculations performed with the original LNPS interaction in Ref. [14, 28]. To understand the flat behavior of 2_1^+ excitation energies in the Cr and Fe chains, we extracted the pairing expectation value of the multipole Hamiltonian for both the ground and first excited states. Our study indicates a delicate interplay between quadrupole and pairing correlations. For example ^{66}Cr and ^{70}Fe show

TABLE II: Occupation number n^ν of neutron intruder orbitals from the shell-model calculations (SM) of this work compared to the independent particle model (IPM). The percentage of particle-hole excitations across the N=40 gap in the ground state of Cr isotopes is also given. The last column features the pairing correlations energy differences $\Delta E_{Pairing}^*$ (in MeV) evaluated between the ground state and the 2_1^+ state.

Nucleus	$n^\nu(g_{3/2} + d_{5/2})$		0p0h	2p2h	4p4h	6p6h	$\Delta E_{Pairing}^*$
	IPM	SM					
^{60}Cr	0	1.8	14	75	7	0	1.84
^{62}Cr	0	3.5	1	25	71	3	1.49
^{64}Cr	0	4.3	0	8	71	20	1.25
^{66}Cr	2	5.2	0	40	56	3	1.13
^{68}Cr	4	6.0	6	79	11	0	1.24

the smallest 2_1^+ excitation energy of their respective isotopic chain as a consequence of a smaller pairing correlations difference between the ground-state and the 2_1^+ . Our work also demonstrates that intruder states are very sensitive to the gd-gd monopole strength in the considered nuclei.

In summary, we measured the 2_1^+ and 4_1^+ states in neutron-rich ^{66}Cr and $^{70,72}\text{Fe}$ isotopes. A plateau in the energy systematics was observed for Cr and Fe isotopes beyond N=38,40 and up to N=44,46, respectively. This plateau is interpreted within the shell model as an extension of the N=40 IoI towards more neutron-rich isotopes. While quadrupole collectivity is maximized at N=40, the evolution of pairing correlations slightly shifts the minimum of 2_1^+ and 4_1^+ energies to larger neutron number for both Cr and Fe isotopes. Whether this plateau extends to N=50, which would imply the disappearance of the N=50 shell closure below ^{78}Ni , requires the spectroscopy of more neutron-rich Fe and Cr isotopes. While the spectroscopy of ^{68}Cr and ^{74}Fe could be reached at SEASTAR in the near-term future with improvements of U primary beam intensity at the RIBF, the spectroscopy of more exotic isotopes should await for major upgrades or next-generation facilities.

The authors are thankful to the RIBF and BigRIPS teams for the stable operation, high intensity of the Uranium primary beam and production of secondary beams during the experiment. The development of MINOS and the core MINOS team have been supported by the European Research Council through the ERC Grant MINOS-258567. A. O. has been supported by the JSPS long-term fellowship L-13520 from Sept. 2013 to June 2014 at the RIKEN Nishina Center. A. O. deeply thanks the ERC and JSPS for their support. C. Santamaria and A. O. are grateful to the RIKEN Nishina Center for its hospitality. L.X. C. has been supported by the LIA program of Viet-

nam Ministry of Science and Technology (MOST). Z. D. and Zs. V. have been supported by the OTKA K100835 contract. V. W. further acknowledges support through the German BMBF grant 05P12RDFN8 and U.S. DOE under grant DE-FG02-91ER-40609. We thank N. Paul for her careful reading of the manuscript.

- [1] O Sorlin and M.-G. Porquet, Prog. in Part. and Nucl. Phys. **61**, 602 (2008).
- [2] E. Caurier *et al.*, Rev. Mod. Phys. **77**, 427 (2005).
- [3] I. Talmi and I. Unna, Phys. Rev. Lett. **4**, 469 (1960).
- [4] T. Otsuka *et al.*, Phys. Rev. Lett. **87**, 082502 (2001).
- [5] T. Otsuka *et al.*, Phys. Rev. Lett. **95**, 232502 (2005).
- [6] N. Smirnova *et al.*, Phys. Lett. B **686**, 109 (2010).
- [7] N. Smirnova *et al.*, Phys. Rev. C **86**, 034314 (2012).
- [8] E. Caurier, F. Nowacki, A. Poves, Phys. Rev. C **90**, 014302 (2014).
- [9] B. H. Wildenthal and W. Chung, Phys. Rev. C **22**, 2260 (1980).
- [10] A. Poves and J. Retamosa, Phys. Lett. B **184**, 311 (1987).
- [11] E. K. Warburton, J. A. Becker and B. A. Brown, Phys. Rev. C **41**, 1147 (1990).
- [12] T. Motobayashi *et al.*, Phys. Lett. B **346**, 9 (1995).
- [13] P. Doornenbal *et al.*, Phys. Rev. Lett. **111**, 212502 (2013).
- [14] J. Ljungvall *et al.*, Phys. Rev. C **81**, 061301 (2010).
- [15] R. Broda *et al.*, Phys. Rev. Lett. **74**, 868 (1995).
- [16] O. Sorlin *et al.*, Phys. Rev. Lett. **88**, 092501 (2002).
- [17] C. Guénaut *et al.*, Phys. Rev. C **75**, 044303 (2007).
- [18] S. Rahaman *et al.*, Eur. Phys. J. A **34**, 5 (2007).
- [19] K. Langanke *et al.*, Phys. Rev. C **67**, 044314 (2003).
- [20] M. Hannawald *et al.*, Phys. Rev. Lett. **82**, 1391 (1999).
- [21] P. Adrich *et al.*, Phys. Rev. C **77**, 054306 (2008).
- [22] O. Sorlin *et al.*, Eur. Phys. J. A **16**, 55 (2003).
- [23] N. Aoi *et al.*, Phys. Rev. Lett. **102**, 012502 (2009).
- [24] A. Gade *et al.*, Phys. Rev. C **81**, 051304(R) (2010).
- [25] W. Rother *et al.*, Phys. Rev. Lett. **106**, 022502 (2011).
- [26] H. L. Crawford *et al.*, Phys. Rev. Lett. **110**, 242701 (2013).
- [27] S. Naimi *et al.*, Phys. Rev. C **86**, 014325 (2012).
- [28] S.M. Lenzi *et al.*, Phys. Rev. C **82**, 054301 (2010).
- [29] L. Gaudefroy *et al.*, Phys. Rev. C **80**, 064313 (2009).
- [30] K. Sato *et al.*, Phys. Rev. C **86**, 024316 (2012).
- [31] I. Hamamoto, Phys. Rev. C **85**, 064329 (2012).
- [32] T. Kubo *et al.*, Prog. Theor. Exp. Phys. **2012**, 3C003 (2012).
- [33] N. Fukuda *et al.*, Nucl. Instr. Meth. B **317**, 323 (2013).
- [34] RIKEN Proposal for Scientific Program (2013). Acronym for Shell Evolution And Search for Two-plus states At the RIBF (SEASTAR).
- [35] S. Takeuchi *et al.*, Nucl. Instr. Meth. A **763**, 596 (2014).
- [36] A. Obertelli *et al.*, Eur. Phys. J. A **50**, 8 (2014).
- [37] H. Kumagai *et al.*, Nucl. Instr. Meth. A **470**, 562 (2001).
- [38] C. Santamaria *et al.*, to be published (2015).
- [39] I. Giomataris *et al.*, Nucl. Instr. Meth. A **376**, 29 (1996).
- [40] D. Calvet, IEEE Trans. Nucl. Sci., **61**, 1, 675-682 (2014).
- [41] S. Anvar *et al.*, Proc. IEEE Nuclear Science Symp., pp. 745-749 (2011).
- [42] S. Agostinelli *et al.*, Nucl. Instr. Meth. A **506**, 250 (2003).
- [43] S.N. Liddick *et al.*, Phys. Rev. C **87**, 014325 (2013).

-
- [44] F. Recchia *et al.*, Phys. Rev. C **88**, 041302(R) (2013).
[45] A. Gade *et al.*, Phys. Rev. Lett. **112**, 112503 (2014).
[46] F. Flavigny *et al.*, Phys. Rev. C **91**, 034310 (2015).

BIBLIOGRAPHY

- [1] W. Elsasser, *J. de Phys. et Rad.* **5** (1934) 625.
- [2] M. Goeppert-Mayer, *Phys. Rev.* **74** (1948) 235.
- [3] M. Goeppert-Mayer, *Phys. Rev.* **75** (1949) 1969.
- [4] O. Haxel, J. Jensen and H. Suess, *Phys. Rev.* **75** (1949) 1766.
- [5] C. Détraz *et al.*, *Phys. Rev. C* **19** (1979) 164.
- [6] D. Guillemaud-Mueller *et al.*, *Nucl. Phys. A* **426** (1984) 37.
- [7] P. Doornenbal *et al.*, *Phys. Rev. Lett.* **103** (2009) 032501.
- [8] A. Gade *et al.*, *Phys. Rev. C* **74** (2006) 021302(R).
- [9] D. Steppenbeck *et al.*, *Nature* **502** (2013) 207–210.
- [10] B. Bastin *et al.*, *Phys. Rev. Lett.* **99** (2007) 022503.
- [11] S. Takeuchi *et al.*, *Phys. Rev. Lett.* **109** (2012) 182501.
- [12] R. V. F. Janssens *et al.*, *Phys. Lett. B* **546** (2002) 55.
- [13] D.-C. Dinca *et al.*, *Phys. Rev. C* **71** (2005) 041302(R).
- [14] D. Steppenbeck *et al.*, *Phys. Rev. Lett.* **114** (2015) 252501.
- [15] J. Erler *et al.*, *Nature* **486** (2012) 509.
- [16] N. Ishii, S. Aoki and T. Hatsuda, *Phys. Rev. Lett.* **99** (2007) 022001.
- [17] P. Navrátil and B. R. Barrett, *Phys. Rev. C* **54** (1996) 2986.
- [18] R. Roth *et al.*, *Phys. Rev. Lett.* **107** (2011) 072501.
- [19] P. Ring and P. Schuck, *The Nuclear Many-Body Problem*, (2004).
- [20] T. H. R. Skyrme, *Nucl. Phys. A* **9** (1959a) 615.
- [21] T. H. R. Skyrme, *Nucl. Phys. A* **9** (1959b) 635.
- [22] J. Dechargé and D. Gogny, *Phys. Rev. C* **21** (1980) 1568.

- [23] J. G. Valatin, Nucl. Phys. A **92** (1967) 608.
- [24] D. L. Hill and J. A. Wheeler, Phys. Rev. **89** (1953) 1102.
- [25] M. Bender, P.-H. Heenen and P.-G. Reinhard, Rev. Mod. Phys. **75** (2003) 121.
- [26] K. Kumar and M. Baranger, Phys. Rev. **122** (1961) 1012.
- [27] J. Libert, M. Girod and J.-P. Delaroche, Phys. Rev. C **60** (1999) 054301.
- [28] G. R. Satchler, *Direct Nuclear Reactions*, (Oxford University Press, 1983).
- [29] T. Aumann *et al.*, Phys. Rev. Lett. **84** (2000) 35.
- [30] E. Sauvan *et al.*, Phys. Lett. B **491** (2000) 1–7.
- [31] F. Flavigny *et al.*, Phys. Rev. Lett. **108** (2012) 252501.
- [32] F. Flavigny *et al.*, Phys. Rev. Lett. **110** (2013) 122503.
- [33] A. Obertelli and T. Uesaka, Eur. Phys. J A **47** (2011) 105.
- [34] N. Chant and P. Roos, Phys. Rev. C **27** (1983) 1060.
- [35] K. Ogata, K. Yoshida and K. Minomo, Phys. Rev. C **92** (2015) 034616.
- [36] R. Crespo, A. Deltuva and E. Cravo, Phys. Rev. C **90** (2014) 044606.
- [37] T. Aumann, C. Bertulani and J. Ryckebusch, Phys. Rev. C **88** (2013) 064610.
- [38] Y. Yano *et al.*, Nucl. Instr. Meth. B **216** (2007) 1009–1013.
- [39] P. Doornenbal and A. Obertelli, NP1312-RIBF118, RIKEN Proposal for Scientific Program: SEASTAR (Shell Evolution and Search for Two-plus energies At the RIBF).
- [40] <http://www.nishina.riken.jp/collaboration/SUNFLOWER/experiment/seastar/index.html>.
- [41] A. Obertelli *et al.*, Eur. Phys. J A **50** (2014) 8.
- [42] <http://minos.cea.fr>.
- [43] T. Furukawa *et al.*, Nucl. Instr. Meth. A **562** (2006) 1050–1053.
- [44] A. Corsi and Y. Kubota, NP1312-SAMURAI18R1, Two-Neutron Momentum Correlations in Borromean Nuclei.
- [45] Y. Kondo, NP1312-SAMURAI21, Spectroscopy of unbound oxygen isotopes II.
- [46] R. Klapisch *et al.*, Phys. Rev. Lett. **23** (1969) 652.
- [47] C. Thibault *et al.*, Phys. Rev. C **12** (1975) 644.

- [48] X. Campi *et al.*, Nucl. Phys. A **251** (1975) 193.
- [49] N. Orr *et al.*, Phys. Lett. B **258** (1991) 29.
- [50] K. Yoneda *et al.*, Phys. Lett. B **499** (2001) 233.
- [51] G. Neyens *et al.*, Phys. Rev. Lett. **94** (2005) 022501.
- [52] A. Gade *et al.*, Phys. Rev. Lett. **99** (2007) 072502.
- [53] Y. Yanagisawa *et al.*, Phys. Lett. B **566** (2003) 84.
- [54] J. Terry *et al.*, Phys. Lett. B **640** (2006) 86.
- [55] K. Wimmer *et al.*, Phys. Rev. Lett. **105** (2010) 252501.
- [56] O. Niedermaier *et al.*, Phys. Rev. Lett. **94** (2005) 172501.
- [57] T. Motobayashi *et al.*, Phys. Lett. B **346** (1995) 9.
- [58] H. Iwasaki *et al.*, Phys. Lett. B **620** (2005) 118.
- [59] V. Chisté *et al.*, Phys. Lett. B **514** (2001) 233.
- [60] B. H. Wildenthal and W. Chung, Phys. Rev. C **22** (1980) 2260.
- [61] A. Poves and J. Retamosa, Phys. Lett. B **184** (1987) 311.
- [62] E. K. Warburton, J. A. Becker and B. A. Brown, Phys. Rev. C **41** (1990) 1147.
- [63] P. Doornenbal *et al.*, Phys. Rev. Lett. **111** (2013) 212502.
- [64] P. Fallon *et al.*, NP1312-RIBF03R1, Spectroscopy of ^{40}Mg .
- [65] N. Iwasa *et al.*, Phys. Rev. C **67** (2003) 064315.
- [66] S. Péru, M. Girod and J. F. Berger, Eur. Phys. J. A **9** (2000) 35–47.
- [67] S. M. Lenzi *et al.*, Phys. Rev. C **82** (2010) 054301.
- [68] http://www-phynu.cea.fr/science_en_ligne/carte_potentiels_microscopiques/carte_potentiel_nucleaire.htm.
- [69] J.-P. Delaroche *et al.*, Phys. Rev. C **81** (2010) 014303.
- [70] M. Hannawald *et al.*, Phys. Rev. Lett. **82** (1999) 1391.
- [71] P. Adrich *et al.*, Phys. Rev. C **77** (2008) 054306.
- [72] J. Ljungvall *et al.*, Phys. Rev. C **81** (2010) 061301.
- [73] W. Rother *et al.*, Phys. Rev. Lett. **106** (2011) 022502.
- [74] H. L. Crawford *et al.*, Phys. Rev. Lett. **110** (2013) 242701.

- [75] S. Naimi *et al.*, Phys. Rev. C **86** (2012) 014325.
- [76] O. Sorlin *et al.*, Eur. Phys. J. A **16** (2003) 55.
- [77] N. Aoi *et al.*, Phys. Rev. Lett. **102** (2009) 012502.
- [78] A. Gade *et al.*, Phys. Rev. C **81** (2010) 051304(R).
- [79] T. Baugher *et al.*, Phys. Rev. C **86** (2012) 011305.
- [80] T. Baugher *et al.*, Erratum Phys. Rev. C **86** (2012) 049902.
- [81] L. Gaudefroy *et al.*, Phys. Rev. C **80** (2009) 064313.
- [82] K. Sato *et al.*, Phys. Rev. C **86** (2012) 024316.
- [83] R. Broda *et al.*, Phys. Rev. Lett. **74** (1995) 868.
- [84] O. Sorlin *et al.*, Phys. Rev. Lett. **88** (2002) 092501.
- [85] C. Guénaut *et al.*, Phys. Rev. C **75** (2007) 044303.
- [86] S. Rahaman *et al.*, Eur. Phys. J. A **34** (2007) 5.
- [87] K. Langanke *et al.*, Phys. Rev. C **67** (2003) 044314.
- [88] I. Hamamoto *et al.*, Phys. Rev. C **85** (2012) 064329.
- [89] C. Louchart *et al.*, Nucl. Instr. Meth. A **736** (2014) 81.
- [90] C. Louchart, *PhD IRFU-12-22-T*, (2012).
- [91] I. Giomataris *et al.*, Nucl. Instr. Meth. A **376** (1996) 29.
- [92] I. Giomataris *et al.*, Nucl. Instr. Meth. A **560** (2006) 405.
- [93] S. Takeuchi *et al.*, Nucl. Instr. Meth. A **763** (2014) 596.
- [94] L. Fabbietti *et al.*, Nucl. Instr. Meth. A **628** (2011) 204.
- [95] S. Biagi *et al.*, Nucl. Instr. Meth. A **241** (1999) 234.
- [96] S. Agostinelli *et al.*, Nucl. Instr. Meth. A **506** (2003) 250.
- [97] G. Charles, *PhD IRFU-13-08-T*, (2013).
- [98] D. Calvet, *A versatile readout system for small to medium scale gaseous and silicon detectors*, in IEEE Trans. Nucl. Sci. **61** (2014) 675–682.
- [99] N. Abgrall *et al.*, Nucl. Instr. Meth. A **637** (2011) 25.
- [100] S. Anvar, in IEEE Nuclear Science Symposium and Medical Imaging Conference (NSS/MIC) **736** (2011) 745–749.

- [101] S. Anvar, in IEEE Nuclear Science Symposium Conference Records (NSS 08) pp. 3558–3561.
- [102] A. Boudard *et al.*, Phys. Rev. C **66** (2002) 044615.
- [103] A. Boudard *et al.*, Phys. Rev. C **87** (2013) 014606.
- [104] H. Miya *et al.*, Nucl. Instr. Meth. B **317** (2013) 701.
- [105] C. Hoppner *et al.*, Nucl. Instr. Meth. A **620** (2010) 518.
- [106] S. Akkoyun *et al.*, Nucl. Instr. Meth. A **668** (2012) 26.
- [107] P. V. C. Hough, *Methods and means for recognizing complex patterns*, U.S. Patent 3.069.654 (December 1962) .
- [108] R. Duda and P. Hart, Commun. ACM **15** (1972) 11–15.
- [109] D. Ballard *et al.*, Pattern Recognition **13** (1981) 111–122.
- [110] <http://root.cern.ch/root/html/TMinuit.html>.
- [111] H. Imao *et al.*, Phys. Rev. ST Accel. Beams **15** (2012) 123501.
- [112] H. Hasebe *et al.*, Journal of Radioanalytical and Nuclear Chemistry **305** (2015) 825–829.
- [113] T. Kubo *et al.*, Nucl. Instr. Meth. B **204** (2003) 97–113.
- [114] T. Kubo *et al.*, Prog. Theor. Exp. Phys. p. 3C003.
- [115] K.-H. Schmidt *et al.*, Nucl. Instr. Meth. A **260** (1987) 287–303.
- [116] H. Kumagai *et al.*, Nucl. Instr. Meth. A **470** (2001) 562.
- [117] H. Kumagai *et al.*, Nucl. Instr. Meth. B **317** (2013) 717–727.
- [118] H. Baba *et al.*, Nucl. Instr. Meth. A **616** (2010) 65.
- [119] N. Fukuda *et al.*, Nucl. Instr. Meth. B **317** (2013) 323.
- [120] H. Bethe, Handb. Phys. **24** (1933) 273.
- [121] H. Bethe, Z. Phys. **76** (1932) 293.
- [122] K. Kimura *et al.*, Nucl. Instr. Meth. A **538** (2005) 608–614.
- [123] H. Blok *et al.*, Nucl. Instr. Meth. A **262** (1987) 291.
- [124] M. Berz *et al.*, Phys. Rev. C **47** (1993) 537.
- [125] D. Bazin *et al.*, Nucl. Instr. Meth. B **204** (2003) 629.
- [126] O. Tarasov and D. Bazin, Nucl. Instr. Meth. B **266** (2008) 4657–4664.

- [127] G. F. Knoll, *Radiation Detection and Measurement*, (Wiley, New York, 1979).
- [128] <http://www.nndc.bnl.gov>.
- [129] J.-M. Daugas *et al.*, Phys. Rev. C **83** (2011) 054312.
- [130] L. Audirac *et al.*, Phys. Rev. C **88** (2013) 041602(R).
- [131] K. Wimmer *et al.*, *in preparation*.
- [132] A. Bohr and B. R. Mottelson, *Nuclear Structure Vol. I and II*, (Advanced Book Program, 1969-1975).
- [133] L. M. Robledo and G. F. Bertsch, Phys. Rev. C **84** (2011) 054302.
- [134] M. Bender and P.-H. Heenen, J. Phys. G: Nucl. Part. Phys. **31** (2005) S1611–S1616.
- [135] F. Nowacki and A. Poves, *in preparation*.
- [136] E. Caurier, F. Nowacki and A. Poves, Phys. Rev. C **90** (2014) 014302.
- [137] H. Alvarez-Pol *et al.*, Nucl Instr. Meth. A **767** (2014) 453–466.

LIST OF FIGURES

1.1	Nuclear chart with number of neutrons on the abscissa and number of protons on the ordinate. The known first excited state energies for even-even nuclei are given in color. The highest values of first excited state energies coincide with magic numbers, indicated on the graph. Source: http://www.nndc.bnl.gov/nudat2/	2
1.2	Nuclear chart with number of neutrons on the abscissa and number of protons on the ordinate. The known ratio of second to first excited state energies for even-even nuclei are shown in color. The highest ratios are an indication of deformation. Source: http://www.nndc.bnl.gov/nudat2/	3
1.3	First 2_1^+ and second 4_1^+ excitation energies for even-even isotopes of Si and Mg and the ratio of second to first excited state R_{42} . The energies are constant from N=20 to N=26 for Mg isotopes whereas Si isotopes exhibit a higher excitation energy at N=20, confirming a shell gap for Si, with a sudden decrease of energies towards N=28 which shows an onset of collectivity for Si. The figure is taken from Ref. [7].	4
1.4	Shell structure of stable nuclei up to N or Z = 50, obtained by Goeppert-Mayer and Haxel <i>et al.</i> [3, 4].	5
1.5	$p_{ }$ distribution of the ^{10}Be fragments in the rest frame of the projectile from a ^9Be ($^{11}\text{Be}, ^{10}\text{Be} + \gamma$) X neutron removal reaction at 60 MeV/nucleon. Only the contribution leading to the ground state of ^{10}Be is shown. The curves are calculations assuming a knockout reaction from s, p, and d states. Figure taken from Aumann <i>et al.</i> [29].	7
1.6	Overview of the 16 new $E(2_1^+)$ and at least 5 new $E(4_1^+)$ measurements foreseen within the SEASTAR project.	8
1.7	Systematics of Cr and Fe isotopes compared to the shell model calculations using the LNPS interaction [67], and also to the Hartree-Fock-Bogoliubov + 5-dimension Collective Hamiltonian calculations using the Gogny D1S force [68, 69].	10
2.1	Principle scheme of the MINOS device.	13
2.2	(Left) Front view (from downstream) of the target during the filling phase. The liquid-gas interface of hydrogen is clearly visible. (Right) Front view of the target cell mounted on its aluminum support with the supply and exhaust tubes for hydrogen.	14
2.3	View of the MUSCADE control command during operation with the vacuum in the reaction chamber, target temperature and storage pressure values for control.	15

2.4	(Left) MINOS TPC with one side opened. The internal and external field cages are visible. (Right) Kapton foil field cage with the Copper strips and resistors in between.	17
2.5	Magboltz simulations of the electron drift velocity as a function of the drift electric field for the two gas admixtures (in black the Ar(82%)-iso(3%)-CF4(15%) gas admixture, and in grey the Ar(97%)-iso(3%) admixture) and for different oxygen and water impurity levels. Despite the small E_d dependence of the Ar(97%)-iso(3%) gas admixture, the Ar(82%)-iso(3%)-CF4(15%)gas was favored due to its high drift velocity at $E_d \sim 200$ V/cm.	17
2.6	Micromegas pad planes with (a) projective pad geometry and (b) constant pad geometry. The Micromegas mesh rectangular connection pad is also visible.	18
2.7	Sketch of the Micromegas principle.	19
2.8	Measured amplification gain of the bulk Micromegas detectors as a function of the mesh potential for two different gas admixtures.	20
2.9	Design schematic (left) and picture (right) of the external Micromegas tracker without its copper shell.	21
2.10	Design schematic of the DSSSD.	22
2.11	Picture of a FEC card equipped with AGET chips and read out by a Feminos card.	22
2.12	Scheme of the MINOS DAQ processes in a standalone operation.	24
2.13	(Left) MIMAC test chamber when opened with an ^{241}Am source fixed with the copper rings as the outer field cage. (Right) Prototype of Micromegas detector at the end of the TPC (seen at the rear of the MIMAC chamber on the left figure) with four different geometries of pads.	25
2.14	Reference axes for the α source test presented in Fig. 2.15 with z in the length of the TPC, and (x, y) a plane parallel to the detection and cathode planes in which the source is located (red disk). The references are transferred in spherical coordinates with (r, ϕ) the position of the source in the (x, y) plane and θ the incident angle of the α particles emitted from the source.	25
2.15	(Right) Incidence angle θ of the α source with respect to the angular position on the detection plane. (Left and Middle) Two dimensional and one dimensional reconstructions of the source position for incidence angles θ of the tracks larger than 25°	26
2.16	(Top Right) Sketch of the setup using a Si detector and an α source. (Top Left) Charge signals for an event. We distinguish two different tracks at two different times in the acquisition time, due to the large acquisition window of $10 \mu\text{s}$. The first signal (Bottom Left) corresponds to the α track in coincidence with the Si detector trigger, while the second signal (Bottom Right) is a random coincidence event.	26
2.17	Figure of a cosmic ray on the detection plane crossing two different Micromegas pad planes.	27
2.18	Articstic view of the CLAS12 cosmic bench composed of two plastic scintillators for trigger, large position sensitive Micromegas detectors interspersing the MINOS TPC. Cables and electronics are not drawn for clarity purposes.	28

2.19	On the cosmic ray test bench: (a) Distribution of deposited charge as a function of the z axis of the TPC for about 2000 events. (b) Typical signal collected on a pad. (c) Projection of a track on the (x, y) Micromegas detection plane. Background events above threshold have been left on purpose and can be seen at random positions on the pad plane. (d) 3D view of the event shown in 2D in panel (c).	29
2.20	On the cosmic ray test bench with a thin scintillator in the beam pipe: (Top) Position on the thin scintillator plane of the reconstructed cosmic tracks in the TPC, the position of the scintillator of 25 cm length is clearly visible inside the red rectangle. (Bottom) Position of the tracks along the TPC length for tracks passing in the thin scintillator (in the red rectangle). Courtesy of A. Corsi (CEA, France).	30
2.21	Difference in millimeters between the reconstructed vertex and the real vertex of the (p,2p) reaction along the beam direction for the simulation of (left) $^{53}\text{K}(p, 2p)$ ^{52}Ar and (right) $^{79}\text{Cu}(p, 2p)$ ^{78}Ni	32
3.1	(Left) MINOS TPC at the HIMAC facility. (Right) MINOS experimental scheme seen from above of the in-beam test at HIMAC, with the distances in mm.	34
3.2	Principle of the Hough transform. For three points in the track (from left to right) the Hough transform scans all the possible tracks passing through this point (several shown in different colors). These tracks are defined by the minimum distance ρ to the origin and the angle θ of this minimum distance to the origin axis, presented here on the left for the red track. On the bottom part is presented schematically the parametrization of the colored tracks with the Hough transform. In the end, we look at all the different couples in the Hough space and find a common couple (ρ_5, θ_5) which corresponds to the track crossing all the points (in red). We therefore find the physical track from which the points belong to.	35
3.3	Scheme of the overall tracking algorithm with details on the applied conditions in Tab. A.1.	37
3.4	View of the Hough transform parameterization used with our geometrical specifications. The parameterization relies on the crossing points of the tracks with the inner and outer disks defined by the angles θ_{int} and θ_{ext} from the x axis. One possible track (in red) crossing the point (x, y) (in purple) is shown. The range of possible angles θ_{int} and θ_{ext} for this specific hit pad (x, y) are shown in orange.	38
3.5	Two-dimensional Hough transform applied to a two-track event. From left to right is shown the hit pads before the filter, the curves in the Hough representation of the event, and finally the hit pads after filtering out the points in the new-found track.	39

3.6	3D Hough transformation showing the filtering of a track from a delta electron (circled in red on the top). From left to right is represented the three 2D Hough transformations in the (xy), (xz) and (yz) planes respectively. From top to bottom are shown the hit pads before the filter, the curves in the Hough space of the event (circled in purple are the maxima taken for the final track), and finally the hit pads after filtering.	40
3.7	(Left) Measured time in μs on the bottom axis and extracted distance z along the beam line in mm on the upper axis inside the TPC for ^{20}Ne run (350 MeV/u). The time and distance 0 correspond to the Micromegas plane. (Right) Deduced drift velocity in $\text{cm}/\mu\text{s}$ as a function of the electric field applied in the MINOS TPC for several runs during the HIMAC measurements. The experimental points are compared to Magboltz simulations (dotted line) with no impurities.	42
3.8	(Left) (Filled histogram) Vertex position along the beam axis z in mm for a run with a ^{20}Ne beam at 350 MeV/u of 20 min duration at 50000 pps and around 56 000 events with 4 tracks or less. The time and distance 0 is the position of the Micromegas plane, i.e. the beginning of the MINOS TPC. (Non-filled histogram) Results of a GEANT4 simulation performed with the same conditions on the experiment and the same software, normalized to the number of counts in the experiment. (Right) Same with a ^4He beam at 200 MeV/u of 62 min duration at 15000 pps and around 163 000 events with 4 tracks or less.	43
3.9	Angles (in degrees) of the charged particles emitted from the regions of the two CH_2 targets, on the left for the first target with $z_v=[5,50]$ mm and on the right for the second target with $z_v=[125,170]$ mm. The data points (in black) are extracted from a run with a ^{20}Ne beam at 350 MeV/u of 20 min duration at 50000 pps and compared to full-scale simulations (in blue).	43
3.10	Pad multiplicity as a function for the experiment (in blue) and for the simulation (in black) of the radius on the Micromegas plane on the upper left. Pad multiplicity for the first, eighth and eighteenth (last) ring as a function of the position along the beam axis on the upper right, lower left and lower right respectively. This is extracted for a run with a ^{20}Ne beam at 350 MeV/u of 20 min duration at 50000 pps and around 56 000 events with 4 tracks or less.	44
4.1	Scheme of the RIBF heavy-ion accelerator system in a constant energy mode of 345 MeV/nucleon.	47
4.2	Scheme of the RIBF experimental beam line.	48
4.3	PPAC horizontal positions in the F3, F7, F8, F11 achromatic and F5, F9 dispersive focal planes for the $^{67}\text{Mn}(p, 2p)^{66}\text{Cr}$ reaction channel.	50
4.4	Picture of the DALI2 gamma array. (Left) Half of the DALI2 crystals, seen from downstream, with the first layer crystals clearly visible. (Right) DALI2 crystals geometry shown from upstream. The last 11 th layer of crystals is shown in the background.	52
4.5	(Top) Layout of the new DALI2 layer of crystals for the SEASTAR experiments. (Middle) Layout of the detectors in the second to eleventh layers in the standard configuration. (Bottom) Layout of the last layer in the standard configuration.	53

LIST OF FIGURES

4.6	DALI2 GEANT4 simulated resolution (green) and photo-peak efficiency (red) at $\beta=0.6$ for the first SEASTAR campaign: target of 100 mm length and 5 mm vertex reconstruction resolution with Doppler-shift corrections and addback for hit detectors distant by less than 15 cm.	54
4.7	SEASTAR experimental scheme at F8 representing the distances between the F8 double PPACs, DALI2, MINOS and DSSSD in mm. The DALI2 structure start represented here corresponds to the edge of the first layer of detectors.	55
4.8	Result of a pedestal check performed at the beginning of a run for all the channels of the MINOS electronics. The ordinate corresponds to the ring of the TPC (the lower part is the inner ring of the TPC while the upper part corresponds to the outer ring of the TPC) and the abscissa to all the channels of each TPC ring. (Left) Mean pedestal value after equalization during the electronics configuration. (Right) Standard deviation σ , i.e. noise level, from the mean pedestal value. As this pedestal run is performed with the constant pad plane, there are less and less channels connected to an actual pad on the detector. These unconnected pads not connected to the ground are seen with a higher standard deviation value in orange or red.	56
5.1	(Bottom) BigRIPS PID. (Top) Projection in A/Q for Mn isotopes, i.e. $Z=25$. . .	61
5.2	(Left) ZeroDegree particle Identification plot on the top figure and F9X position with respect to A/Q on the lower figure before any corrections. (Right) ZeroDegree particle Identification plot on the top figure and F9X position with respect to A/Q on the lower figure after a linear correction in F9X.	63
5.3	(Bottom) ZeroDegree PID after corrections. (Top) Projection in A/Q for Cr isotopes, i.e. $Z=24$	64
5.4	(Left) Energy spectrum of ^{60}Co after calibration for the 23 rd DALI2 crystal, fitted with an exponential background summed with a double gaussian function. (Right) Linearity between the ADC channel and energy for the same detector. . .	66
5.5	(Right) Raw spectrum (in ADC channels) of ^{88}Y for the 64 th DALI2 detector. The two transitions are each divided in two bumps because of the non linearity. . .	66
5.6	Energy spectra for the three calibration sources and the 186 DALI2 detectors. . .	67
5.7	(Left) Energy difference between measured and tabulated energy transitions of the calibration sources for the 182 DALI2 crystals taken in the analysis. (Right) Projection of this energy difference for all the detectors.	68
5.8	(Left) FWHM resolutions for the energy transitions of the calibration sources for the 182 DALI2 crystals taken in the analysis. (Right) Projection of this FWHM resolution for all the detectors.	69
5.9	Time drift in the TPC for one run and drift velocity and target length over the ^{66}Cr setting.	70
5.10	Differences in x (left) and y (right) reconstructed vertices from either the TPC for the two protons or one proton from the TPC and the beam from the PPAC trajectory. In orange is represented the two different distributions before corrections in position, and in red after corrections in position.	72

5.11	(Before any position correction on the DSSSD) x and y positions from the DSSSD and PPAC at F8 in the DSSSD plane along the beam on the four upper left figures. On the bottom part are the differences Δx and Δy between the DSSSD and PPAC reconstruction of the beam. On the right hand side are plotted 2D dimensional diagrams with the two different x and y beam tracking coordinates.	73
5.12	NaI(Tl) scintillator relative cross sections for photoelectric absorption (noted photo.), Rayleigh scattering, Compton scattering, and pair production (noted Pair P.) with respect to the γ ray energy.	74
5.13	Doppler corrected energy for each of the DALI2 crystals.	75
5.14	Doppler corrected energy with respect to the vertex position along the beam (Left) without MINOS reconstruction (Right) with MINOS reconstruction. . . .	75
5.15	Doppler corrected energy spectrum of ^{68}Fe with adback and gamma multiplicities after adback below 4.	76
5.16	Scheme of the LH_2 target of 102.7(10) mm when cooled down and filled with hydrogen.	77
5.17	Scheme of the analysis in momentum distribution difference in a $(p, 2p)$ reaction.	77
5.18	(Top) Direct ^{69}Co beam. Momentum difference distribution at the exit of the target between upstream (BigRIPS) and downstream (ZeroDegree). The distribution should be centered at zero and its width represents the intrinsic momentum resolution of the system. The target profile and beam trajectories are taken in consideration on an event-by-event basis. (Bottom) Momentum difference distribution inside the target by taking into account the vertex position with MINOS for the $^{69}\text{Co}(p, 2p)^{68}\text{Fe}$ case.	79
5.19	Momentum distributions for an $s_{1/2}$ and $f_{7/2}$ knocked-out proton in $^{69}\text{Co}(p, 2p)^{68}\text{Fe}$ from eikonal/DWIA calculations.	80
6.1	Doppler-corrected γ -ray spectra of ^{66}Cr populated from $^{67}\text{Mn}(p, 2p)$ in black and $^{68}\text{Fe}(p, 3p)$ reactions in blue with adback correction (maximum distance of 15 cm without energy threshold). All multiplicities are shown.	81
6.2	Doppler-corrected γ -ray spectrum of ^{66}Cr populated from the summed $^{67}\text{Mn}(p, 2p)$ and $^{68}\text{Fe}(p, 3p)$ reactions with adback correction (maximum distance of 15 cm). All multiplicities are shown.	82
6.3	Doppler-corrected γ -ray spectrum of ^{66}Cr populated from the summed $(p, 2p)$ and $(p, 3p)$ reactions: the experimental data points, the simulated response of each transition (red), and the sum of these simulated transitions with a two-exponential background (black). Multiplicities below five are shown.	83
6.4	Gamma-gamma coincidence spectra for multiplicities below five with a gate on (top) the first transition at 386(9) keV and on (bottom) the second transition at 683(9) keV.	84
6.5	Proposed level scheme of ^{66}Cr	85
6.6	Simulated 370 keV transition responses for 0, 100, 200, 500 ps half-lives.	85
6.7	Doppler-corrected experimental γ -ray spectra of ^{65}Cr populated from $^{66}\text{Mn}(p, 2p)$ reaction with adback (all multiplicities in blue and multiplicities below 5 γ in red).	86

LIST OF FIGURES

6.8	Scheme for inclusive ($p, 2p$) cross section measurement.	87
6.9	Systematics of Cr and Fe isotopes compared to the shell model calculations using the LNPS original [67] and modified interactions, and also to the Hartree-Fock-Bogoliubov + 5-dimension Collective Hamiltonian calculations using the Gogny force [68, 69].	91
6.10	Simulations of transitions in ^{68}Fe with a standard ^9Be target in black, with a 10 cm LH_2 target without and with tracking from the MINOS TPC in blue and red respectively. On the left is represented the simulation for the DALI2 array and on the right for AGATA, for a 100 pps beam during 4.5 days. For the DALI2 simulation, the SEASTAR configuration is used with the individual detector resolutions from the experiment. For AGATA, the configuration of 5 triplets and 5 doublets of AGATA clusters is used, such as used at GSI (2013).	99
C.1	Scheme of the DALI2 electronics.	106

LIST OF TABLES

2.1	Simulation results for the ^{53}K ($p, 2p$) ^{52}Ar and ^{79}Cu ($p, 2p$) ^{78}Ni physics cases. The entrance window of the target is located at the beginning of the TPC, at the Micromegas detection plane in both physics cases. Detected events correspond to the portion of ($p, 2p$) events that leave energy in the TPC. Analyzed events correspond to events that are fully treated by the tracking algorithm and lead to a vertex position.	31
4.1	Characteristics of the BigRIPS line.	49
4.2	BigRIPS and ZeroDegree settings with measured intensities.	51
5.1	ZeroDegree PPAC efficiencies convoluted with the transmission of the cocktail beam in the ZeroDegree line.	65
5.2	PPAC and DSSSD offsets applied for the first SEASTAR campaign.	72
6.1	Inclusive knockout cross sections and number of counts in the different reaction channels for the F7 DS (Downscaled by 20) trigger.	87
6.2	Exclusive knockout cross sections for the 0_1^+ , 2_1^+ , 4_1^+ , and 6_1^+ states.	89
6.3	Spectroscopic amplitudes calculated for the 0_1^+ , 2_1^+ , 4_1^+ , and 6_1^+ states, assuming no other populated transition in ^{66}Cr	89
6.4	Theoretical exclusive ($p, 2p$) knockout cross sections for the 0_1^+ , 2_1^+ , 4_1^+ , and 6_1^+ states of ^{66}Cr from the single-particle cross sections with the eikonal/DWIA formalism and the spectroscopic amplitudes from the shell model calculations with the LNPS-m interaction.	90
6.5	Energies and quadrupole deformation properties of Cr isotopes. Energies are in MeV, $B(E2)$ in $e^2 \text{ fm}^4$, and quadrupolar momenta in $e \text{ fm}^2$. Experimental energies are the same as Fig. 6.2.	93
6.6	Occupation of neutron intruder orbitals and percentage of particle-hole excitations across the $N = 40$ gap in the ground states of Cr isotopes. The last column features the pairing correlations energy differences (in MeV) evaluated between the ground state and the 2_1^+ state.	94
A.1	Conditions applied in the present study for the tracking algorithm.	103
B.1	Characteristics of the <i>Zero Degree</i> Spectrometer settings.	104
B.2	Distance between the different focal planes in BigRIPS (F0-F8) and ZDS (F9-F11).	105

